MAGNESIUM-BASED MATERIALS SUPPORTED ON CARBON FOR HYDROGEN STORAGE

MAGNESIUMVERBINDINGEN GEDRAGEN OP KOOLSTOF VOOR WATERSTOFOPSLAG.

(met een samenvatting in het Nederlands)

PROEFSCHRIFT

ter verkrijging van de graad van doctor aan de Universiteit Utrecht op gezag van de rector magnificus, prof.dr. G.J. van der Zwaan, ingevolge het besluit van het college voor promoties in het openbaar te verdedigen op woensdag 4 juni 2014 des middags te 2.30 uur

door

YUEN SHENG AU

geboren op 6 februari 1986 te Leiden

Promotores: Prof. dr. P.E. de Jongh

Promotor: Prof. dr. ir. K.P. de Jong

This thesis was mainly accomplished with financial support from a VIDI grant (016.072.316) of: “de Nederlandse Organisatie voor Wetenschappelijk Onderzoek (NWO)” and part of this work was supported by COST Action MP1103 “Nanostructured materials for solid state hydrogen storage”

He that can have patience can have what he will.

Benjamin Franklin (1706 - 1790)

ISBN: 978-94-6182-428-8

Printed by: Off Page Amsterdam

Contents

1. Introduction to energy, hydrogen and hydrogen storage in metal hydrides

1.1 Towards a new society based on renewable energy

The demand for energy in our society is essential for our current living standards and is increasing due to new emerging economies. In 2012, 80% of the energy came from fossil fuels in Europe. Hydropower and nuclear energy covered ~16% and renewable energy accounted for 4% of the total energy used [1]. The production of electricity in the same year showed a similar trend [2]. The division of the energy sources for generation of electricity is shown in Fig. 1 - 1. The high dependence on fossil fuels (63%) as the main energy source has led to a rapid depletion of natural resources [3]. Another issue related to burning of fossil fuels is carbon dioxide production and the related enhanced greenhouse effect [4].

To become less dependent on fossil fuels, different scenarios can be envisioned. Favorable would be a worldwide reduction in energy consumption. However, it is unlikely that his will happen given the current trends and upcoming economies. Another option is to find a complete replacement for fossil fuels. Fortunately, many alternatives are available, but they have to fulfill certain requirements from a practical, financial and environmental point of view.

Fig. 1 - 1 shows that nuclear energy is the second largest energy source covering 18% of the total electricity production, but this technology has disadvantages, mainly related to the disposal of nuclear waste and the threat of nuclear meltdowns. Hydropower plants closely follow nuclear power, covering 14% of the total electricity production. Hydropower is safer and has less impact on the environment than nuclear power. Unfortunately, the plants require certain landscapes, which are not worldwide available and the electricity produced by the facility is not sufficient. Nowadays, only 3 hydropower plants in the world are capable of producing more than 10 GW (50 TWh per year), which is just a fraction of the total power used (102254 TWh) [5].

Only 5% of the energy usage is covered by renewable energy sources such as solar and wind energy. Using renewable energy sources to substitute fossil fuels is the most promising solution from an environmental perspective. It can be applied almost anywhere in the world and the risks

for calamities affecting huge areas and large amount of people are limited. The only barrier is caused by the low efficiency, which leads to high costs for implementation. On the other hand, rapid development in this area and upscaling of renewable energy can lead to a reduction in the costs over time making renewable energy also financially feasible [6]. For example, the mass-production of solar cells has decreased the overall costs for solar energy by half over 5 years [7].

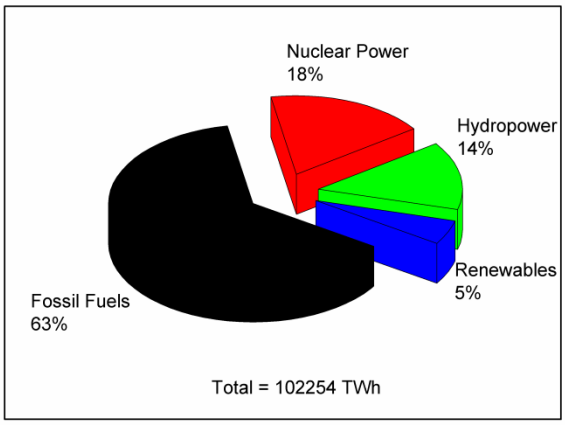

Fig. 1 - 1: Worldly power production by fuel type in 2012 [2].

Although renewable energy sources are promising to replace the use of fossil fuels, there are still some issues to be addressed. The production of solar energy cannot take place during nighttime and windmills do not operate, when wind is absent. Also, these renewable sources mainly produce electricity and this cannot be used for off-grid applications without proper methods for energy storage. If electrical energy can be converted into a fuel, the energy will be available anywhere, anytime. An alternative feedstock is biomass, which is being researched extensively. Hydrogen can be produced for instance by splitting water using electricity (electrolysis) or from biomass, and further converted into other fuels such as methanol or dimethyl ether, or used as fuel directly [8, 9].

1.2 Hydrogen as sustainable energy carrier

Hydrogen has the advantage that it is non-toxic and its weight-based energy content (142 $MJ \cdot kg^{-1}$) is higher than that of petrol (47 $MJ \cdot kg^{-1}$). This advantage is used in for example space technology. As proposed in the so-called 'hydrogen economy', hydrogen is generated from water [10]. Electrolysis of H_2O yields H_2 and O_2 and the required electricity is provided by a renewable energy source. Burning H_2 directly or using a fuel-cell to regain electricity would create a zero-

emission cycle (Fig. 1 - 2) [11, 12]. Despite the mentioned advantages, hydrogen also has several drawbacks preventing it from fast implementation in society. Currently, large amounts of H_2 cannot be produced in a cost effective way from water without involving fossil fuels. Another issue is the lack of feasible methods to store hydrogen in a safe and compact way.

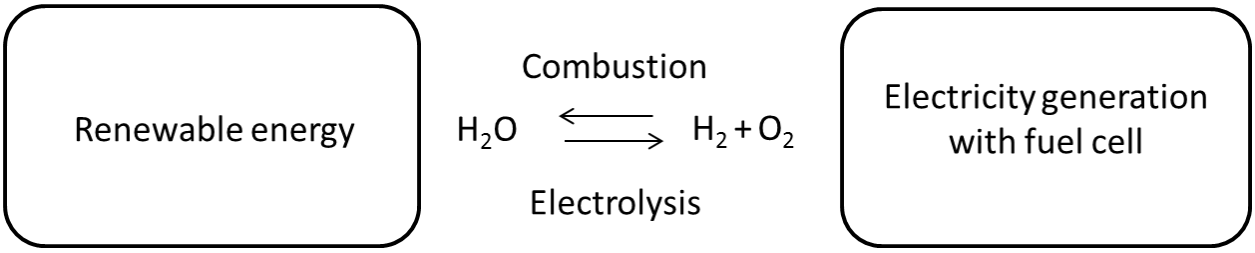

Fig. 1 - 2: A simplified zero-emission cycle as proposed in the hydrogen economy model.

The simplest way to store hydrogen is at ambient conditions, as a gas. However, hydrogen gas has a very low density (0.092 $kg \cdot m^{-3}$), which means that a lot of space is required. This might be less of an issue for stationary applications, but it is an issue whenever transportation of the fuel is required or when the usage of hydrogen is desired in mobile applications and/or small portable devices [12-15]. Compression in high-pressure cylinders is currently possible up to 700 bars of hydrogen [16]. But this method is not safe in case car accidents occur, where possibly all hydrogen is released uncontrolled and may even exceed the explosion limit. Another idea is to store hydrogen as a liquid at very low temperatures (~ -253 ^{o}C). Similar safety issues remain in case the permanent cryogenic cooling fails and this method is less cost and energy efficient compared to storage as gas.

A promising way to store hydrogen is to use solid absorbents [15]. Hydrogen may be bound to a host material as atoms or ions and a (metal) hydride compound is formed. Fig. 1 - 3 shows several examples of these hydride compounds. It also gives an overview of the theoretical storage capacities of the different materials and methods. The hydrogen storage material should possess both a high gravimetric and volumetric density to store hydrogen is the most compact way. The marked areas show the typical capacity ranges for certain classes of hydride compounds and other storage methods. Moreover, the figure shows that mainly the volumetric density in solid-materials is much higher compared to hydrogen storage in gaseous or liquid form and solves the issues associated with space restrictions. The formed hydride compounds are also very stable and do not release hydrogen, when it is exposed to the atmosphere and this meet the safety requirements.

Unfortunately, the high stability of the hydrides compounds is also a drawback. Hydrogen is bound so strongly to the host material that it is difficult to release it from the host. To break the chemical bond between hydrogen and the host material, sufficient energy has to be provided by heating the material to high temperatures. This decreases the energy efficiency of the storage method. The challenge in the field of hydrogen storage in the solid state is to find new materials and/or improve materials, so that hydrogen storage and release occurs reversibly at near-ambient conditions. To achieve this, we have to understand more about the nature of the bond between the host material and hydrogen; and which barriers have to be overcome to store and release hydrogen from the host material.

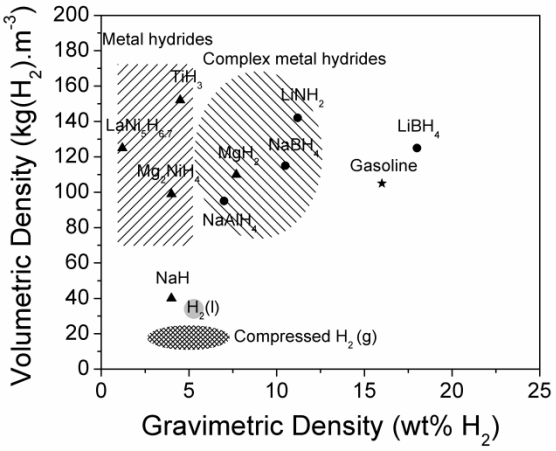

Fig. 1 - 3: Overview of the storage capacity of different H_2 storage methods. Compressed H_2 is stored in a pressure range of 150 – 700 bar. Reproduced from Chandra D. et al. [14].

1.3 Hydrogen storage in solid materials

Hydrogen can be bound to solid materials in several ways. The first is physical bonding of H_2 molecules, often referred to as physisorption, where hydrogen is bound to the surface of a host material. The interaction between H_2 molecules and host material is based on van der Waals forces with a typical binding energy of 1-5 $kJ \cdot mol^{-1}$ [17]. Examples of materials, where hydrogen is stored involving this type of binding, are carbon and metal-organic frameworks displaying high specific surface areas [18, 19].

The second type of bonding is chemical in nature. In this case the hydrogen molecule is split into atoms or ions, which form chemical bonds with the host material. The chemical bond between the H-atoms and the host can be further classified as metallic, ionic or covalent [20]. In metal hydrides, a metallic or ionic bond exists between a metal-(ion) and hydrogen. PdH and

LiH are examples, where the H-atoms have a metallic and ionic bond respectively. Another category is the complex metal hydrides, in which both ionic and covalent bonds are present. The H-atoms are bound covalently to species such as Al, B or N forming complex anions, which form an ionic lattice with metal cations. Examples are $Li[BH_4]$ or $Li[NH_2]$, where the complex anion is shown in the brackets. The enthalpy required to decompose the (complex) metal hydrides is usually well above 50 $kJ \cdot mol^{-1}$ H_2.

For practical application of hydrogen storage materials for instance in cars and mobile devices, the desired operation conditions are typically between 1 - 10 bar at around ~100 ^oC. Hydrogenation/dehydrogenation equilibrium under these conditions is achieved if the dehydrogenation enthalpy is ~40 $kJ \cdot mol^{-1}$ H_2 [15, 21]. The high temperatures required to break the chemical bond is one of the main reasons, why an important focus of the research on metal hydrides is to find materials with modest decomposition enthalpies or apply modifications to the material to destabilize the metal hydride compound.

On the other hand, the bond strength in material, where H_2 molecules are physisorbed, is too weak and leads to hydrogen adsorption to occur below -196 ^oC. However, to obtain sufficient storage capacity (> 1 wt %), either multi-layer adsorption of hydrogen molecules is required or the specific surface area of the host material should be greatly enhanced. Note that for example a carbon nanofiber of 2000 $m^2 \cdot g^{-1}$ is only able to adsorb 0.2 wt% hydrogen [17]. With multi-layer adsorption, the average van der Waals forces between the host and the physisorbed H_2 molecules is very small; and operation temperatures below the critical temperature of H_2 (-240 ^oC) are required. Therefore, research on this type of materials is focused on maximizing the surface area of the host material and strengthening the bond between the host and adsorbed hydrogen molecules.

1.4 Hydrogen storage in magnesium

Magnesium is a good candidate for hydrogen storage. It can form MgH_2, which is a metal hydride that has a high gravimetric capacity of 7.6 wt% H_2 and a volumetric density of ~110 $kg \cdot m^{-3}$ H_2. Another benefit is the low costs of the material since Mg is in the top 10 of most abundant elements in the earth's crust. However, a drawback is the high stability of MgH_2 due the existence of the ionic Mg-H bond that requires an enthalpy of 75 $kJ \cdot mol^{-1}(H_2)$ to decompose MgH_2 for hydrogen release. Another issue is the slow kinetic rate for the hydrogen sorption

reactions. Much research is conducted for Mg in order to lower the decomposition temperature and improve the hydrogen absorption and release rates [11, 13, 22]. The next section will discuss the fundamental aspects of thermodynamics and kinetics of the equilibrium reaction $Mg + H_2 \leftrightarrow MgH_2$ in order to understand the applied methods to improve Mg-based hydrogen storage systems.

1.4.1 The thermodynamic equilibrium of the hydrogen sorption reaction in $Mg(H_2)$

Whether hydrogen is absorbed or desorbed from Mg or MgH_2 respectively, depends on the applied temperature and pressure conditions. These conditions are determined by the thermodynamic equilibrium of the (de)hydriding reaction. One of the reactions is favorable if the Gibbs free energy (ΔG) is < 0 (eq. 1 - 1) [23].

$$\Delta G(p,T) = \Delta H - T\Delta S \text{ (Eq. 1 - 1)}$$

The enthalpy (ΔH) required for formation or decomposition of a hydride is characteristic for each material. To let the decomposition reaction $MgH_2 \rightarrow Mg + H_2$ occur, an enthalpy of 75 $kJ \cdot mol^{-1}$ H_2 at standard conditions (25 ^oC and a pressure of 1 bar) is required. The term $T\Delta S$ includes the temperature (in K) and change in entropy respectively. The value for the entropy is mainly determined by the entropy change from hydrogen in the gas state to hydrogen bound to the host material. In case of MgH_2, the difference is between H atoms bound in the lattice of MgH_2 and H_2 gas molecules in the surrounding atmosphere. The value for the entropy is estimated to be ~130 $J \cdot mol^{-1} \cdot K^{-1}$ (at -273 ^oC) [24, 25]. Assuming a ΔH of 75 $kJ \cdot mol^{-1}$ H_2 and a ΔS of 130 $J \cdot mol^{-1} \cdot K^{-1}$ for desorption of MgH_2, at low temperatures and 1 bar H_2 ΔH is the larger than the term $T\Delta S$ and results in a positive value for ΔG, hence dehydrogenation will not occur. For example at a temperature of 200 ^oC (473 K) and a H_2 pressure of 1 bar, ΔG = 13.51 $kJ \cdot mol^{-1}$, which is a positive energy and decomposition is not favorable. By increasing the temperature sufficiently, the term $T\Delta S$ will exceed ΔH, which result in a negative value for ΔG and hydrogen release is favorable. Assuming a temperature of 400 ^oC (673 K) and a H_2 pressure of 1 bar, ΔG = -12.49 $kJ \cdot mol^{-1}$, hence decomposition becomes favorable. Note that a change in pressure will follow a similar effect as a change in temperature. Whenever the values of ΔH and $T\Delta S$ are equal to each other, then $\Delta G = 0$, which means that the reaction is in equilibrium. This occurs at approximately 300 ^oC (573 K) at 1 bar of H_2 pressure.

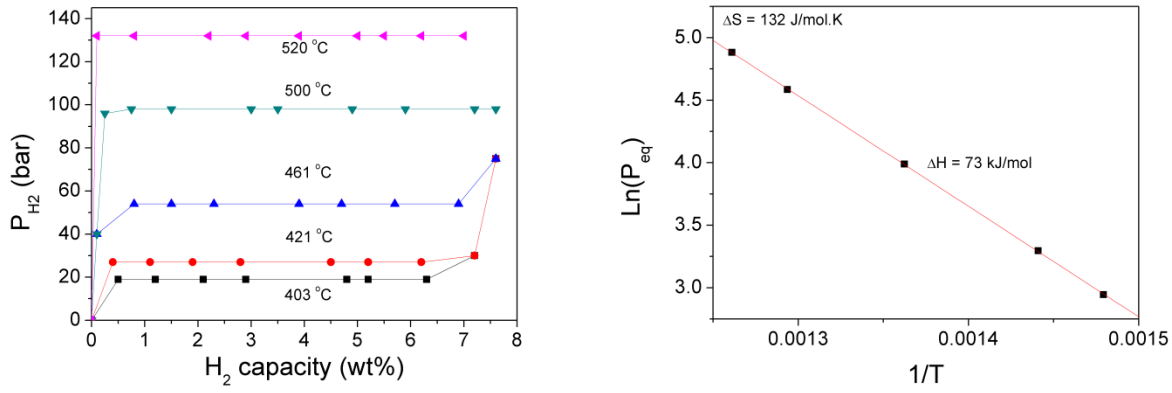

Fig. 1 - 4: Left: Pressure composition isotherms of the Mg + H_2 ↔ MgH_2 equilibrium reaction. Right: van 't Hoff plot derived from the equilibrium pressures. Reproduced from Bogdanovic et al [26].

The entropy and enthalpy value for the equilibrium reaction Mg + H_2 ↔ MgH_2 can experimentally be determined by measuring Pressure-Composition-Isotherms (PCIs). Fig. 1 - 4 shows the PCIs of the Mg(H_2) system by varying the H_2 pressure (P_{H2}) at constant temperature (T) and measuring the change in H_2 capacity (wt% hydrogen). The amount of H_2 being absorbed or released is determined by the change in H_2 pressure. At the beginning when P_{H2} = 0 at 0 wt% capacity, metallic Mg is present. Whenever H_2 pressure is applied and increased at a constant temperature, absorption of hydrogen by Mg starts to occur for example at 461 °C and 40 bar H_2 pressure (Fig. 1 - 4: left). After increasing the pressure to 58 bar, an equilibrium pressure (P_{eq}) is found as displayed by the plateau and the reaction Mg + H_2 ↔ MgH_2 is in equilibrium (ΔG = 0). In this state both Mg and MgH_2 are present. Further increase of the pressure leads to the complete conversion to MgH_2 from Mg over time as is indicated by the steep increase of the pressure near the full capacity of 7.6 wt% H_2. The equilibrium pressures (P_{eq}) and temperatures (T) can be used in a van 't Hoff plot to determine the entropy and enthalpy of the material following Eq. 1 - 2:

$$\ln(P_{eq}) = \Delta H/RT - \Delta S/R \quad \text{(Eq. 1 - 2)}$$

The enthalpy (ΔH) can be derived from the slope ($\Delta H/RT$) of the linear relation and the entropy (ΔS) from the intercept ($\Delta S/R$) and resulted in an enthalpy change of 73 kJ·mol^{-1} and an entropy change of 132 J·mol^{-1}·K^{-1} (Fig. 1 - 4: right).

For each reaction a standard enthalpy is defined by the formation enthalpies of the reactants and products. Density function theory calculations (DFT) confirm that the formation enthalpy is influenced by the particle size and becomes significant for particle sizes below 1 nm [27-29]. However, a possible change in entropy has not been taken into account in the calculations. No gain in free energy is obtained, if the change in entropy between H_2 gas molecules and H-atoms in the MgH nanoparticles is decreased. If a MgH_2 nanoparticle decreased the desorption enthalpy from 75 kJ·mol^{-1} H_2 to 69 kJ·mol^{-1} H_2, it will not have any effect on the thermodynamic equilibrium if the entropy change is compensated by an entropy change smaller than 120 J·mol^{-1}·K^{-1} (at 300 ^{o}C and 1 bar H_2).

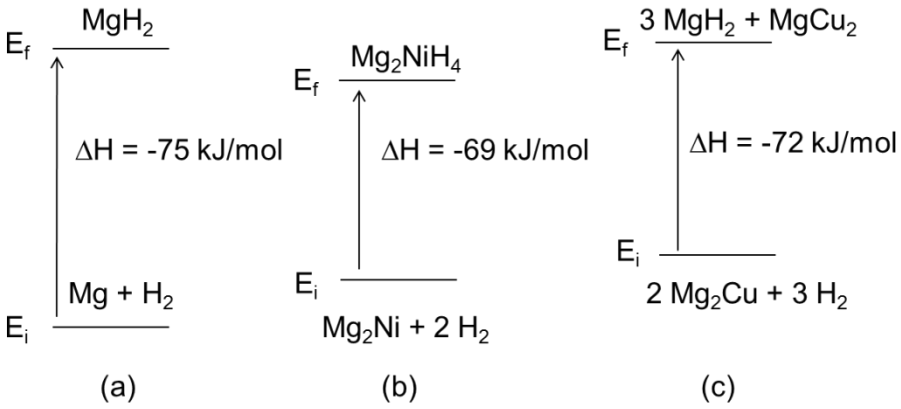

Fig. 1 - 5: Schematic representation of the energy states (*E*) and enthalpy change (Δ*H*) for different reactants (E_i) and final products (E_f). (a) The enthalpy of formation for MgH_2. (b) The enthalpy of formation for the ternary hydride Mg_2NiH_4 that forms an alloy upon decomposition. (c) The enthalpy of formation for a disproportionation reaction with Mg_2Cu as alloy.

A significant change in equilibrium conditions for hydrogen sorption is obtained by changing the reactants and related products as illustrated in Fig. 1 - 5. Situation (a) represents the reaction to form MgH_2 from Mg, which has an enthalpy change of -75 kJ·mol^{-1}(H_2). In example (b) the reaction is changed by forming a different hydride compound and used a different reactant with both a different energy state. The Mg_2Ni alloy is used as reactant and Mg_2NiH_4 is formed, which has a different thermodynamic equilibrium. The formation of different Mg-based hydrides such as, Mg_2NiH_4, Mg_2CoH_5, Mg_2FeH_6 also known as ternary hydrides were reported [30-32]. These ternary hydrides have lower decomposition enthalpies in the range of 60-70 kJ·mol^{-1}(H_2) instead of 75 kJ·mol^{-1}(H_2) for MgH_2. More recent reports show the existence of other Mg-based ternary hydrides with Ti, Zr, Hf, V, Nb and Ta [33]. Mg can also form complex metal hydrides such as $Mg(AlH_4)_2$ and $Mg(BH_4)_2$ [34, 35].

Another method is to add an element that is able to react or alloy with Mg, which results in a dehydrogenated phase with a negative formation enthalpy. This results in a smaller heat of reaction for the combination of the endothermic decomposition of MgH_2 and the exothermic reaction of Mg with the added element. The reaction that follows is classified as a disproportionation reaction and a stable magnesium alloy is formed during decomposition. The example in (c) shows the disproportionation reaction $2\ Mg_2Cu + 3\ H_2 \leftrightarrow MgCu_2 + 3\ MgH_2$, where the enthalpy is lowered by 3 $kJ \cdot mol^{-1}(H_2)$ due to formation of a Mg-Cu alloy. Other Mg alloys that are able to perform this type of reaction are Mg-Al and Mg-Si [36-38]. Similar to this method is the use of mixed metal hydride systems to destabilize MgH_2, for example a mixture of $MgH_2 + LiBH_4$. The two different hydrides will be able to react with each other during decomposition and form different dehydrogenated compounds, which usually results in a smaller ΔH compared to the decomposition of the metal hydrides separately [39-49].

A main issue with these methods is the reversibility of the reaction, because either the hydride or the compounds formed after decomposition might be too stable. A physical relation that relates the stabilities of the ternary hydride compared to the alloy and the binary hydride is:

$$\Delta H_f(ABH_{2x}) = \Delta H_f(AH_x) + \Delta H_f(B_nH_x) - \Delta H_f(AB_n) \quad \text{(Eq. 1 - 3)}$$

This equation is known as Miedema's rule of reversed stability [50]. The heat of formation of the (ternary) hydride phase is the sum of the heat formation (ΔH_f) of the metal hydrides (AH and BH) and the alloy (AB). In case of the formation of the ternary hydride Mg_2NiH_4 ($\Delta H_f(ABH_{2x})$), Mg is the element forming the stable MgH_2 phase ($\Delta H_f(AH_x)$), while another element such as Ni ($\Delta H_f(B_nH_x)$) does not form a stable hydride. The value for the term $\Delta H_f(AH_x)$ is negative, which is -75 $kJ \cdot mol^{-1}(H_2)$ for MgH_2. The term $\Delta H_f(B_nH_x)$ is 0 if no hydride is formed. If the heat of formation for the alloy or another decomposition product ($\Delta H_f(AB_n)$) is very negative for example MgB_2 (ΔH_f = -156 kJ mol^{-1}) [51], it will result in a less negative value for $\Delta H_f(ABH_{2x})$ and the ternary hydride phase is more unstable. It is known that $Mg(BH_4)_2$ is difficult to synthesize from MgB_2 and required very high pressures and temperatures [52]. Vice versa if the alloy phase is less stable (less negative value $\Delta H_f(AB_n)$), for example in Mg_2Ni (ΔH_f = -67 kJ mol^{-1}) [53], the ternary hydride becomes more stable (negative value of $\Delta H_f(ABH_{2x})$ is higher). In conclusion, the ternary hydride phase is more stable, if a less stable alloy is formed after decomposition of the hydride.

The thermodynamic equilibrium is determining the temperature and pressure conditions at which hydrogen sorption may occur, but another important aspect is the rate of the hydrogen sorption reactions. The kinetics of the reactions are determined by several aspects. It is illustrative to look at the necessary steps required for hydrogen to be stored or released from a metal hydride system in order to understand the rate limiting factors.

1.4.2 The hydrogen sorption kinetics of the Mg(H_2) system

A general description on the mechanism for hydrogen sorption is given in Fig. 1 - 6. State (a) describes free H_2 molecules in the atmosphere separated from an Mg particle. When the H_2 molecules and the Mg particles are brought together in a closed system at ambient conditions and pressures, there will be an initial albeit low surface coverage by H_2 molecules as illustrated in situation (b). Whenever the H_2-pressure is increased above the equilibrium pressure and the right temperature is applied, e.g. 300 ^oC and 50 bar H_2, the reaction equilibrium is favorable for MgH_2 formation. Sufficient energy is required to break the H-H bond to split the hydrogen molecules into single H-atom. The H-atoms will start to penetrate the surface and diffuse through the metal lattice, forming a chemical bond with the metal. Via nucleation and growth, the MgH_2 phase will be formed as shown in Fig. 1 - 6 (c). If the H_2-pressure is removed and sufficient heat is applied, the reverse process will occur, leading to decomposition of MgH_2 and hydrogen will be released [54].

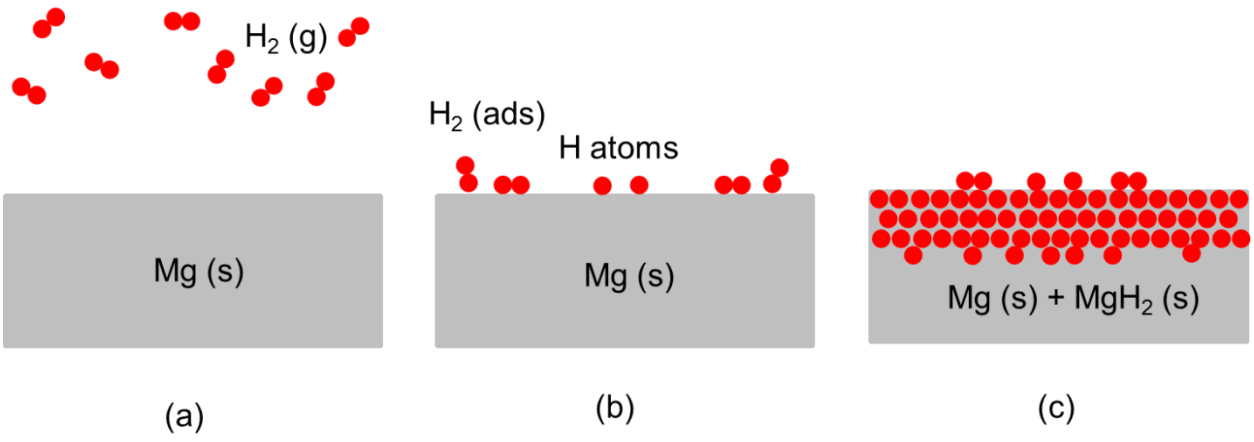

Fig. 1 - 6: Schematic mechanism on the hydrogen sorption process. (a) Free H_2 gas molecules and Mg. (b) H_2 molecules adsorbed on the surface of the metal and split into H-atoms. (c) Penetration and diffusion of the H-atoms through the metal lattice into magnesium accompanied by nucleation and growth of the MgH_2 phase.

Each step could potentially be rate-limiting for the overall hydrogen sorption reaction. The possible kinetic barriers for the absorption reaction will be discussed. The adsorption step on the

surface could be rate limiting in catalytic reactions, if there is no electronic interaction between the molecule and the surface. However, under high pressure conditions, which is required for hydrogen absorption to occur, sufficient hydrogen molecules should be able to interact with the surface of the host material. As a consequence, the approach of H_2 molecules and H_2 adsorption are usually not rate limiting for the hydrogen absorption reaction.

The next step is the splitting of the hydrogen molecule into single hydrogen atoms. Breaking the H-H bond requires an energy of 436 $kJ \cdot mol^{-1}$ (at 25 ^oC) [55]. Mg is not very effective to catalyze this process. Therefore, the dissociation of the hydrogen molecule can pose a significant barrier limiting the rate of the reaction. Addition of other elements acting as a catalyst for hydrogen dissociation can lower the kinetic barrier [56]. For example Ni and Pd catalyze the dissociation of the H-H bond and they have been used as catalyst to improve the sorption kinetics in Mg [57, 58].

Penetration of the H-atoms and diffusion through the metal lattice, followed by nucleation and growth of the metal hydride phase may also be a rate limiting step, which plays a role during both absorption and desorption [59].The rate for atomic H diffusion through the Mg lattice depends mainly on the path length and if the H-atoms are able to penetrate the surface of the lattice. These processes are necessary to allow nucleation and growth of the metal hydride phase [60]. Note that absorption of H-atoms by Mg also changes the density of the material from 1.74 $g \cdot cm^{-3}$ to 1.45 $g \cdot cm^{-3}$ when MgH_2 is formed, so mechanical strain forces also have to be overcome during nucleation and growth of the MgH_2 phase. A similar analysis can be made for the desorption steps. However, the main issue for desorption is the high energy required to break the bond between magnesium and hydrogen.

The diffusion time can be reduced by decreasing the particle size, which coincides with increasing the specific surface area of Mg. Nanoparticles have a larger amount of surface atoms, so that H_2 molecules have better access to the metal lattice of Mg leading to an increase in the rate and chance for nucleation to form MgH_2. Also the growth distance to convert the whole Mg particle to MgH_2 is reduced [61]. Much research is conducted to find ways to make nanoparticles or nanostructured Mg compounds [62, 63].

A study on Mg thin films with a thickness of 10 nm showed that the nucleation and growth process is a rate limiting factor during hydrogen absorption. Nucleation of the MgH_2 phase occurred at preferential sites followed by growth of the MgH_2 phase [64]. The hydrogenation rate

decreased over time, because the amount of available nucleation sites was limited. After saturation of the nucleation sites, the phase transformation to MgH_2 continued via growth. A following study revealed that nucleation occurred instantly at high pressure conditions and only growth of the nuclei is the rate limiting step for complete formation of MgH_2 from the Mg thin film [65]. Dehydrogenation took place via a 1-dimensional growth mechanism of the Mg-phase and resulted in a porous Mg phase, which was favorable for rehydrogenation due to the improved access for H_2. The investigation on $Mg(H_2)$ thin films showed that the mechanisms for hydrogen absorption and desorption were not the same. No clear nucleation sites for Mg were observed during dehydrogenation.

Another common method to obtain Mg nanostructures is by mechanical milling of bulk precursors. Huot et al. has performed ball-milling of MgH_2 and compared the new nanostructured material with bulk MgH_2 [66]. The nanostructured MgH_2 showed faster kinetics for both absorption and desorption, mainly due to an increase of the metal surface area and the creation of defects in the Mg lattice, which improves the accessibility for the H atoms and increases the amount of nucleation sites. Also indications for the weakening of the Mg-H bond were found, when MgH_2 is nanosized. Further improvement was made by ball-milling mixtures of $Mg(H_2)$ doped with other elements as catalyst [67-74]. The doping of elements is not limited to a single metal, but also mixtures with other elements or metal oxides were also very effective. So far, the addition of Nb_2O_5 has shown the best improvements for the hydrogen sorption kinetics [67, 69, 75-77].

Nanosizing is a very interesting tool since multiple aspects of the hydrogen storage material are improved without changing the reaction or storage capacity. However, nanoparticles possess a high surface energy and tend to grow with neighboring particles to form large particles, which are more stable due to their lower surface energy. The driving rate of particle growth often becomes higher at elevated temperatures [78]. After severe particle growth, the properties of the material will revert to that of bulk material and the benefits will be lost.

Particle growth can be prevented by separating the particles physically. One way to achieve this is by dispersing the nanoparticles on a support material, which is already applied in large chemical processes requiring the presence of a catalyst. The support is able to separate the particles and may provide anchoring points or physical confinement to restrict the mobility of the nanoparticles at elevated temperatures [79, 80]. Physical confinement is in particular interesting,

because it is also able to enhance the reversibility of certain complex metal hydride systems by stabilization of the hydride phase [81-84].

1.5 Supported MgH_2 nanoparticles for hydrogen storage

A support is mainly used to prevent sintering of the nanoparticles. Moreover, the transformation from a metal species to a metal hydride species changes the heat conductivity properties of the material. Typically, metallic Mg is a conductor, while MgH_2 is an insulator. On the other hand if bulk Mg is used in large systems, the heat capacity is too large and leads to the formation of hot and cold spots during desorption and decreases the efficiency of the material. During absorption, the heat produces (75 $kJ \cdot mol^{-1}$) has to be removed in order to keep the reaction running [85]. The addition of support could be somewhat helpful to overcome this issue.

The options for the support material from a synthesis aspect are limited. The final product and intermediates should not react with the support material to form stable compounds that prevents hydrogen sorption. The support material should provide sufficient surface area to disperse the nanoparticles on. For this reason, most of the literature report about metal hydrides supported on carbon material with different morphologies varying from graphic material to carbon nanotubes [86-91] , nanofibres [92], templated carbon structures [93, 94], activated carbons [95-102] and carbon aerogels [103-105]. Yet, the use of mesoporous silica was also reported [106-108].

The research described in this thesis used activated carbons and carbon aerogels as support material. The preparation of activated carbons typically involves 3 steps: raw material preparation, low temperature carbonization and activation. The raw materials are matter containing carbon such as wood, coal or biomass derived material. The final product is an amorphous carbon material that is build up from disordered graphite sheets. Activated carbon materials have a high specific surface area (800 - 1200 $m^2 \cdot g^{-1}$) and can possess micro- and/or mesopores with pore volumes in the range of 0.9 - 1.5 $cm^3 \cdot g^{-1}$ [109]. These properties are useful for application as membranes, catalyst support and gas storage [110-112]. Additionally, the surface properties of the carbon support can be modified by different treatments. Functional groups are added to be used as anchoring points for metal deposition. For example, oxygen groups can be added via acid treatments or doping of other elements [113, 114].

Carbon aerogels are prepared by pyrolyzing a polymer obtained from a polymerization reaction between different precursors. For example, carbon aerogel can be obtained via

polycondensation of formaldehyde and resorcinol in aqueous solution [115]. The advantage of using carbon aerogels is their tunable pore structure by varying the precursors and/or concentrations. The pore size distribution is more dominant in the mesoporous region compared to activated carbon, which mainly contains micropores. Surface areas up to 1100 $m^2 \cdot g^{-1}$ can be obtained [116]. The application of carbon aerogels is not limited to support materials, but is also used as electrodes and super capacitors [117, 118]

1.5.1 Methods for deposition of Mg nanoparticles on carbon supports

Different methods are reported to prepare supported Mg-nanoparticles. Ball-milling was already mentioned earlier. However, most literature report about ball-milling with carbon as an additive to improve the milling process rather than as a support [119-123]. A possible method to disperse Mg on a support is by using solution impregnation. Usually, a metal organic Mg-complex, such as diethyl magnesium or dibutyl magnesium, is used as precursor in an organic solvent [94, 104]. The presence of oxygen must be avoided to prevent the irreversible formation of magnesium oxide. After removal of the solvent, supported MgH_2 nanoparticles are obtained via reaction with H_2 under high pressure.

Addition of compounds incapable of storing hydrogen decreases the total capacity of the material; hence the Mg-loading should be as high as possible. The discussed synthesis methods face some challenges in this aspect. The solution impregnation route is limited by the maximum concentration of the metal-complex in a solvent. Multiple impregnations have to be performed to reach higher loadings, which potentially causes redistribution of the previously deposited particles resulting in particle growth.

Another method is melt infiltration [124]. The literature reports about the application of melt infiltration to deposit complex metal hydrides such as $LiBH_4$, $NaBH_4$ and $NaAlH_4$ [125-127]. Deposition of the complex metal hydrides was successful by applying increased H_2 pressure to prevent decomposition before the melting point is reached, which is one of the conditions to apply melt infiltration successfully. Melt infiltration has a better potential to be applied at large scale, but the success rate also depends on the wetting properties. MgH_2 does not melt before decomposition, however, Mg metal melts at 650 ^oC and can form MgH_2 after hydrogenation. MgH_2 nanoparticles were synthesized by heating a mixture of Mg with an activated carbon support above the melting point [128], but Mg and carbon do not lead to favorable wetting

condition due a contact angle larger than 90^{o} between the Mg and carbon interface as is described in the literature [129, 130]. Therefore, a fraction of Mg particles remained on the exterior surface of the carbon support. A possible solution to increase the amount of Mg nanoparticles is to add other metals acting as wetting layer for Mg to improve the deposition on the carbon support [99, 114].

In conclusion, a support can be used to improve the stability of the nanoparticles and is beneficial for the heat conductivity for practical applications. However, from a synthesis aspect some challenges have to be faced in order to obtain supported nanostructured Mg-based materials.

1.6 Scope of the thesis

Different Mg-based hydrides are studied supported on different type of carbon supports, varying from non-porous graphite to porous carbon materials with different pore sizes and structures in order to obtain nanostructured Mg-based hydrides with favorable hydrogen sorption properties. A combination of the different methods as described in the introduction is used to improve the kinetics and to change the thermodynamics. However, the main purpose is to investigate the effect of nanosizing and the role of the support material on the synthesis and the hydrogen sorption properties of the different nanostructured Mg-based hydride compounds.

Chapter 2 focuses on the MgH_2 system, where only carbon is used as a support and potentially as scaffold material to form MgH_2 nanoparticles. The method to deposit Mg nanoparticles is via a heat treatment of an Mg/carbon composite above the melting point of Mg. Not only the change in the hydrogen sorption properties due to addition of a support and the presence of nanoparticles are studied, but also the effect of different pore sizes of the scaffold is investigated to find out if the particle size can be controlled during synthesis.

In Chapter 3, the Mg-Cu-H system is discussed. Since no ternary hydride of Mg-Cu-H is reported, the aim is to find out if any changes could be made in the thermodynamics by addition of Cu and if different compounds, such as a ternary compound or alloys, could be formed. The synthesis was performed in multiple steps, starting with deposition of small Cu particles on different carbon supports via incipient wetness impregnation followed by reaction with molten Mg and hydrogenation. Both the changes in kinetic and thermodynamic are investigated due to nanosizing and addition of Cu and C to the Mg(H_2) system.

Chapter 4 deals with a new method to synthesize magnesium boron hydrides, which is a promising complex hydride system. Among these $Mg(BH_4)_2$ has a high gravimetric storage capacity of 14.9 wt%. Even more interesting is the calculated decomposition enthalpy of 39 $kJ \cdot mol^{-1}$. Unfortunately, the decomposition of $Mg(BH_4)_2$ is hindered by kinetic barriers and the system cannot be rehydrogenated under mild conditions. This chapter investigates the possibility to synthesize and to improve the decomposition and reversibility of the $Mg(BH_4)_2$ system by nanosizing combined with supporting the material on carbon. The material is synthesized by using supported nano-Mg particles on carbon aerogel or non-porous graphite as precursor followed by ball-milling in B_2H_6/H_2 pressure.

Chapter 5 continuous on taking advantage of the increased reactivity of nanoconfined species. Nanoconfined MgH_2 and Mg-Ni-H compounds were used initially for direct reaction with B_2H_6 via heat treatment to form nanoconfined magnesium borohydride. The challenge is to characterize the newly formed Mg-B-H species and to investigate the role of Ni as additive, which potentially facilitate the formation of the $Mg(BH_4)_2$ phases and catalyzes the hydrogen sorption reactions.

In summary, MgH_2 is a promising compound to be applied as hydrogen storage material. However, before application can be realized, the kinetic properties have to be improved and/or the operation temperature and pressures have to be lowered to the desired range of 1 - 10 bar at around ~100 ^oC. The thesis describes carbon supported nanostructured Mg-based compounds as a potential method to improve the kinetics and change the thermodynamic equilibrium of MgH_2. New methods are shown to synthesize nanostructured compounds and the structure is related to the hydrogen sorption properties.

References

(1) BP, Statistical Review of World Energy June 2013. *http://www.bp.com/content/dam/bp/pdf/statistical-review/statistical_review_of_world_energy_2013.pdf* (accessed 01/04, 2014).

(2) International Energy Agency, Monthly Electricity Statistics. *http://www.iea.org/newsroomandevents/newsletters/* (accessed 03/28, 2013).

(3) U.S. Energy Information Administration, U.S. Crude Oil, Natural Gas, and NG Liquids Proved Reserves. *http://www.eia.gov/naturalgas/crudeoilreserves/* (accessed 06/24, 2013).

(4) U.S. Enviromental Protection Agency, Climate Change. *http://www.epa.gov/climatechange/* (accessed 06/24, 2013).

(5) Itaipu Biacional, The world's largest of renewable clean energy. *http://www.itaipu.gov.br/en/energy/energy* (accessed 06/24, 2013).

(6) Mueller-Langer, F.; Tzimas, E.; Kaltschmitt, M.; Peteves, S. Techno-Economic Assessment of Hydrogen Production Processes for the Hydrogen Economy for the Short and Medium Term. *Int J Hydrogen Energy* **2007**, *32*, 3797-3810.

(7) SolStats, Solar panel prices – drop by half over the last 5 years. *http://www.solstats.com/blog/solar-energy/solar-panel-prices-drop-by-half-over-the-last-5-years/* (accessed 01/04, 2014).

(8) Huber, G. W.; Iborra, S.; Corma, A. Synthesis of Transportation Fuels from Biomass: Chemistry, Catalysts, and Engineering. *Chem. Rev.* **2006**, *106*, 4044-4098.

(9) Olah, G. A. Perspective: After Oil and Gas: Methanol Economy. *Catalysis Letters* **2004**, *93*, 1-2.

(10) Crabtree, G. W.; Dresselhaus, M. S.; Buchanan, M. V. The Hydrogen Economy. *Phys Today* **2004**, *57*, 39-44.

(11) Sakintuna, B.; Lamari-Darkrim, F.; Hirscher, M. Metal Hydride Materials for Solid Hydrogen Storage: A Review. *Int J Hydrogen Energy* **2007**, *32*, 1121-1140.

(12) Gahleitner, G. Hydrogen from Renewable Electricity: An International Review of Power-to-Gas Pilot Plants for Stationary Applications. *Int J Hydrogen Energy* **2013**, *38*, 2039-2061.

(13) Felderhoff, M.; Bogdanovic, B. High Temperature Metal Hydrides as Heat Storage Materials for Solar and Related Applications. *International Journal of Molecular Sciences* **2009**, *10*, 335-344.

(14) Chandra, D.; Reilly, J. J.; Chellappa, R. Metal Hydrides for Vehicular Applications: The State of the Art. *JOM* **2006**, *58*, 26-32.

(15) Schlapbach, L.; Züttel, A. Hydrogen-Storage Materials for Mobile Applications. *Nature* **2001**, *414*, 353-358.

(16) Irani, R. S. Hydrogen Storage: High-Pressure Gas Containment. *MRS Bull* **2002**, *27*, 680-682.

(17) Centrone, A.; Brambilla, L.; Zerbi, G. Adsorption of H_2 on Carbon-Based Materials: A Raman Spectroscopy Study. *Physical Review B - Condensed Matter and Materials Physics* **2005**, *71*.

(18) Dillon, A. C.; Heben, M. J. Hydrogen Storage using Carbon Adsorbents: Past, Present and Future. *Applied Physics A: Materials Science and Processing* **2001**, *72*, 133-142.

(19) Rosi, N. L.; Eckert, J.; Eddaoudi, M.; Vodak, D. T.; Kim, J.; O'Keeffe, M.; Yaghi, O. M. Hydrogen Storage in Microporous Metal-Organic Frameworks. *Science* **2003**, *300*, 1127-1129.

(20) Yang, J.; Sudik, A.; Wolverton, C.; Siegel, D. J. High Capacity Hydrogen Storage Materials: Attributes for Automotive Applications and Techniques for Materials Discovery. *Chem. Soc. Rev.* **2010**, *39*, 656-675.

(21) Schüth, F.; Bogdanovic, B.; Felderhoff, M. Light Metal Hydrides and Complex Hydrides for Hydrogen Storage. *Chemical Communications* **2004**, , 2249-2258.

(22) Jain, I. P.; Lal, C.; Jain, A. Hydrogen Storage in mg: A most Promising Material. *Int J Hydrogen Energy* **2010**, *35*, 5133-5144.

(23) Atkins, P. In *Atkins's Physical Chemistry 7th Ed.* Oxford: 2002; , pp 108.

(24) Griessen, R. Heats of Solution and Lattice-Expansion and Trapping Energies of Hydrogen in Transition Metals. *Physical Review B* **1988**, *38*, 3690-3698.

(25) Griessen, R.; Driessen, A. Heat of Formation and Band Structure of Binary and Ternary Metal Hydrides. *Physical Review B* **1984**, *30*, 4372-4381.

(26) Bogdanovic, B.; Bohmhammel, K.; Christ, B.; Reiser, A.; Schlichte, K.; Vehlen, R.; Wolf, U. Thermodynamic Investigation of the Magnesium-Hydrogen System. *J. Alloys Compounds* **1999**, *282*, 84-92.

(27) Wagemans, R. W. P.; Van Lenthe, J. H.; De Jongh, P. E.; Van Dillen, A. J.; De Jong, K. P. Hydrogen Storage in Magnesium Clusters: Quantum Chemical Study. *J. Am. Chem. Soc.* **2005**, *127*, 16675-16680.

(28) Wu, Z.; Allendorf, M. D.; Grossman, J. C. Quantum Monte Carlo Simulation of Nanoscale MgH_2 Cluster Thermodynamics. *J. Am. Chem. Soc.* **2009**, *131*, 13918-13919.

(29) Vajeeston, P.; Ravindran, P.; Fichtner, M.; Fjellvåg, H. Influence of Crystal Structure of Bulk Phase on the Stability of Nanoscale Phases: Investigation on MgH_2 Derived Nanostructures. *Journal of Physical Chemistry C* **2012**, *116*, 18965-18972.

(30) Reilly, J. J.; Wiswall Jr., R. H. The Reaction of Hydrogen with Alloys of Magnesium and Nickel and the Formation of Mg_2NiH_4. *Inorg. Chem.* **1968**, *7*, 2254-2256.

(31) Zolliker, P.; Yvon, K.; Fischer, P.; Schefer, J. Dimagnesium Cobalt(I) Pentahydride, Mg_2CoH_5, Containing Square-Pyramidal $[CoH_5]^{4-}$ Anions. *Inorg. Chem.* **1985**, *24*, 4177-4180.

(32) Didisheim, J. J.; Zolliker, P.; Yvon, K.; Fischer, P.; Schefer, J.; Gubelmann, M.; Williams, A. F. Dimagnesium Iron (II) Hydride, Mg_2FeH_6, Containing Octahedral $[FeH_6]^{4-}$ Anions. *Inorg. Chem.* **1984**, *23*, 1953-1957.

(33) Moser, D.; Bull, D. J.; Sato, T.; Noréus, D.; Kyoi, D.; Sakai, T.; Kitamura, N.; Yusa, H.; Taniguchi, T.; Kalisvaart, W. P.; Notten, P. Structure and Stability of High Pressure Synthesized Mg-TM Hydrides (TM = Ti, Zr, Hf, V, Nb and Ta) as Possible New Hydrogen Rich Hydrides for Hydrogen Storage. *Journal of Materials Chemistry* **2009**, *19*, 8150-8161.

(34) Fossdal, A.; Brinks, H. W.; Fichtner, M.; Hauback, B. C. Thermal Decomposition of $Mg(AlH_4)_2$ Studied by in Situ Synchrotron X-Ray Diffraction. *J. Alloys Compounds* **2005**, *404-406*, 752-756.

(35) Chlopek, K.; Frommen, C.; Léon, A.; Zabara, O.; Fichtner, M. Synthesis and Properties of Magnesium Tetrahydroborate, $Mg(BH_4)_2$. *Journal of Materials Chemistry* **2007**, *17*, 3496-3503.

(36) Reilly, J. J.; Wiswall, R. H. The Reaction of Hydrogen with Alloys of Magnesium and Copper. *Inorg. Chem.* **1967**, *6*, 2220-2223.

(37) Bouaricha, S.; Dodelet, J. P.; Guay, D.; Huot, J.; Boily, S.; Schulz, R. Hydriding Behavior of mg-Al and Leached Mg-Al Compounds Prepared by High-Energy Ball-Milling. *J. Alloys Compounds* **2000**, *297*, 282-293.

(38) Vajo, J. J.; Mertens, F.; Ahn, C. C.; Bowman Jr., R. C.; Fultz, B. Altering Hydrogen Storage Properties by Hydride Destabilization through Alloy Formation: LiH and MgH_2 Destabilized with Si. *J Phys Chem B* **2004**, *108*, 13977-13983.

(39) Jepsen, J.; Milanese, C.; Girella, A.; Lozano, G. A.; Pistidda, C.; Bellosta Von Colbe, J. M.; Marini, A.; Klassen, T.; Dornheim, M. Compaction Pressure Influence on Material Properties and Sorption Behaviour of $LiBH_4$-MgH_2 Composite. *Int J Hydrogen Energy* **2013**, *38*, 8357-8366.

(40) Ibikunle, A. A.; Sabitu, S. T.; Goudy, A. J. Kinetics and Modeling Studies of the $CaH_2/LiBH_4$, $MgH_2/LiBH_4$, $Ca(BH_4)_2$ and $Mg(BH_4)_2$ Systems. *J. Alloys Compounds* **2013**, *556*, 45-50.

(41) Kang, X.; Wang, K.; Zhong, Y.; Yang, B.; Wang, P. A Novel Three-Step Method for Preparation of a TiB_2-Promoted $LiBH_4$-MgH_2 Composite for Reversible Hydrogen Storage. *Physical Chemistry Chemical Physics* **2013**, *15*, 2153-2158.

(42) Song, M. Y.; Kwak, Y. J.; Shin, H. S.; Lee, S. H.; Kim, B. G. Improvement of Hydrogen-Storage Properties of MgH_2 by Ni, $LiBH_4$, and Ti Addition. *Int J Hydrogen Energy* **2013**, *38*, 1910-1917.

(43) Mao, J.; Guo, Z.; Yu, X.; Liu, H. Combined Effects of Hydrogen Back-Pressure and NbF_5 Addition on the Dehydrogenation and Rehydrogenation Kinetics of the $LiBH_4$- MgH_2 Composite System. *Int J Hydrogen Energy* **2013**, *38*, 3650-3660.

(44) Song, M. Y.; Kwon, S. N.; Kwak, Y. J.; Park, H. R. Improvement of Hydrogen-Storage Properties of MgH2 by Addition of Li_3N, $LiBH_4$, Fe and/Or Ti. *Mater. Res. Bull.* **2013**, *48*, 74-78.

(45) Fernández, A.; Deprez, E.; Friedrichs, O. A Comparative Study of the Role of Additive in the MgH_2 Vs. the $LiBH_4$-MgH_2 Hydrogen Storage System. *Int J Hydrogen Energy* **2011**, *36*, 3932-3940.

(46) Sudik, A.; Yang, J.; Siegel, D. J.; Wolverton, C.; Carter, R. O.; Drews, A. R. Impact of Stoichiometry on the Hydrogen Storage Properties of $LiNH_2$-$LiBH_4$-MgH_2 Ternary Composites. *Journal of Physical Chemistry C* **2009**, *113*, 2004-2013.

(47) Bösenberg, U.; Ravnsbæk, D. B.; Hagemann, H.; D'Anna, V.; Minella, C. B.; Pistidda, C.; Van Beek, W.; Jensen, T. R.; Bormann, R.; Dornheim, M. Pressure and Temperature Influence on the Desorption Pathway of the $LiBH_4$-MgH_2 Composite System. *Journal of Physical Chemistry C* **2010**, *114*, 15212-15217.

(48) Crosby, K.; Shaw, L. L. Dehydriding and Re-Hydriding Properties of High-Energy Ball Milled $LiBH_4$ + MgH_2 Mixtures. *Int J Hydrogen Energy* **2010**, *35*, 7519-7529.

(49) Bösenberg, U.; Kim, J. W.; Gosslar, D.; Eigen, N.; Jensen, T. R.; von Colbe, J. M. B.; Zhou, Y.; Dahms, M.; Kim, D. H.; Günther, R.; Cho, Y. W.; Oh, K. H.; Klassen, T.; Bormann, R.; Dornheim, M. Role of Additives in $LiBH_4$-MgH_2 Reactive Hydride Composites for Sorption Kinetics. *Acta Materialia* **2010**, *58*, 3381-3389.

(50) Huot, J. In *Metal Hydrides;* Hirscher, M., Ed.; Handbook of Hydrogen Storage; Wiley-vch: Weinheim, 2010; pp 81.

(51) Cook, L. P.; Klein, R.; Wong-Ng, W.; Huang, Q.; Ribeiro, R. A.; Canfield, P. C. Thermodynamics of MgB_2 - by Calorimetry and Knudsen Thermogravimetry. *IEEE Trans. Appl. Supercond.* **2005**, *15*, 3227-3229.

(52) Severa, G.; Rönnebro, E.; Jensen, C. M. Direct Hydrogenation of Magnesium Boride to Magnesium Borohydride: Demonstration of >11 Weight Percent Reversible Hydrogen Storage. *Chemical Communications* **2010**, *46*, 421-423.

(53) Smith, J. F.; Christian, J. L. Thermodynamics of Formation of Coppermagnesium and Nickelmagnesium Compounds from Vapor Pressure Measurements. *Acta Metallurgica* **1960**, *8*, 249-255.

(54) Dornheim, M.; Doppiu, S.; Barkhordarian, G.; Boesenberg, U.; Klassen, T.; Gutfleisch, O.; Bormann, R. Hydrogen Storage in Magnesium-Based Hydrides and Hydride Composites. *Scr. Mater.* **2007**, *56*, 841-846.

(55) Luo, Y.; Cheng, J. In *Bond dissociation energies;* Haynes, W. M., Ed.; Handbook of Chemistry and Physics 94th ed. CRC: 2013; Vol. 94, pp 9-65.

(56) Schlapbach, L.; Shaltiel, D.; Oelhafen, P. Catalytic Effect in the Hydrogenation of mg and mg Compounds: Surface Analysis of Mg-Mg_2Ni and Mg_2Ni. *Mater. Res. Bull.* **1979**, *14*, 1235-1246.

(57) Zidan, R.; Slattery, D. K.; Burns, J. Study of Chemically Synthesized Mg-MgH_2 for Hydrogen Storage. *Int J Hydrogen Energy* **1991**, *16*, 821-827.

(58) Du, A. J.; Smith, S. C.; Yao, X. D.; Lu, G. Q. Hydrogen Spillover Mechanism on a Pd-Doped mg Surface as Revealed by Ab Initio Density Functional Calculation. *J. Am. Chem. Soc.* **2007**, *129*, 10201-10204.

(59) Zaluska, A.; Zaluski, L.; Ström-Olsen, J. O. Nanocrystalline Magnesium for Hydrogen Storage. *J. Alloys Compounds* **1999**, *288*, 217-225.

(60) Barkhordarian, G.; Klassen, T.; Bormann, R. Kinetic Investigation of the Effect of Milling Time on the Hydrogen Sorption Reaction of Magnesium Catalyzed with Different Nb_2O_5 Contents. *J. Alloys Compounds* **2006**, *407*, 249-255.

(61) Burda, C.; Chen, X.; Narayanan, R.; El-Sayed, M. A. Chemistry and Properties of Nanocrystals of Different Shapes. *Chem. Rev.* **2005**, *105*, 1025-1102.

(62) Bérubé, V.; Radtke, G.; Dresselhaus, M.; Chen, G. Size Effects on the Hydrogen Storage Properties of Nanostructured Metal Hydrides: A Review. *Int. J. Energy Res.* **2007**, *31*, 637-663.

(63) Chen, X.; Li, C.; Grätzel, M.; Kostecki, R.; Mao, S. S. Nanomaterials for Renewable Energy Production and Storage. *Chem. Soc. Rev.* **2012**, *41*, 7909-7937.

(64) Mooij, L.; Dam, B. Hysteresis and the Role of Nucleation and Growth in the Hydrogenation of mg Nanolayers. *Physical Chemistry Chemical Physics* **2013**, *15*, 2782-2792.

(65) Mooij, L.; Dam, B. Nucleation and Growth Mechanisms of Nano Magnesium Hydride from the Hydrogen Sorption Kinetics. *Physical Chemistry Chemical Physics* **2013**, *15*, 11501-11510.

(66) Huot, J.; Liang, G.; Boily, S.; Van Neste, A.; Schulz, R. Structural Study and Hydrogen Sorption Kinetics of Ball-Milled Magnesium Hydride. *J. Alloys Compounds* **1999**, *293*, 495-500.

(67) Jung, K. S.; Lee, E. Y.; Lee, K. S. Catalytic Effects of Metal Oxide on Hydrogen Absorption of Magnesium Metal Hydride. *J. Alloys Compounds* **2006**, *421*, 179-184.

(68) Guoxian, L.; Erde, W.; Shoushi, F. Hydrogen Absorption and Desorption Characteristics of Mechanically Milled $Mg_{35wt.\%}$ $FeTi_{1.2}$ Powders. *J. Alloys Compounds* **1995**, *223*, 111-114.

(69) Song, M.; Bobet, J. L.; Darriet, B. Improvement in Hydrogen Sorption Properties of mg by Reactive Mechanical Grinding with Cr_2O_3, Al_2O_3 and CeO_2. *J. Alloys Compounds* **2002**, *340*, 256-262.

(70) Tran, N. E.; Lambrakos, S. G.; Imam, M. A. Analyses of Hydrogen Sorption Kinetics and Thermodynamics of Magnesium-Misch Metal Alloys. *J. Alloys Compounds* **2006**, *407*, 240-248.

(71) Dehouche, Z.; Djaozandry, R.; Huot, J.; Boily, S.; Goyette, J.; Bose, T. K.; Schulz, R. Influence of Cycling on the Thermodynamic and Structure Properties of Nanocrystalline Magnesium Based Hydride. *J. Alloys Compounds* **2000**, *305*, 264-271.

(72) Bogdanovi, B.; Reiser, A.; Schlichte, K.; Spliethoff, B.; Tesche, B. Thermodynamics and Dynamics of the Mg-Fe-H System and its Potential for Thermochemical Thermal Energy Storage. *J. Alloys Compounds* **2002**, *345*, 77-89.

(73) Liang, G.; Huot, J.; Boily, S.; Van Neste, A.; Schulz, R. Catalytic Effect of Transition Metals on Hydrogen Sorption in Nanocrystalline Ball Milled MgH_2-Tm (Tm = Ti, V, Mn, Fe and Ni) Systems. *J. Alloys Compounds* **1999**, *292*, 247-252.

(74) Hanada, N.; Ichikawa, T.; Fujii, H. Catalytic Effect of Nanoparticle 3d-Transition Metals on Hydrogen Storage Properties in Magnesium Hydride MgH_2 Prepared by Mechanical Milling. *J Phys Chem B* **2005**, *109*, 7188-7194.

(75) Hanada, N.; Ichikawa, T.; Fujii, H. Catalytic Effect of Ni Nano-Particle and Nb Oxide on H-Desorption Properties in MgH_2 Prepared by Ball Milling. *J. Alloys Compounds* **2005**, *404-406*, 716-719.

(76) Wang, P.; Wang, A. M.; Zhang, H. F.; Ding, B. Z.; Hu, Z. Q. Hydrogenation Characteristics of Mg-TiO_2 (Rutile) Composite. *J. Alloys Compounds* **2000**, *313*, 218-223.

(77) Barkhordarian, G.; Klassen, T.; Bormann, R. U. Effect of Nb_2O_5 Content on Hydrogen Reaction Kinetics of Mg. *J. Alloys Compounds* **2004**, *364*, 242-246.

(78) German, R. M. Coarsening in Sintering: Grain Shape Distribution, Grain Size Distribution, and Grain Growth Kinetics in Solid-Pore Systems. *Critical Reviews in Solid State and Materials Sciences* **2010**, *35*, 263-305.

(79) Sachtler, W. M. H. Metal Clusters in Zeolites: An Intriguing Class of Catalysts. *Acc. Chem. Res.* **1993**, *26*, 383-387.

(80) Toebes, M. L.; Zhang, Y.; Hájek, J.; Alexander Nijhuis, T.; Bitter, J. H.; Jos Van Dillen, A.; Murzin, D. Y.; Koningsberger, D. C.; De Jong, K. P. Support Effects in the Hydrogenation of Cinnamaldehyde Over Carbon Nanofiber-Supported Platinum Catalysts: Characterization and Catalysis. *Journal of Catalysis* **2004**, *226*, 215-225.

(81) De Jongh, P. E.; Adelhelm, P. Nanosizing and Nanoconfinement: New Strategies Towards Meeting Hydrogen Storage Goals. *ChemSusChem* **2010**, *3*, 1332-1348.

(82) Nielsen, T. K.; Besenbacher, F.; Jensen, T. R. Nanoconfined Hydrides for Energy Storage. *Nanoscale* **2011**, *3*, 2086-2098.

(83) Fichtner, M. Nanoconfinement Effects in Energy Storage Materials. *Physical Chemistry Chemical Physics* **2011**, *13*, 21186-21195.

(84) Zou, Y.; Xiang, C.; Qiu, S.; Chu, H.; Sun, L.; Xu, F. Nanoconfined Materials for Hydrogen Storage. *Progress in Chemistry* **2013**, *25*, 115-121.

(85) Miland, H.; Ulleberg, O. Testing of a Small-Scale Stand-Alone Power System Based on Solar Energy and Hydrogen. *Solar Energy* **2012**, *86*, 666-680.

(86) Chen, B. H.; Kuo, C. H.; Ku, J. R.; Yan, P. S.; Huang, C. J.; Jeng, M. S.; Tsau, F. H. Highly Improved with Hydrogen Storage Capacity and Fast Kinetics in Mg-Based Nanocomposites by CNTs. *J. Alloys Compounds* **2013**, *568*, 78-83.

(87) Kadri, A.; Jia, Y.; Chen, Z.; Yao, X. Effect of Titanium Based Complex Catalyst and Carbon Nanotubes on Hydrogen Storage Performance of Magnesium. *Science China Chemistry* **2013**, *56*, 451-458.

(88) Kodi Pandyan, R.; Seenithurai, S.; Mahendran, M. Hydrogen Storage in MgH_2 Coated Single Walled Carbon Nanotubes. *Int J Hydrogen Energy* **2011**, *36*, 3007-3015.

(89) Ranjbar, A.; Ismail, M.; Guo, Z. P.; Yu, X. B.; Liu, H. K. Effects of CNTs on the Hydrogen Storage Properties of MgH_2 and MgH_2-BCC Composite. *Int J Hydrogen Energy* **2010**, *35*, 7821-7826.

(90) Schaller, R.; Mari, D.; dos Santos, S. M.; Tkalcec, I.; Carreño-Morelli, E. Investigation of Hydrogen Storage in Carbon Nanotube-Magnesium Matrix Composites. *Materials Science and Engineering A* **2009**, *521-522*, 147-150.

(91) Yao, X.; Wu, C. Z.; Du, A. J.; He, Y.; Smith, S. C.; Cheng, H. M.; Lu, G. Q. In *In Carbon nanotubes enhanced hydrogen ab/desorption in Magnesium-based nanocomposites;* Proceedings of the 2006 International Conference on Nanoscience and Nanotechnology, ICONN; 2006; , pp 206-209.

(92) Baldé, C. P.; Hereijgers, B. P. C.; Bitter, J. H.; De Jong, K. P. Facilitated Hydrogen Storage in $NaAlH_4$ Supported on Carbon Nanofibers. *Angewandte Chemie - International Edition* **2006**, *45*, 3501-3503.

(93) Konarova, M.; Tanksale, A.; Norberto Beltramini, J.; Qing Lu, G. Effects of Nano-Confinement on the Hydrogen Desorption Properties of MgH_2. *Nano Energy* **2013**, *2*, 98-104.

(94) Zlotea, C.; Chevalier-César, C.; Léonel, E.; Leroy, E.; Cuevas, F.; Dibandjo, P.; Vix-Guterl, C.; Martens, T.; Latroche, M. Synthesis of Small Metallic Mg-Based Nanoparticles Confined in Porous Carbon Materials for Hydrogen Sorption. *Faraday Discuss.* **2011**, *151*, 117-131.

(95) Kubota, A.; Miyaoka, H.; Tsubota, M.; Shimoda, K.; Ichikawa, T.; Kojima, Y. Synthesis and Characterization of Magnesium-Carbon Compounds for Hydrogen Storage. *Carbon* **2013**, *56*, 50-55.

(96) Jia, Y.; Zou, J.; Yao, X. Catalytically Enhanced Dehydrogenation of MgH_2 by Activated Carbon Supported Pd-VO_x (x=2.38) Nanocatalyst. *Int J Hydrogen Energy* **2012**, *37*, 13393-13399.

(97) Grigorova, E.; Mandzhukova, T.; Khristov, M.; Tzvetkov, P.; Tsyntsarski, B. Effect of Activated Carbons Derived from Agricultural by-Products on the Hydrogen Storage Properties of Magnesium. *Bulgarian Chemical Communications* **2011**, *43*, 483-488.

(98) Sartori, S.; Knudsen, K. D.; Zhao-Karger, Z.; Bardaij, E. G.; Fichtner, M.; Hauback, B. C. Small-Angle Scattering Investigations of Mg-Borohydride Infiltrated in Activated Carbon. *Nanotechnology* **2009**, *20*, 505702.

(99) Bogerd, R.; Adelhelm, P.; Meeldijk, J. H.; De Jong, K. P.; De Jongh, P. E. The Structural Characterization and H_2 Sorption Properties of Carbon-Supported $Mg_{1-x}Ni_x$ Nanocrystallites. *Nanotechnology* **2009**, *20*, 204019.

(100) Rud, A. D.; Lakhnik, A. M.; Ivanchenko, V. G.; Uvarov, V. N.; Shkola, A. A.; Dekhtyarenko, V. A.; Ivaschuk, L. I.; Kuskova, N. I. Hydrogen Storage of the Mg-C Composites. *Int J Hydrogen Energy* **2008**, *33*, 1310-1316.

(101) Huang, Z. G.; Guo, Z. P.; Calka, A.; Wexler, D.; Liu, H. K. Improvement in Hydrogen Cycling Properties of Magnesium through Added Graphite. *Mater Lett* **2007**, *61*, 3163-3166.

(102) Lototskyy, M.; Sibanyoni, J. M.; Denys, R. V.; Williams, M.; Pollet, B. G.; Yartys, V. A. Magnesium-Carbon Hydrogen Storage Hybrid Materials Produced by Reactive Ball Milling in Hydrogen. *Carbon* **2013**, *57*, 146-160.

(103) Nielsen, T. K.; Manickam, K.; Hirscher, M.; Besenbacher, F.; Jensen, T. R. Confinement of MgH_2 Nanoclusters within Nanoporous Aerogel Scaffold Materials. *ACS Nano* **2009**, *3*, 3521-3528.

(104) Zhang, S.; Gross, A. F.; Van Atta, S. L.; Lopez, M.; Liu, P.; Ahn, C. C.; Vajo, J. J.; Jensen, C. M. The Synthesis and Hydrogen Storage Properties of a MgH_2 Incorporated Carbon Aerogel Scaffold. *Nanotechnology* **2009**, *20*, 204027.

(105) Liu, Y.; Zou, J.; Zeng, X.; Wu, X.; Tian, H.; Ding, W.; Wang, J.; Walter, A. Study on Hydrogen Storage Properties of Mg Nanoparticles Confined in Carbon Aerogels. *Int J Hydrogen Energy* **2013**, *38*, 5302-5308.

(106) Ngene, P.; Adelhelm, P.; Beale, A. M.; De Jong, K. P.; De Jongh, P. E. $LiBH_4$/SBA-15 Nanocomposites Prepared by Melt Infiltration Under Hydrogen Pressure: Synthesis and Hydrogen Sorption Properties. *Journal of Physical Chemistry C* **2010**, *114*, 6163-6168.

(107) Gutowska, A.; Li, L.; Shin, Y.; Wang, C. M.; Li, X. S.; Linehan, J. C.; Smith, R. S.; Kay, B. D.; Schmid, B.; Shaw, W.; Gutowski, M.; Autrey, T. Nanoscaffold Mediates Hydrogen Release and the Reactivity of Ammonia Borane. *Angewandte Chemie - International Edition* **2005**, *44*, 3578-3582.

(108) Wang, H.; Zhang, S. F.; Liu, J. W.; Ouyang, L. Z.; Zhu, M. Enhanced Dehydrogenation of Nanoscale MgH_2 Confined by Ordered Mesoporous Silica. *Mater. Chem. Phys.* **2012**, *136*, 146-150.

(109) Yang, Y.; Chiang, K.; Burke, N. Porous Carbon-Supported Catalysts for Energy and Environmental Applications: A Short Review. *Catalysis Today* **2011**, *178*, 197-205.

(110) Choi, W. C.; Woo, S. I.; Jeon, M. K.; Sohn, J. M.; Kim, M. R.; Jeon, H. J. Platinum Nanoclusters Studded in the Microporous Nanowalls of Ordered Mesoporous Carbon. *Adv Mater* **2005**, *17*, 446-451.

(111) Domingo-Garcia, M.; Fernández-Moráles, I.; López-Garzón, F. J. Activated Carbons as Supports for Nickel Catalysts. *Applied Catalysis A, General* **1994**, *112*, 75-85.

(112) Nijkamp, M. G.; Raaymakers, J. E. M. J.; Van Dillen, A. J.; De Jong, K. P. Hydrogen Storage using Physisorption-Materials Demands. *Applied Physics A: Materials Science and Processing* **2001**, *72*, 619-623.

(113) Gosselink, R. W.; Xia, W.; Muhler, M.; De Jong, K. P.; Bitter, J. H. Enhancing the Activity of Pd on Carbon Nanofibers for Deoxygenation of Amphiphilic Fatty Acid Molecules through Support Polarity. *ACS Catalysis* **2013**, *3*, 2397-2402.

(114) Gross, A. F.; Ahn, C. C.; Van Atta, S. L.; Liu, P.; Vajo, J. J. Fabrication and Hydrogen Sorption Behaviour of Nanoparticulate MgH_2 Incorporated in a Porous Carbon Host. *Nanotechnology* **2009**, *20*, 204005.

(115) Pekala, R. W. Organic Aerogels from the Polycondensation of Resorcinol with Formaldehyde. *J. Mater. Sci.* **1989**, *24*, 3221-3227.

(116) Li, J.; Wang, X.; Wang, Y.; Huang, Q.; Dai, C.; Gamboa, S.; Sebastian, P. J. Structure and Electrochemical Properties of Carbon Aerogels Synthesized at Ambient Temperatures as Supercapacitors. *J. Non Cryst. Solids* **2008**, *354*, 19-24.

(117) Wang, X.; Wang, X.; Liu, L.; Bai, L.; An, H.; Zheng, L.; Yi, L. Preparation and Characterization of Carbon Aerogel Microspheres by an Inverse Emulsion Polymerization. *J. Non Cryst. Solids* **2011**, *357*, 793-797.

(118) Zheng, L.; Wang, Y.; Wang, X.; Li, N.; An, H.; Chen, H.; Guo, J. The Preparation and Performance of Calcium Carbide-Derived Carbon/Polyaniline Composite Electrode Material for Supercapacitors. *J. Power Sources* **2010**, *195*, 1747-1752.

(119) Lototskyy, M.; Sibanyoni, J. M.; Denys, R. V.; Williams, M.; Pollet, B. G.; Yartys, V. A. Magnesium-Carbon Hydrogen Storage Hybrid Materials Produced by Reactive Ball Milling in Hydrogen. *Carbon* **2013**, *57*, 146-160.

(120) Kubota, A.; Miyaoka, H.; Tsubota, M.; Shimoda, K.; Ichikawa, T.; Kojima, Y. Synthesis and Characterization of Magnesium-Carbon Compounds for Hydrogen Storage. *Carbon* **2013**, *56*, 50-55.

(121) Rud, A. D.; Lakhnik, A. M. Effect of Carbon Allotropes on the Structure and Hydrogen Sorption during Reactive Ball-Milling of Mg-C Powder Mixtures. *Int J Hydrogen Energy* **2012**, *37*, 4179-4187.

(122) Rud, A. D.; Lakhnik, A. M.; Mikhailova, S. S.; Karban, O. V.; Surnin, D. V.; Gilmutdinov, F. Z. Structure of Mg-C Nanocomposites Produced by Mechano-Chemical Synthesis. *J. Alloys Compounds* **2011**, *509*, S592-S594.

(123) Spassov, T.; Zlatanova, Z.; Spassova, M.; Todorova, S. Hydrogen Sorption Properties of Ball-Milled Mg-C Nanocomposites. *Int J Hydrogen Energy* **2010**, *35*, 10396-10403.

(124) De Jongh, P. E.; Eggenhuisen, T. M. Melt Infiltration: An Emerging Technique for the Preparation of Novel Functional Nanostructured Materials. *Adv Mater* **2013**, *25*, 6672-6690.

(125) Ngene, P.; Van Zwienen, R.; De Jongh, P. E. Reversibility of the Hydrogen Desorption from $LiBH_4$: A Synergetic Effect of Nanoconfinement and Ni Addition. *Chemical Communications* **2010**, *46*, 8201-8203.

(126) Ngene, P.; Van Den Berg, R.; Verkuijlen, M. H. W.; De Jong, K. P.; De Jongh, P. E. Reversibility of the Hydrogen Desorption from $NaBH_4$ by Confinement in Nanoporous Carbon. *Energy and Environmental Science* **2011**, *4*, 4108-4115.

(127) Adelhelm, P.; Gao, J.; Verkuijlen, M. H. W.; Rongeat, C.; Herrich, M.; Van Bentum, P. J. M.; Gutfleisch, O.; Kentgens, A. P. M.; De Jong, K. P.; De Jongh, P. E. Comprehensive Study of Melt Infiltration for the Synthesis of $NaAlH_4$/C Nanocomposites. *Chemistry of Materials* **2010**, *22*, 2233-2238.

(128) De Jongh, P. E.; Wagemans, R. W. P.; Eggenhuisen, T. M.; Dauvillier, B. S.; Radstake, P. B.; Meeldijk, J. D.; Geus, J. W.; De Jong, K. P. The Preparation of Carbon-Supported Magnesium Nanoparticles using Melt Infiltration. *Chemistry of Materials* **2007**, *19*, 6052-6057.

(129) Dujardin, E.; Ebbesen, T. W.; Hiura, H.; Tanigaki, K. Capillarity and Wetting of Carbon Nanotubes. *Science* **1994**, *265*, 1850-1852.

(130) Zhang, D.; Shen, P.; Shi, L.; Jiang, Q. Wetting of B, 4C, TiC and Graphite Substrates by Molten Mg. *Mater. Chem. Phys.* **2011**, *130*, 665-671.

2. The size dependence of hydrogen mobility and sorption kinetics for carbon-supported MgH_2 particles

Abstract

MgH_2 is a promising material for reversible solid-state hydrogen storage. It is known that particle size can have a strong impact on hydrogen dynamics and sorption characteristics, but more detailed insight has been hampered by the great challenge to prepare small and well-defined particles and study their hydrogen storage properties upon cycling. The preparation of MgH_2 nanoparticles supported on high surface area carbon aerogels with pore sizes varying from 6-20 nm is reported. Two distinctly different MgH_2 particle populations were observed: XRD invisible nanoparticles with sizes below 20 nm, and larger, crystalline, MgH_2 particles. The size of the small nanoparticles was controlled by varying the pore size of the support. They released hydrogen at temperatures 140 ^{o}C lower than bulk MgH_2. The size-dependent hydrogen kinetics were for the first time corroborated by intrinsic hydrogen dynamics data obtained by solid state ^{1}H NMR. The rapid hydrogen release and absorption in the small MgH_2 nanoparticles allowed a selective study of their sorption properties. Fast cycling was possible (80% of the capacity absorbed within 15 minutes at 18 bar and 300 °C), and full stability of both capacity and hydrogen release temperature upon cycling was observed, showing that the growth of the nanoparticles is effectively prevented by the carbon support. A clear correlation was found between the hydrogen desorption temperature and the size of the MgH_2 nanoparticles. This illustrates the potential of the use of supported nanoparticles for fast, reversible and stable hydrogen cycling.

2.1. Introduction

Nowadays, more than 60% of the energy is obtained from fossil fuels [1]. The current status of the world-wide energy reserves and increasing energy consumption makes it necessary to move towards alternative sources for energy production. Renewable energy sources, like solar and wind energy, are required to deal with the current environmental issues, such as global warming. The renewable energy sources usually provide electricity while fuels are also needed as energy carrier for off-grid applications. Hydrogen is proposed as alternative energy carrier [2]. However, an important challenge is the reversible storage of hydrogen, which has to be done safely and with high density. Hydrogen storage in metals or other solid compounds has the potential to satisfy these conditions.

MgH_2 has been widely studied as a potential hydrogen storage material. The low cost of the material and its high hydrogen storage capacity of 7.6 wt% are interesting for stationary and mobile energy storage applications. MgH_2 can store hydrogen reversibly following the reaction:

$$Mg\ (s) + H_2\ (g) \leftrightarrow MgH_2\ (s) \qquad \text{(Eq. 2 - 1)}$$

The related decomposition enthalpy is 75 $kJ \cdot mol^{-1}$ H_2 [3, 4], which means that hydrogen release only occurs above 300 ^oC at 1 bar H_2, which is the thermodynamic equilibrium temperature for the reaction at that pressure. The high operation temperature is a drawback; however, this will not be a problem if the material can be combined with exothermic processes [5]. Prototypes of storage tanks with efficient heat management have already been realized [6]. Nonetheless, thermodynamic and kinetic enhancement of the Mg-system is still desirable for mobile applications.

Modification of the reaction equilibrium is often obtained by adding other compounds. The compounds either form a stable Mg-alloy upon dehydrogenation or involve a ternary hydride. Examples of these systems include Mg-Al [7] or Mg_2NiH_4 [8], but the enthalpy required to decompose the hydrides is still high in the range of 60 $kJ \cdot mol^{-1}$ H_2. Computational studies have predicted that MgH_2-clusters consisting of few atoms would have lower thermodynamic stability [9-11]. However, experimental results only show modest changes in the thermodynamic equilibrium, since the less positive value for the enthalpy for desorption is being counteracted by a less positive value for the entropy change [12].

Another issue is the slow reaction kinetics. The kinetic properties can be changed by modifying the size of the Mg particles. Decreasing the particle size to nanoscale enhances the reaction kinetics due to a larger surface-to-volume ratio of the particle and decreased solid-state diffusion distances for hydrogen [13]. However, so far it is not clear what the rate-limiting step is for hydrogen release and which effect dominates the kinetic enhancement or whether both effects are contributing.

Different approaches have been investigated to synthesize nanostructured MgH_2. Ball milling with addition of catalysts is often used to create nanostructured materials. For example, addition of metals such as Pd and Ni or metal oxides like Nb_2O_5 has proven to be quite effective [14-20]. Despite the kinetic enhancement, high temperatures are still required for the hydrogen sorption reactions to occur. Particle growth occurs at these elevated temperatures and deteriorates the kinetic properties [21]. To prevent particle growth, direct inter-particle contact has to be avoided. One strategy to achieve this is to anchor nanoparticles on porous and/or high surface area support materials. The porous structure of the support material allows potentially control over the particle size [22-25].

In this study the importance of size effects on the hydrogen sorption kinetics in Mg and MgH_2 is shown. To gain more insight in the kinetic behavior of pure $Mg(H_2)$ nanoparticles, carbon supports with different pore size distributions were used and a significant fraction of MgH_2 nanoparticles limited to a specific size range between 6-20 nm were obtained. The use of carbons with different pore sizes allowed for the first time systematic control over the nanoparticle size of MgH_2. The supported MgH_2 nanoparticles exhibit remarkably different hydrogen sorption properties compared to bulk MgH_2 and this coincides with different intrinsic H-mobilities as determined with ^1H solid-state NMR.

2.2. Experimental

2.2.1. Preparation of the carbon aerogels

The carbon aerogels (CAs) were synthesized through resorcinol-formaldehyde condensation catalyzed by sodium carbonate, as reported by Pekala et al. [26]. Resorcinol (Sigma Aldrich 99%, 8.65 g, 79 mmol), formaldehyde (Fisher chemical, analytical reagent 37-41%, stabilized by 12% methanol, 12.89 g, 158 mmol) and sodium carbonate (Across organics 99.5%, 0.017 g, 0.16

mmol) were dissolved in deionized water. In order to obtain CAs with different pore size distributions, the amount of water was varied from 40, 45, 50 to 55 wt% with respect to the total weight including the weight of the resorcinol-formaldehyde mixture. After aging (1 day at room temperature, 1 day at 60 ^{o}C and 3 days at 90 ^{o}C) the samples were cooled, powdered and immersed in acetone to replace the water inside the pores of the formed polymer (3 times, soak time: 1 h, 1 h, 8 h) as described by Li et al. [27]. The samples were dried at room temperature and then pyrolyzed in a tubular oven at 800 ^{o}C for 10 hours in an Ar-flow. All CA samples were stored in an Ar-glovebox (MBraunLabmaster) and all further preparation steps and measurements were performed in inert atmosphere.

2.2.2 Preparation of MgH_2/CA nanocomposites

In a typical experiment, 900 mg of CA was mixed and ground with 100 mg of MgH_2 (Alfa Aesar (98%)) in a mortar, to obtain a 10 wt% MgH_2/CA mixture. The mixture was placed in a graphite cup, which was placed inside a closed stainless steel sample holder, and was heated in a tubular oven with 10 ^{o}C·min^{-1} to 658 ^{o}C and kept at the maximum temperature for 24 min under an Ar flow. Hydrogenation of the samples was performed at 80 bar H_2, 300 ^{o}C for 10 hours in an autoclave (Parr). The hydrogenated samples were used for structural characterization, NMR and dehydrogenation experiments.

2.2.3 Characterization

Porosity measurements on the carbon aerogels and MgH_2/CA nanocomposites were performed by N_2-physisorption. The samples were loaded in airtight-quartz tubes inside the glove box and measured at -196 ^{o}C, using a Micromeritics Tristar 3000 apparatus. The pore size distributions of the samples were obtained by performing Barrett-Joyner-Halenda (BJH) analysis using a Carbon Black thickness-equation as reference on the adsorption branch. The total pore volume was obtained at p/p_0 = 0.997. For removal of Mg species, the sample was stirred in an aqueous HCl solution (pH ~ 2.5) overnight at room temperature, followed by filtering and drying in Ar at 200 ^{o}C overnight before this sample was measured.

X-ray diffraction (XRD) patterns were obtained at room temperature from 25^{o} to 105^{o} 2θ (Bruker D8 Advance equipped with VANTEC-1 detector using $Co_{K\alpha1,2}$ radiation) with a step size of 0.1^{o} per step and an acquisition time of 2 s per step. The samples were measured in an airtight

sample holder. For quantitative analysis, Si-powder (Sigma Aldrich, 99.9%) was added as internal standard and Rietveld refinement was performed with the Rietica program [28].

Differential scanning calorimetry (DSC) measurements were carried out on a physical mixture of MgH_2 and CA (Mettler Toledo HP-DSC 1). Graphite sample holders (TA instruments (40 µl)) were used and loaded with approximately 10 mg of sample. The sample was heated from room temperature to 680 ^oC followed by a cooling step to room temperature with 5 $^oC \cdot min^{-1}$ in an Ar-flow of 20 $ml \cdot min^{-1}$.

Transmission electron microscopy (TEM) analysis was performed using an FEI Tecnai 20F FEG microscope operated at 200 kV. Images were obtained in bright field mode with energy-dispersive X-ray spectroscopy (EDX) performed during the same measurement. The samples were prepared by grinding in a mortar extensively, before the dry powders were applied on a 200 mesh copper grid with a carbon coated polymer film in the glove box. The samples were exposed to air for no more than 5 sec during insertion of the probe into the electron microscope. Histograms for the average size of the nanoparticles were obtained by measuring manually ~150 particles below 20 nm.

2.2.4 Hydrogen sorption measurements

The hydrogen desorption properties of the MgH_2/CA composites were studied with temperature programmed desorption (TPD) using a Micromeritics AutoChem II 2920 apparatus equipped with a TCD detector. Approximately 100 mg of the sample was used for each measurement. The samples were heated up to 450 ^oC with 5 $^oC \cdot min^{-1}$ in 25 $ml \cdot min^{-1}$ Ar- flow.

The hydrogen absorption kinetics were measured directly on the as prepared Mg/CA samples using a Sievert apparatus (Setaram PCT PRO-2000). A steel holder was used (~4.8 ml), where the inner walls were covered with graphite foil (PAPYEX®) to avoid side reactions. The hydrogen absorption conditions were 300 ^oC at ~18 bar H_2 pressure for 3 hours. Before starting the next absorption cycle, the sample was kept at 300 ^oC in vacuum for several hours to allow full hydrogen desorption from the samples.

2.2.5 NMR spectroscopy

Wideline ^1H NMR spectra were recorded at room temperature without sample rotation on a Bruker DRX200 spectrometer operating at a ^1H NMR frequency of 200 MHz, and equipped with

a probe head with a 5 mm horizontal coil. To obtain undistorted line shapes, a magic-sandwich-echo pulse sequence preceded by two 90° pulses was employed with alternatingly same and opposite phases [29]:

$$90^{o}_{+x}90^{o}_{\pm x}\text{-}\ T\ \text{-}\ 90^{o}_{\varphi}\ \text{-}\ \tau\ \text{-}\ 90^{o}_{\psi}\ \text{-}\ (\tau_{MSE}\ \text{-}\ 90^{o}_{\varphi}\ \text{-}\ \tau_{MSE})4\ (\tau_{MSE}\ \text{-}\ 90^{o}_{-\varphi}\ \text{-}\ \tau_{MSE})4\ \text{-}\ 90^{o}_{\psi}\ \text{-}\ \tau\ \text{-}\ \text{detection}_{\pm\varphi}$$

where the pulse phases φ and ψ are related by 90° phase shift, ψ = φ + 90°. The 90° pulse duration was 2 μs, and the pulse intervals τ and τ_{MSE}, were 8 and 2 μs, respectively, whereby τ also includes the pre-detection delay of 5.5 μs. Combined with a proper phase cycle of φ and ψ, the initial $90°_{+x}$- $90°_{\pm x}$ pulse pair effectively prevents the accumulation of the tail of the last pulse into the first points of the echo and ensures a flat baseline in this way. For quantitative purpose the (z-filter) time *T* following the initial two pulses was taken 10 ms, which is large compared to proton transversal relaxation T_2, but negligibly short with respect to the spin-lattice relaxation T_1. T_1 – weighed spectra were recorded with T = 1 s, and T_1 relaxation was measured by varying T. The relaxation delay between subsequent NMR scans was taken 3600 s for bulk MgH_2 and 900 s for the nanocomposites.

Table 2 - 1: The average pore diameters of the carbon scaffold and the average small nanoparticle (SNP) size of MgH_2 are shown. The mesopore volumes before and after addition of Mg; and after removal of Mg are also reported.

Sample	Avg. Pore Size (nm)	V_{meso} ($cm^3 \cdot g^{-1}$)	$V_{meso}MgH_2$ ($cm^3 \cdot g^{-1}$)	Avg. MgH_2 SNPs size (nm)
CA-6	6	0.16	0.11	6.3(±1.8)
CA-9	9	0.46	0.33	7.2(±2.1)
CA-9 leached	9	0.45	-	-
CA-12	12	0.72	0.65	9.2(±2.0)
CA-20	20	1.14	0.97	12.9(±3.0)

3. Results and discussion

2.3.1 MgH_2-carbon aerogel nanocomposites

The average pore diameters of the carbon supports were calculated by averaging the volume contribution of the available mesopores (2-50 nm) from the mesopore size distribution as

determined by N_2-physisorption (Fig. 2 - 1: left). This resulted in average pore sizes of 6 nm, 9 nm, 12 nm and 20 nm (Table 2 - 1).

Fig. 2 - 1: right shows the result of the in-situ study on the heat treatment of a physical mixture of MgH_2 with CA performed with DSC. Upon heating, an endothermic event with an onset temperature near 430 ^oC was observed. This was due to the decomposition of MgH_2 to metallic Mg. Another endothermic event occurred around 650 ^oC, which is the melting point of Mg. During cooling, an exothermic signal was observed with the same onset temperature as the melting point corresponding to solidification of Mg. This peak was broader compared to the peak observed during melting probably due to nucleation required for recrystallization. No other peaks were found indicating that no reaction took place between Mg and the carbon support during the heat treatment.

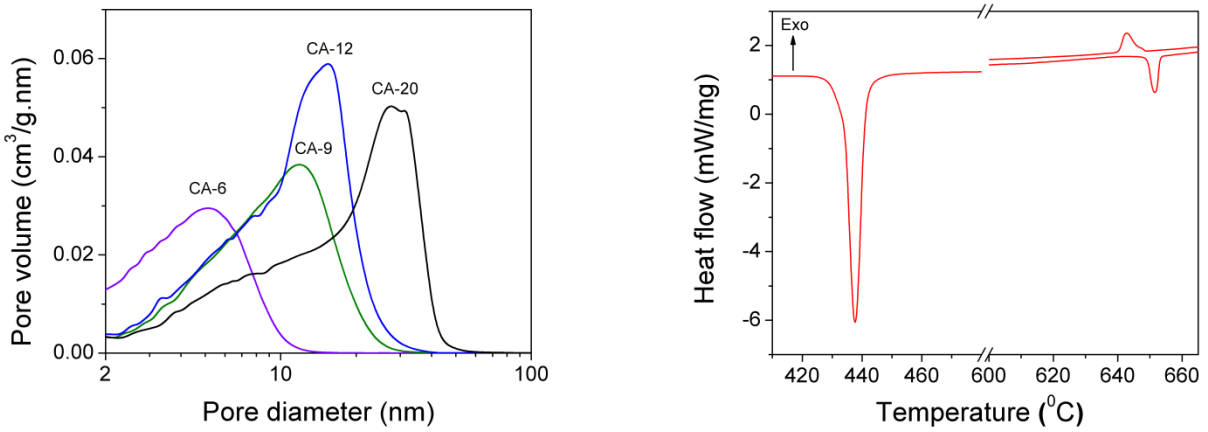

Fig. 2 - 1: Left: Pore size distribution of four different CA supports. The average pore diameters are 6, 9, 12, and 20 nm respectively. Right: DSC measurement starting with a 10 wt% MgH_2 and CA-9 physical mixture heated under Ar with 5 $^oC \cdot min^{-1}$. Around 435 ^oC the endothermic decomposition of MgH_2 to Mg is observed and around 650 ^oC the melting of Mg and subsequent exothermic solidification during cooling occurred.

The carbon supports were non-crystalline and X-ray diffraction only showed one broad diffraction peak around 50^o (Fig. 2 - 2(a): left). Fig. 2 - 2(b): left shows a physical mixture of the CA support with 10 wt% pure MgH_2. The X-ray pattern of the Mg-CA sample after heat treatment (Fig. 2 - 2(c): left) only had peaks belonging to the hexagonal Mg phase ($P6_3/mmc$) and the broad peak corresponding to the amorphous carbon aerogel. The presence of sharp Mg diffraction lines indicated that crystalline Mg is present. After hydrogenation, X-ray diffraction was measured again and Fig. 2 - 2(d): left shows that new diffraction lines appeared belonging to

the tetragonal MgH_2 phase ($P4_2/mnm$). Thus, the crystalline fraction of Mg was rehydrogenated to form MgH_2. However, the overall intensity of the diffraction lines of the nanocomposite was much lower than for a physical mixture of MgH_2 and CA (Fig. 2 - 2(b): left) with the same weight ratio. A significant fraction of MgH_2 was not detected, which is in line with earlier findings [30]. According to analysis with Rietveld refinement, 70% of the Mg added was detected as crystalline Mg (Fig. 2 - 2: right). This suggests that 30% of the Mg is nanocrystalline or amorphous and cannot be probed by XRD due to lack of long range order. Another possibility is that some Mg was evaporated during heating due to its high vapor pressure.

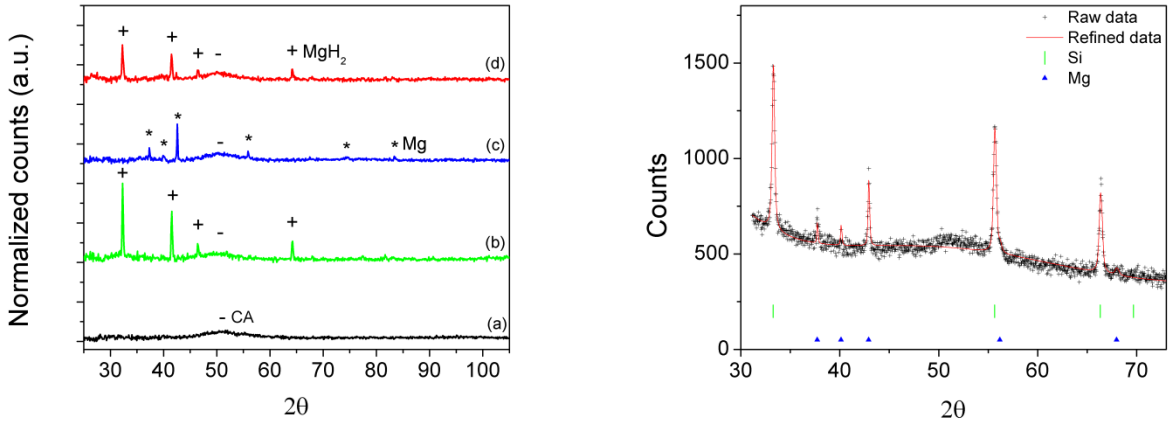

Fig. 2 - 2: Left: XRD patterns of (a) CA-9 as synthesized, (b) a physical mixture of CA-9 and 10 wt% MgH_2, (c) 10 wt% Mg/CA-9, and (d) 10 wt% MgH_2/CA-9. The used symbols indicating the diffraction lines are: CA (-), Mg (*) and MgH_2 (+). The intensities are normalized to fit in the same scale for comparison. Right: Refined X-ray diffraction pattern of 10 wt% Mg/CA-9 with Si as internal standard. 30% of Mg was not observed after heat treatment. R_p: 4.33, R_{wp}: 4.93, χ^2: 1.94.

Fig. 2 - 3 shows a bright field TEM image of the MgH_2/CA-6 composite and interestingly, many nanoparticles are observed. EDX measurements confirm that these particles are MgH_2 species (Fig. 2 - 3(b)). Additionally, the presence of large MgH_2 crystallites was confirmed by TEM. It is clear that MgH_2 particles were formed in two distinctly different size ranges: small nanoparticles (SNPs) with a size smaller than 20 nm, but also larger nanoparticles (LNPs) in the range of 100 nm that can be detected as crystalline MgH_2 with XRD. The average nanoparticle sizes of MgH_2/CA-6, MgH_2/CA-9, MgH_2/CA-12 and MgH_2/CA-20 were 6.3 nm (±1.8), 7.2 nm (±2.1), 9.2 nm (±2.0) and 12.9 nm (±3.0) respectively (Fig. 2 - 3 (d-f)). Using scaffolds with

larger pore sizes resulted in larger particles, while in all cases the resulting particle sizes were somewhat smaller than the average scaffold pore diameter.

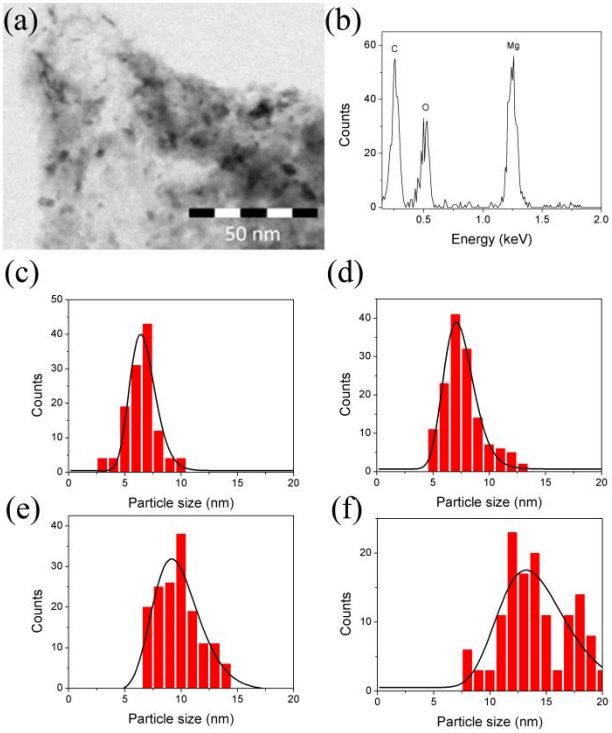

Fig. 2 - 3: (a) Bright field TEM image of MgH_2/CA-6. (b) EDX measurement on (a) and nanoparticle size distribution of MgH_2/CA-6 (c), MgH_2/CA-9 (d), MgH_2/CA-12 (e) and MgH_2/CA-20 (f).

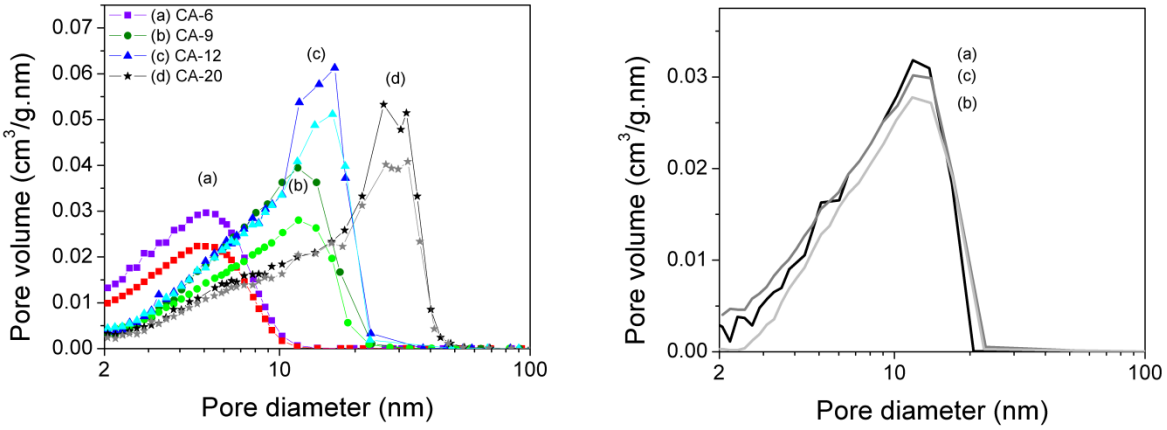

Fig. 2 - 4: Left: Pore-size distribution of CA-6 (a), CA-9 (b), CA-12 (c), and CA-20 (d). The profiles with lower intensity and matching symbols represent the Mg/CA composites. Right: Pore size distribution of CA-9 (a) as prepared (b) after Mg deposition (c) after leaching of Mg.

Table 2 - 1 summarizes the structural properties of the CA supports and the SNPs of MgH_2. Upon heat treatment with Mg, the pore volume of the CAs decreased (Fig. 2 - 4: left). The initial pore volume was recovered after removal of Mg (Fig. 2 - 4: right). Hence, deposition of Mg did not change the structure of the carbon. The decrease in pore volume is caused by Mg nanoparticles being inside the pores of CA.

2.3.2 The influence of particle size on the hydrogen release kinetics and H-mobility

The hydrogen release profile of MgH_2/CA-9 was compared to that of MgH_2 powder and MgH_2 on High Surface Area Graphite (HSAG) in Fig. 2 - 5. Pure MgH_2 (a) released hydrogen above 400 ^oC. If MgH_2 powder was physically mixed with CA, no significant change in the hydrogen release profile was observed (b). When MgH_2 was supported on HSAG-500 (c), the peak temperature was lowered to 386 ^oC. The hydrogen desorption profile of the MgH_2/CA-9 sample was quite different (Fig. 2 - 5(d)). Two peaks were observed. One peak had a maximum temperature in a similar region as HSAG-500, which was around 380 ^oC, and can probably be attributed to the hydrogen release from the LNPs of MgH_2. More interesting is the presence of a peak around 280 ^oC, which was ~140 ^oC lower than for bulk MgH_2. This desorption temperature is comparable to MgH_2 supported on CA or CMK-3, prepared by solution impregnation [31-34], and hence can probably be attributed to the SNPs of MgH_2 present in the pores of the carbon scaffold.

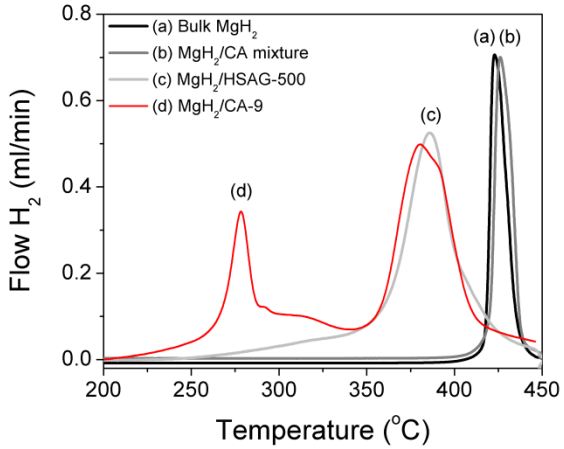

Fig. 2 - 5: Hydrogen release profiles of (a) MgH_2 powder, (b) a physical mixture of 10 wt% MgH_2 powder and CA; (c) 10wt% MgH_2 on HSAG and (d) 10wt% MgH_2/CA-9

This is further supported by the fact that there was a modest, but significant, shift of the low temperature release for the different MgH_2/CA composites (Fig. 2 - 6: left). The lowest peak temperature was observed for CA-6, which is the carbon support with the smallest average pore size, followed by CA-9, CA-12 and CA-20 with the peak maximum at the highest temperature. This trend is visualized in Fig. 2 - 6: right, which shows the maximum peak temperatures against the average size of the MgH_2 nanoparticles (Fig. 2 - 3).

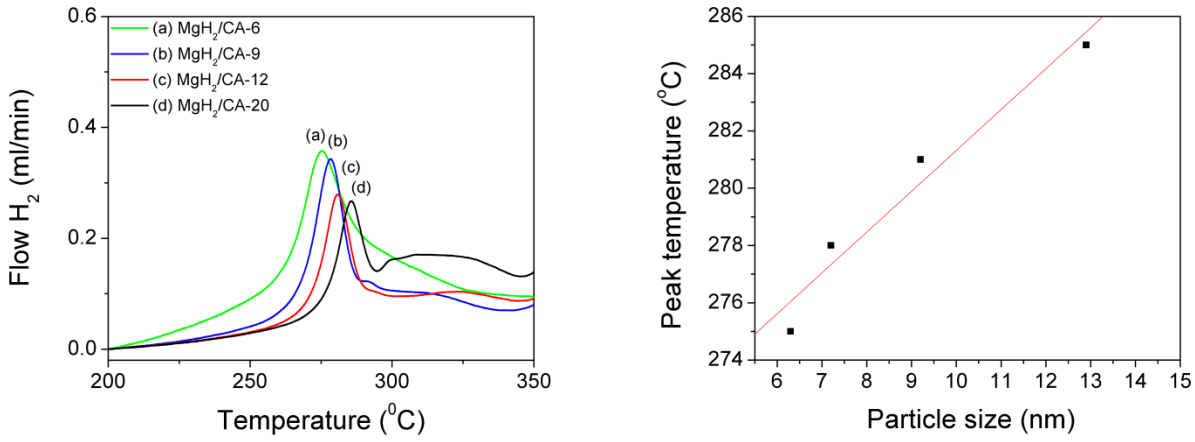

Fig. 2 - 6: Left: Hydrogen release profiles of 10 wt% MgH_2 on (a) CA-6, (b) CA-9, (c) CA-12 and (d) CA-20. Right: Relation between peak temperature and average nanoparticle size for hydrogen desorption.

In all samples, MgH_2 was the only phase that could release hydrogen, as no impurities were detected. A significant shift in equilibrium decomposition temperature is unlikely in this size range, so the correlation between size and temperature shift is most likely a kinetic effect, but the exact underlying cause of this correlation is not fully understood. It is generally postulated that either the surface association/dissociation of hydrogen, and/or slow solid state hydrogen diffusion are rate-limiting steps [25]. Therefore, the hydrogen dynamics for the different particle sizes were studied. These can be measured by solid-state $^{1,2}H$ NMR; a powerful tool to investigate nanostructured phases as it does not depend on long range order, but probes local properties [35].

Fig. 2 - 7(a-d) shows static ^1H NMR spectra of the composites MgH_2/CA-6, MgH_2/CA-9, MgH_2/CA-12 and MgH_2/CA-20 (thick black lines). The NMR line shapes were broad (FWHH ~20 kHz) as result of the strong dipole coupling between ^1H nuclei in the MgH_2 nanodomains. However, these were not as broad as the static NMR line shape of bulk MgH_2 (FWHH ~ 40 kHz), which has been superimposed (grey lines) on the spectra of the four composites in Fig. 2 -

7(a-d), for comparison. The significantly narrower ^{1}H NMR resonances of the nanocomposites reflected the motional-averaging effect caused by hydrogen mobility inside the MgH_2 nanodomains. The more mobile the hydrogen atoms, the more their (average) dipole interactions are reduced and the narrower the ^{1}H NMR resonance become.

The increased hydrogen mobility in the nanocomposites was confirmed by ^{1}H NMR spin-lattice relaxation, which is sensitive to mobility at the 10^{-12}-10^{-8} s^{-1} timescale. The higher the mobility, the faster this type of relaxation becomes. Indeed, the spin-lattice relaxation was extremely slow in bulk MgH_2 (Fig. 2 - 7(e)), and three orders of magnitude faster in the nanocomposites (Fig. 2 - 7(f)). However, the faster relaxation in the nanocomposites cannot be exclusively attributed to hydrogen mobility alone, since it was a combined result of hydrogen mobility, the presence of paramagnetic centers in the carbon support and short ^{1}H spin-diffusion distances in the nanocomposites.

Detailed comparison of the NMR line shape of the nanocomposites with that of bulk MgH_2 (Fig. 2 - 7(a-d)) suggests that the nanocomposite spectra actually reflect a superposition of a relatively narrow and wide (bulk-like) component. This is consistent with the presence of two distinct particle sizes as determined from XRD (Fig. 2 - 2: right) and hydrogen release profiles (Fig. 2 - 5(d)). The bimodal character of the nanocomposites in terms of hydrogen mobility was confirmed by the increased line width found in spin-lattice relaxation-weighed spectra (thin black lines in Fig. 2 - 7(a-d)). These relaxation-weighed spectra especially reflect the relatively broad resonances from hydrogen atoms with relatively low mobility. Thus, there was a range of hydrogen mobilities, probably caused by varying MgH_2 domain sizes in the nanocomposites. Although the broad line shape features of a bulk-like MgH_2 phase appeared to be recognizable in the static ^{1}H NMR spectra, the corresponding extremely slow spin-lattice relaxation was not observed for the nanocomposites. Apparently, what looks like "bulk MgH_2" in the ^{1}H NMR line shape and XRD, still differed from macroscopically bulk MgH_2 in terms of ^{1}H NMR relaxation, and probably represent the LNPs. Quantitative comparison of the ^{1}H NMR intensity with an external reference compound (adamantane, 11 wt.% hydrogen) allows the total hydrogen capacity of MgH_2/CA-6, MgH_2/CA-9, MgH_2/CA-12 and MgH_2/CA-20 to be roughly estimated as, 65 %, 38 %, 52 % and 65 % respectively. These values were similar to the values determined from TPD (Table 2 - 2). Following the same procedure for bulk MgH_2 a hydrogen content of 6.9 wt% was obtained, which is close to the theoretical capacity of 7.6 wt% H_2.

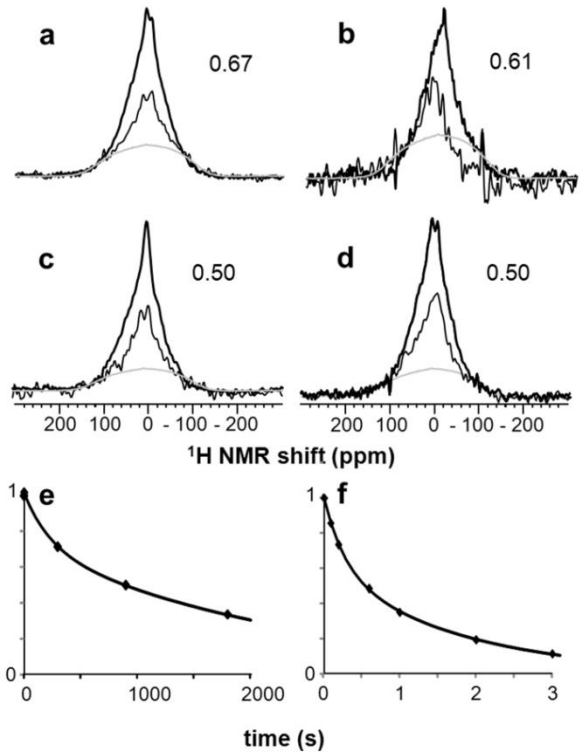

Fig. 2 - 7: Static ^{1}H NMR spectra of the 10 wt% MgH_2 on (a) CA-6, (b) CA-9, (c) CA-12 and (d) CA-20; (e-f) spin-lattice relaxation curves of (e) bulk MgH_2 and (f) 10 wt% MgH_2/CA-20. In addition to the quantitative ^{1}H NMR spectra (thick black lines) figure panels a-d also show the corresponding spin-lattice relaxation weighed spectra (thin, noisy black lines) recorded with a z-filter time of 1 s, as well as the broad resonance line shape of bulk MgH_2 (grey line) for comparison.

Table 2 - 2: Hydrogen release capacities from MgH_2 SNPs on CA and the total amounts of hydrogen released with respect to a loading of 10 wt% MgH_2 on CA. The capacity is determined from the area of the low temperature peak (~280 ^{o}C) in Fig. 2 - 6: left and wide line ^{1}H NMR (Fig. 2 - 7(a-d)). $^\alpha$The deviation might be caused by air contamination during the measurement.

Sample	H_2 capacity SNPs TPD (%)	Total H_2 capacity TPD (%)	Total H_2 capacity NMR (%)
MgH_2/CA-6	14	76	65
MgH_2/CA-9	19	68	38$^\alpha$
MgH_2/CA-12	13	60	52
MgH_2/CA-20	21	54	65

Concluding a clear agreement between the solid state NMR results, showing two MgH_2 fractions with clearly different hydrogen mobility (resulting in about three orders of magnitude difference in hydrogen relaxation times) and the structural and hydrogen release data was observed, which show two MgH_2 fractions, SNPs and LNPs, which are clearly different in size

and hydrogen desorption kinetics. This strongly suggests that the faster hydrogen release for the small MgH_2 nanoparticles can at least partially be attributed to faster hydrogen dynamics in such particles, not only due to decreased solid state diffusion distances, but also due to a higher intrinsic mobility. This is the first time that structural and hydrogen release studies for MgH_2 nanoparticles are combined with intrinsic hydrogen dynamics data.

2.3.3 Hydrogen cycling properties of nano-Mg(H_2) (<20 nm)

The hydrogen cycling properties of the SNPs will now be discussed in more detail. The left frame in Fig. 2 - 8 shows the hydrogen absorption of Mg(H_2)/CA-9 performed at 300 ^oC in 18 bar H_2, for 3 subsequent cycles. An absorption measurement on bulk MgH_2 was added as reference. Bulk MgH_2 only had absorbed 0.25 wt% H_2 after 1 hour, while Mg(H_2)/CA-9 was able to absorb ~1.75 wt% of hydrogen within 1 hour. This is approximately the amount of hydrogen released by the SNPs in MgH_2/CA-9 at low temperatures (Table 2 - 2).

The effect of different absorption times was compared by measuring the hydrogen release profiles in Fig. 2 - 8: middle frame. Interestingly, the same peak at low temperature (~280 ^oC) was clearly present after hydrogenating for 2 hours and almost no hydrogen release was found at higher temperatures. However, after hydrogenating for 10 hours the peak at ~390 ^oC was present again. A small amount of hydrogen was absorbed by the large Mg particles after 2 hours, which is in line with the slow absorption rate of the Mg reference with a powder size in the range micrometers (Fig. 2 - 8: left). These results clearly show that not only the hydrogen desorption, but also the hydrogen absorption kinetics are strongly affected by the particle size. The large difference in hydrogen sorption rates allows for a selective study on the cycling behavior of the SNPs.

Subsequent absorption cycles were performed on MgH_2/CA-9 (Fig. 2 - 8: left). Within 15 min, the first cycle absorbed ~ 1.3 wt%, while the other cycles have reached a higher capacity after the same time (~ 1.5 wt%). Possibly, the Mg phase became more accessible for hydrogen molecules to enter the crystal lattice after the first cycle. This result is comparable to MgH_2/CA nanocomposites prepared by solution impregnation [36] and shows that these Mg(H_2) nanoparticles have an excellent cycling stability with its improved kinetics maintained.

After performing 4 absorption and desorption cycles, hydrogen release for all MgH_2/CA composites was measured again to compare between the performance of the first cycle and after

4 cycles. The right frame in Fig. 2 - 8 shows the desorption profiles and interestingly, the peaks at low temperatures were still present with similar peak temperatures. Almost no capacity loss was observed, which indicate that no side reactions took place; and no loss in kinetic performance occurred. Thus, the $Mg(H_2)$ nanoparticles showed excellent cycling stability over 4 cycles.

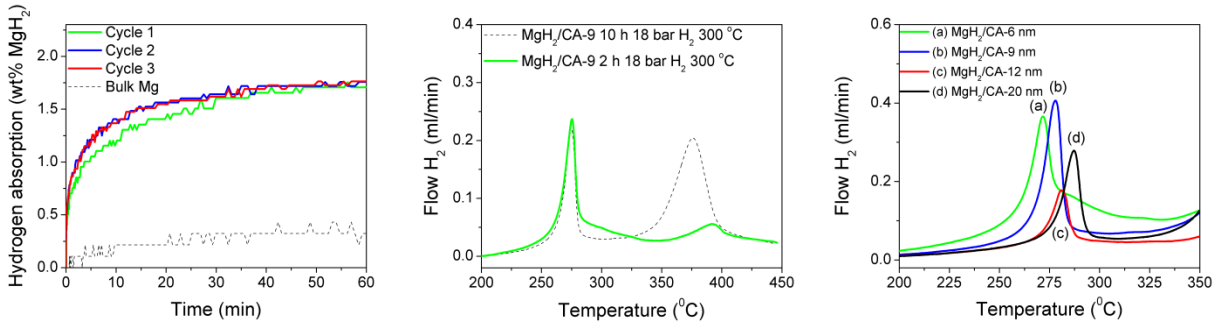

Fig. 2 - 8: Left: Absorption kinetics of 10 wt% Mg/CA-9 measured volumetrically at 300 °C and 18 bar H_2. Three absorption-desorption cycles were measured subsequently. The absorption of MgH_2 powder (± 37 µm) is shown as reference. Middle: Hydrogen release profiles of 10 wt% MgH_2/CA-9 after different first H_2 absorption durations of 2 h and 10 h. Right: Hydrogen release from 10 wt% nano-MgH_2 on (a) CA-6, (b) CA-9, (c) CA-12 and (d) CA-20 after 4 hydrogen sorption cycles at 300 °C. Absorption and desorption was performed at 18 bar and 0.3 bar H_2, respectively.

2.4. Conclusion

Carbon aerogels with different pore size distributions were synthesized and MgH_2 nanoparticles were deposited by heating a mixture of MgH_2 with the carbon aerogels. A bimodal distribution of MgH_2 particles was obtained on the different CAs, which could be distinguished as small nano-MgH_2 particles (< 20 nm) and larger particles. The small nanoparticles had a size between 3 to 20 nm and the size was correlated to the pore size of the carbon support. Hydrogen sorption measurements showed a large difference in the hydrogen sorption rates for the two different particle size regimes. The peak temperature for hydrogen desorption of the MgH_2/CA composites varied around 280 °C depending on the pore size of the CA, while temperatures near 400 °C were observed for the larger nanoparticles. Within the small nanoparticle population, the larger the particle, the higher the hydrogen desorption temperatures. Also, the ^1H wideline NMR spectra clearly showed that the hydrogen dynamics depended on the particle size of MgH_2 with 3 orders of magnitude faster hydrogen dynamics for the small nanoparticles.

Hydrogen storage in the small MgH_2 nanoparticles was completely reversible for at least 4 cycles. A capacity of ~80% was absorbed within 15 min for the Mg nanoparticles at 300 ^oC with 18 bar H_2. This study shows for the first time a clear relation between MgH_2 particle size and hydrogen desorption rates, combined with hydrogen mobility data for the different MgH_2 sizes.

Acknowledgements

M. van Zwienen and J. D. Meeldijk are acknowledged for their technical support in the hydrogen sorption measurement; and for obtaining the TEM images.

References

(1) International Energy Agency Monthly Electricity Statistics. *http://www.iea.org/newsroomandevents/newsletters/* (accessed 03/28, 2013).

(2) Crabtree, G. W.; Dresselhaus, M. S.; Buchanan, M. V. The Hydrogen Economy. *Phys Today* **2004**, *57*, 39-44.

(3) Larsson, P.; Araújo, C. M.; Larsson, J. A.; Jena, P.; Ahuja, R. Role of Catalysts in Dehydrogenation of MgH_2 Nanoclusters. *Proc. Natl. Acad. Sci. U. S. A.* **2008**, *105*, 8227-8231.

(4) Mao, G.; Hu, X.; Wu, X.; Dai, Y.; Chu, S.; Deng, J. Benchmark Quantum Monte Carlo Calculation of the Enthalpy of Formation of MgH_2. *Int J Hydrogen Energy* **2011**, *36*, 8388-8391.

(5) Felderhoff, M.; Bogdanović, B. High Temperature Metal Hydrides as Heat Storage Materials for Solar and Related Applications. *International Journal of Molecular Sciences* **2009**, *10*, 335-344.

(6) McPhy Energy, Solid hydrogen storage. *http://www.mcphy.com/en/technologies/solid-hydrogen-storage/* (accessed 11-2012, 2012).

(7) Zhang, Q. A.; Wu, H. Y. Hydriding Behavior of $Mg_{17}Al_{12}$ Compound. *Mater. Chem. Phys.* **2005**, *94*, 69-72.

(8) Haussermann, U.; Blomqvist, H.; Noréus, D. Bonding and Stability of the Hydrogen Storage Material Mg_2NiH_4. *Inorg. Chem.* **2002**, *41*, 3684-3692.

(9) Wu, Z.; Allendorf, M. D.; Grossman, J. C. Quantum Monte Carlo Simulation of Nanoscale MgH_2 Cluster Thermodynamics. *J. Am. Chem. Soc.* **2009**, *131*, 13918-13919.

(10) Vajeeston, P.; Ravindran, P.; Fichtner, M.; Fjellvåg, H. Influence of Crystal Structure of Bulk Phase on the Stability of Nanoscale Phases: Investigation on MgH_2 Derived Nanostructures. *Journal of Physical Chemistry C* **2012**, *116*, 18965-18972.

(11) Wagemans, R. W. P.; Van Lenthe, J. H.; De Jongh, P. E.; Van Dillen, A. J.; De Jong, K. P. Hydrogen Storage in Magnesium Clusters: Quantum Chemical Study. *J. Am. Chem. Soc.* **2005**, *127*, 16675-16680.

(12) Paskevicius, M.; Sheppard, D. A.; Buckley, C. E. Thermodynamic Changes in Mechanochemically Synthesized Magnesium Hydride Nanoparticles. *J. Am. Chem. Soc.* **2010**, *132*, 5077-5083.

(13) Bérubé, V.; Radtke, G.; Dresselhaus, M.; Chen, G. Size Effects on the Hydrogen Storage Properties of Nanostructured Metal Hydrides: A Review. *Int. J. Energy Res.* **2007**, *31*, 637-663.

(14) Berlouis, L. E. A.; Honnor, P.; Hall, P. J.; Morris, S.; Dodd, S. B. An Investigation of the Effect of Ti, Pd and Zr on the Dehydriding Kinetics of MgH_2. *J. Mater. Sci.* **2006**, *41*, 6403-6408.

(15) Chen, D.; Chen, L.; Wang, Y.; Liu, S.; Chen, D.; Ma, C.; Wang, L. Ca, Pd, Sn and La Effects on the Electronic Structure of MgH_2. *Xiyou Jinshu Cailiao Yu Gongcheng/Rare Metal Materials and Engineering* **2004**, *33*, 485-489.

(16) Gutfleisch, O.; Dal Toè, S.; Herrich, M.; Handstein, A.; Pratt, A. Hydrogen Sorption Properties of Mg-1 Wt.% Ni-0.2 Wt.% Pd Prepared by Reactive Milling. *J. Alloys Compounds* **2005**, *404-406*, 413-416.

(17) Hanada, N.; Ichikawa, T.; Fujii, H. Catalytic Effect of Ni Nano-Particle and Nb Oxide on H-Desorption Properties in MgH2 Prepared by Ball Milling. *J. Alloys Compounds* **2005**, *404-406*, 716-719.

(18) Jensen, T. R.; Andreasen, A.; Vegge, T.; Andreasen, J. W.; Ståhl, K.; Pedersen, A. S.; Nielsen, M. M.; Molenbroek, A. M.; Flemming Besenbacher Dehydrogenation Kinetics of Pure and Nickel-Doped Magnesium Hydride Investigated by in Situ Time-Resolved Powder X-Ray Diffraction. *Int J Hydrogen Energy* **2006**, *31*, 2052-2062.

(19) Oelerich, W.; Klassen, T.; Bormann, R. Metal Oxides as Catalysts for Improved Hydrogen Sorption in Nanocrystalline Mg-Based Materials. *J. Alloys Compounds* **2001**, *315*, 237-242.

(20) Notten, P. H. L.; Ouwerkerk, M.; Van Hal, H.; Beelen, D.; Keur, W.; Zhou, J.; Feil, H. High Energy Density Strategies: From Hydride-Forming Materials Research to Battery Integration. *J. Power Sources* **2004**, *129*, 45-54.

(21) Beattie, S. D.; Setthanan, U.; McGrady, G. S. Thermal Desorption of Hydrogen from Magnesium Hydride (MgH_2): An in Situ Microscopy Study by Environmental SEM and TEM. *Int J Hydrogen Energy* **2011**, *36*, 6014-6021.

(22) Ngene, P.; Van Zwienen, R.; De Jongh, P. E. Reversibility of the Hydrogen Desorption from $LiBH_4$: A Synergetic Effect of Nanoconfinement and Ni Addition. *Chemical Communications* **2010**, *46*, 8201-8203.

(23) Adelhelm, P.; Gao, J.; Verkuijlen, M. H. W.; Rongeat, C.; Herrich, M.; Van Bentum, P. J. M.; Gutfleisch, O.; Kentgens, A. P. M.; De Jong, K. P.; De Jongh, P. E. Comprehensive Study of Melt Infiltration for the Synthesis of $NaAlH_4$/C Nanocomposites. *Chemistry of Materials* **2010**, *22*, 2233-2238.

(24) Gao, J.; Adelhelm, P.; Verkuijlen, M. H. W.; Rongeat, C.; Herrich, M.; Van Bentum, P. J. M.; Gutfleisch, O.; Kentgens, A. P. M.; De Jong, K. P.; De Jongh, P. E. Confinement of $NaAlH_4$ in Nanoporous Carbon: Impact on H_2 Release, Reversibility, and Thermodynamics. *Journal of Physical Chemistry C* **2010**, *114*, 4675-4682.

(25) De Jongh, P. E.; Adelhelm, P. Nanosizing and Nanoconfinement: New Strategies Towards Meeting Hydrogen Storage Goals. *ChemSusChem* **2010**, *3*, 1332-1348.

(26) Pekala, R. W. Organic Aerogels from the Polycondensation of Resorcinol with Formaldehyde. *J. Mater. Sci.* **1989**, *24*, 3221-3227.

(27) Li, W. C.; Lu, A. H.; Weidenthaler, C.; Schüth, F. Hard-Templating Pathway to Create Mesoporous Magnesium Oxide. *Chemistry of Materials* **2004**, *16*, 5676-5681.

(28) Hunter, B. A. *IUCR Powder Diffraction* **1997**, *22*, 21.

(29) Verkuijlen, M. H. W.; Ngene, P.; De Kort, D. W.; Barré, C.; Nale, A.; Van Eck, E. R. H.; Van Bentum, P. J. M.; De Jongh, P. E.; Kentgens, A. P. M. Nanoconfined $LiBH_4$ and Enhanced Mobility of $[Li]^+$ and $[BH]^{4-}$ Studied by Solid-State NMR. *Journal of Physical Chemistry C* **2012**, *116*, 22169-22178.

(30) De Jongh, P. E.; Wagemans, R. W. P.; Eggenhuisen, T. M.; Dauvillier, B. S.; Radstake, P. B.; Meeldijk, J. D.; Geus, J. W.; De Jong, K. P. The Preparation of Carbon-Supported Magnesium Nanoparticles using Melt Infiltration. *Chemistry of Materials* **2007**, *19*, 6052-6057.

(31) Zlotea, C.; Chevalier-César, C.; Léonel, E.; Leroy, E.; Cuevas, F.; Dibandjo, P.; Vix-Guterl, C.; Martens, T.; Latroche, M. Synthesis of Small Metallic Mg-Based Nanoparticles Confined in Porous Carbon Materials for Hydrogen Sorption. *Faraday Discuss.* **2011**, *151*, 117-131.

(32) Konarova, M.; Tanksale, A.; Norberto Beltramini, J.; Qing Lu, G. Effects of Nano-Confinement on the Hydrogen Desorption Properties of MgH_2. *Nano Energy* **2013**, *2*, 98-104.

(33) Nielsen, T. K.; Manickam, K.; Hirscher, M.; Besenbacher, F.; Jensen, T. R. Confinement of MgH_2 Nanoclusters within Nanoporous Aerogel Scaffold Materials. *ACS Nano* **2009**, *3*, 3521-3528.

(34) Paskevicius, M.; Tian, H.; Sheppard, D. A.; Webb, C. J.; Pitt, M. P.; Gray, E. M.; Kirby, N. M.; Buckley, C. E. Magnesium Hydride Formation within Carbon Aerogel. *Journal of Physical Chemistry C* **2011**, *115*, 1757-1766.

(35) Srinivasan, S.; Magusin, P. C. M. M.; Van Santen, R. A.; Notten, P. H. L.; Schreuders, H.; Dam, B. Siting and Mobility of Deuterium Absorbed in Cosputtered $Mg_{0.65}Ti_{0.35}$. A MAS ^2H NMR Study. *Journal of Physical Chemistry C* **2011**, *115*, 288-297.

(36) Liu, Y.; Zou, J.; Zeng, X.; Wu, X.; Tian, H.; Ding, W.; Wang, J.; Walter, A. Study on Hydrogen Storage Properties of Mg Nanoparticles Confined in Carbon Aerogels. *Int J Hydrogen Energy* **2013**, *38*, 5302-5308.

3. Synthesis of Mg_2Cu nanoparticles on carbon supports with enhanced hydrogen sorption kinetics

Abstract

The reaction kinetics and reversibility for hydrogen sorption were investigated for supported Mg_2Cu nanoparticles on carbon. A new preparation method is proposed to synthesize the supported alloy nanoparticles. The motivation of using a support is to separate the nanoparticles to prevent sintering at elevated temperatures. Supported nanocrystallites with an average size of 20 nm were obtained on porous graphite and larger particles (~300 nm) on non-porous graphite by first deposition of metallic Cu species, using solution impregnation, followed by addition of molten Mg and hydrogenation. The temperature for hydrogen release of the 20 nm particles was much lower (~150 ^{o}C) than the micron-sized material, and the reaction was reversible with the same improved kinetic performance after several hydrogen sorption cycles. The 20 nm Mg_2Cu crystallites had a lower activation energy for the hydrogen desorption reaction compared to the bulk material (97 (± 9) and 128 (± 6) kJ·mol^{-1} respectively). A desorption enthalpy of 66 (± 3) kJ·mol^{-1} and an entropy value of 126 (± 10) J·mol^{-1}·K^{-1} were found for this system. The use of a porous carbon support was beneficial for obtaining Mg_2Cu nanoparticles, which improved the hydrogen sorption kinetics.

3.1 Introduction

The decrease in the fossil fuel reserves has led to an increasing interest to produce energy from renewable sources. Hydrogen is a promising candidate to act as a sustainable energy carrier in the future. But to allow usage of hydrogen as energy carrier, an efficient and safe way for storage is required. Hydrogen storage in a solid could be a solution.

Magnesium is a promising material for hydrogen storage and has been widely studied because of its light weight and natural abundance. It can store hydrogen directly, forming MgH_2, which contains 7.7 wt% of hydrogen. However, it suffers from slow hydrogen sorption kinetics and has a high thermodynamic stability, since the equilibrium temperature for the hydrogen sorption reaction is around 300 ^oC for 1 bar of H_2 pressure. Many investigations have been conducted on Mg as potential hydrogen storage material to improve the reaction kinetics and to change the thermodynamic stability in order to shift the reaction equilibrium to ambient conditions [1, 2].

One way to improve the kinetics of the hydrogen sorption reaction is to add a catalyst. Doping small amounts of other metals such as Ti, V, Mn, Fe and Ni has led to enhanced hydrogen sorption kinetics and lowered the activation energy for hydrogen desorption of MgH_2 [3]. Also, the addition of small amounts of metal oxides like Nb_2O_5 resulted in improved kinetic performance [4]. Another method to alter the hydrogen storage properties of Mg is to form intermetallics. For example, Mg-Ni or Mg-Al form stable intermetallics [5, 6]. Some of these intermetallic compositions can form ternary hydrides upon hydrogenation like the well known Mg_2NiH_4. Moser et al. were able to synthesize ternary hydrides with Ti, Zr, Hf, V Nb and Ta [7]. The enthalpy of formation for these ternary hydrides is usually less negative than pure MgH_2, so that hydrogen can be released at lower temperatures for these systems.

Another way to improve hydrogen sorption properties is by nanosizing the material. In general, reducing the particle or crystallite size improves the access for H_2 to enter the lattice by the increased surface area to volume ratio. Also, the diffusion distance for hydrogen molecules through the crystal lattice is decreased. Mechanical alloying, arc-discharge and colloid synthesis have been used to prepare nanostructured Mg based intermetallics and altered kinetic behavior for hydrogen sorption was reported [8-14]. An important issue is sintering of the nanostructures at high temperatures, which will diminish the benefits obtained [15]. The formation of large particles is energetically favorable due to their lower specific surface area compared to small particles. A

microscopy study by Beattie et al. has shown that small Mg particles formed an agglomerated network after heating to 400 ^{o}C [16].

To prevent sintering, one can disperse the metal particles over a support material. The support material should be inert to prevent a reaction between the support and the deposited metal species. Most hydrogen storage materials are susceptible to oxidation and form stable oxides, which is an irreversible reaction. Mg is no exception, thus any material containing oxygen species is not suitable. This narrows the choice down to carbon support materials. Carbon is inert towards most metal compositions and depending on the morphology of the carbon material, particle sizes can be controlled during the synthesis process. Quite a number of hydrogen storage systems supported or embedded in carbon have already been studied [17-19]. Nanosized Mg-Ni composites by using a carbon support were synthesized earlier [20]. A mixture of nanostructured Mg_2NiH_4 and Ni catalyzed nano-MgH_2 particles were obtained and improved hydrogen desorption properties were observed.

The aim of the work described was to modify the hydrogen sorption properties of MgH_2 by investigating the possibility to synthesize supported Mg_2Cu nanoparticles on carbon. Next to the challenge to obtain a pure phase of supported alloy nanoparticles, this model system could also demonstrate the synergetic effect of supported nanoparticles and addition of a transition metal to change the thermodynamic equilibrium. So far, no ternary hydride of the Mg-Cu system has been reported in the literature. The role of Cu is to substitute H_2 in MgH_2 to from the stable Mg_2Cu compound, leading to a lower desorption enthalpy compared to pure MgH_2. Reilly and Wiswall were one of the first to investigate the hydrogen sorption properties of the bulk Mg_2Cu intermetallic system [21]. They found that this system can reversibly store up to 2.6 wt% of hydrogen following the reaction:

$$2\ Mg_2Cu + 3\ H_2 \leftrightarrow 3\ MgH_2 + MgCu_2 \qquad \text{(Eq. 3 - 1)}$$

They also reported that the enthalpy for the hydrogen desorption reaction is approximately 5.9 $kJ \cdot mol^{-1}$ lower compared to the pure MgH_2 system. Next to diffusion of hydrogen through the material as in pure MgH_2, this reaction also requires solid state diffusion of Mg to go from the Mg-poor to the Mg-rich state of the alloy and vice versa. Solid-state diffusion is slow and requires thermal activation. Nanosizing this intermetallic system could improve the reaction kinetics by shortening the diffusion distance of the Mg atoms to perform reaction (Eq. 3 - 1).

Bulk Mg_2Cu can be crystallized from a melt with the correct stoichiometric Mg : Cu ratio as described by the phase diagram of the Mg-Cu system in Fig. 3 - 1 [22]. However, it is not trivial to prepare nanoparticles from a melt due to the high vapor pressure of Mg and possible demixing of the alloy phase. An alternative synthesis strategy is to use a support material to obtain small and well dispersed alloy particles. In this way the particles are prevented from sintering at elevated temperatures. A method to deposit small metallic Cu particles on a support material is to use solution impregnation techniques, which are widely applied in catalyst preparation [23, 24].

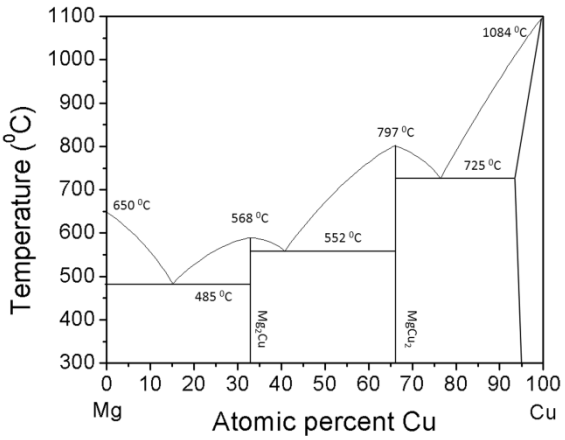

Fig. 3 - 1: Phase diagram of the Mg-Cu system.

The addition of Mg is not as straightforward as Cu. Mg easily reacts irreversibly with other species, such as oxygen, to form stable compounds, thereby greatly limiting the choice for suitable precursors to perform a second impregnation or co-impregnation with a suitable solvent. On the other hand, another method was developed to disperse Mg nanoparticles over carbon with a melting process [25]. Therefore, Mg_2Cu was synthesized in two steps by first depositing small Cu particles on the support followed by a melting process, where molten Mg reacts with the supported Cu particles. The characteristics of the obtained intermetallic compositions on two different carbon supports are shown. Different particle sizes were obtained and they showed different kinetic behavior for hydrogen desorption.

3.2 Experimental

3.2.1 Sample preparation

The first step in preparing Mg_2Cu on carbon was to perform incipient-wetness impregnation to deposit small Cu particles on the carbon support. An aqueous solution of 2.5 M $Cu(NO_3)_2.3H_2O$ (Sigma-Aldrich) was used. The solution was acidified to a pH of 1 with nitric acid to prevent the precipitation of basic nitrates during the impregnation procedure. Two different carbon supports were used. One was a porous carbon material (Timcal High Surface Area Graphite (HSAG)) with a surface area of 500 $m^2 \cdot g^{-1}$ and with a total pore volume of 0.66 $cm^3 \cdot g^{-1}$. The other was a non-porous graphite material (Timcal KS-6) with a surface area of 21 $m^2 \cdot g^{-1}$. The carbons were degassed at 600 ^oC overnight in an Ar atmosphere to remove all traces of moisture.

The dry carbons (1 g) were impregnated with 0.66 ml of the $Cu(NO_3)_2$ solution under an Ar atmosphere, followed by drying in vacuum at room temperature overnight. For decomposition of the precursor and reduction to obtain metallic Cu particles, the sample was heated to 230 ^oC with a temperature ramp of 1 $^oC \cdot min^{-1}$ and a dwell time of 30 min under a 20% H_2 in Ar gasflow of 300 $ml \cdot min^{-1}$. All further sample handling for the next synthesis steps was performed in an Ar-glove box (MBraun Labmaster) and excluded from contact with air.

The next step was to perform the melting of Mg with the presence of the Cu-C materials following a procedure as described in the literature [25]. MgH_2 (Alfa Aesar 98%) was used as precursor. The Cu-C composite (1.0 g) was mixed with MgH_2 (85 mg) and ground in a mortar. The molar ratio of Mg : Cu was 2.25 : 1, which is slightly higher than the stoichiometric amount in Mg_2Cu. An excess of Mg was used to avoid the formation of $MgCu_2$ [22]. The final composites consist of 15 wt% Mg_2Cu on carbon. A reference sample containing 10 wt% MgH_2 on porous carbon (Timcal High Surface Area Graphite) was prepared with the same procedure. Hydrogenation of the samples was performed in high pressure autoclaves (Parr) at 300 ^oC and H_2 pressures around 80 bars for 12 hours. The hydrogenated samples are designated as $Mg_2Cu(H)$.

Bulk Mg_2Cu was synthesized by induction melting. A Cu-plate (Chempur 99,99%) was wrapped around a Mg-rod (Chempur 99,9%) and placed in a Ta-foil crucible. The exact molar ratio of 2 : 1 was used for Mg and Cu respectively. The sample was placed in a sealed quartz tube and brought into the coil of the induction furnace. The quartz tube with the sample was evacuated and refilled with Ar before the current of the induction furnace was slowly increased

until a molten mixture was observed. The molten metal mixture was kept under the same current for 30 min followed by cooling to room temperature. After the reaction was completed, the alloy was heated under Ar in a tubular resistance furnace at 470 ^{o}C for 1 day to ensure chemical homogeneity. Lastly, the sample was powdered in a mortar and sieved to obtain particles smaller than 10 microns. This sample was used for reference purposes either in bare state or physically mixed (15 wt%) with porous carbon.

3.2.2 Structural characterization

The crystalline phases in the samples were analyzed with X-ray diffraction (XRD) (Bruker D8 equipped with VANTEC-1 detector and using Co K$\alpha_{1,2}$ radiation in an airtight sample holder). Data was collected from 20^{o} to 105^{o} 2θ with a step size of 0.1^{o} with an acquisition time of 2 s per step. The data was refined by using the Rietica program [26].

N_2-physisorption (Micromeritics TriStar 3000) was performed at 77 K for porosity analysis. Barrett-Joyner-Halenda (BJH) analysis on the adsorption isotherms, using a carbon black as reference for the thickness equation, provided information on the pore-size distribution of the meso-pores. The total pore volume was obtained at p/p_0 = 0.997. Leaching of the Mg-Cu from the nanocomposite was done in a diluted nitric acid solution (*pH* ~ 2.5) and stirred overnight followed by filtration and washing with demineralized water until the *pH* was neutral. This sample was dried under He at 200 ^{o}C before measurement. The other samples were prepared in a capped quartz sample tube in the glovebox and were directly measured.

A Scanning Electron Microscope (SEM) (Philips XL30S FEG equipped with embedded Energy-dispersive X-ray spectroscopy (EDX) and low kilovolt backscatter detectors) was used to obtain micrographs from back-scattered electrons (BSE). The samples were prepared in air by spreading a thin powder layer on sticky carbon. For Transmission Electron Microscopy (TEM), a part of the sample was stored in air and a small amount of sample was put on a 200 mesh Ni grid coated with a carbon polymer film. The microscope images were taken with an FEI Tecnai 20F (equipped with a Field Emission Gun) and operated at 200 kV in bright field mode.

3.2.3 Hydrogen sorption measurements

Temperature Programmed Desorption (TPD) (Micromeritics AutoChem II 2920) measurements were performed to obtain kinetic data on hydrogen release. Approximately 100

mg of sample was taken for each measurement. The experiments were carried out in an Ar-flow of 25 $ml \cdot min^{-1}$ with a temperature ramp of 5 $^oC \cdot min^{-1}$ and dwelled at 450 ^oC for 20 min. To allow Kissinger analysis, the temperature ramps were varied from 1 $^oC \cdot min^{-1}$, 2 $^oC \cdot min^{-1}$, 5$^oC \cdot min^{-1}$ to 10 $^oC \cdot min^{-1}$.

Cycling performance of the material was tested gravimetrically after activation with a magnetic suspension balance (Rubotherm). Desorption was measured under 1.3 bars of H_2 with a temperature ramp of 1 $^oC \cdot min^{-1}$ up to 380 ^oC and absorption at 300 ^oC under 50 bars of H_2 for 5 hours. Activation of the material was performed *ex-situ* in an autoclave. Absorption occurred at 325 ^oC and 50 bar H_2 pressure for 10 h and desorption was performed in vacuum for 2 h at the same temperature.

H_2 desorption isotherms were also measured volumetrically by using Sieverts' method (Setaram PCT PRO-2000). The sample was placed in a steel holder, which was covered with graphite foil (PAPYEX®) on the inside to prevent side reactions at temperatures above 350 ^oC. The hydrogen desorption measurements were performed at 250 ^oC, 300 ^oC, 325 ^oC and 350 ^oC with pressure steps of 2 bar H_2. Two boundary conditions were set for obtaining an equilibrium: a minimum kinetic rate of 1.10^{-4} $wt\%(H_2) \cdot min^{-1}$ and a time limit of 150 min. Rehydrogenation was performed *in-situ* at 300 ^oC and 50 bars of H_2 for 12 hours.

3.3 Results and discussion

3.3.1 Structural characterization of the Cu-C composites

The X-ray diffraction patterns show only C and Cu diffraction lines for both the porous (Fig. 3 – 2(a) : left) and non-porous carbon supports (Fig. 3 - 2(a): right) after Cu impregnation and reduction. Profile fitting with Rietveld refinement confirms that only metallic Cu (F*m*-3*m*) on graphitic carbon ($P6_3/mmc$) was present as crystalline phase. The average crystallite size of Cu on porous carbon was 10 nm, which was calculated from the line width at half maximum of all the Cu diffraction lines. A larger average crystallite size of 30 nm for Cu on non-porous carbon was calculated from its diffraction pattern.

SEM with backscattered electrons shows the difference between the Cu particle sizes obtained on the porous and non-porous support (Fig. 3 - 3(a) and (b)). The obtained Cu particles were much smaller on porous carbon and the distribution of the particles was quite homogeneous over the porous carbon support. This probably prevented the growth of the Cu particles during the

reduction step. So, using High Surface Area Graphite was better for obtaining small Cu particles with a uniform distribution.

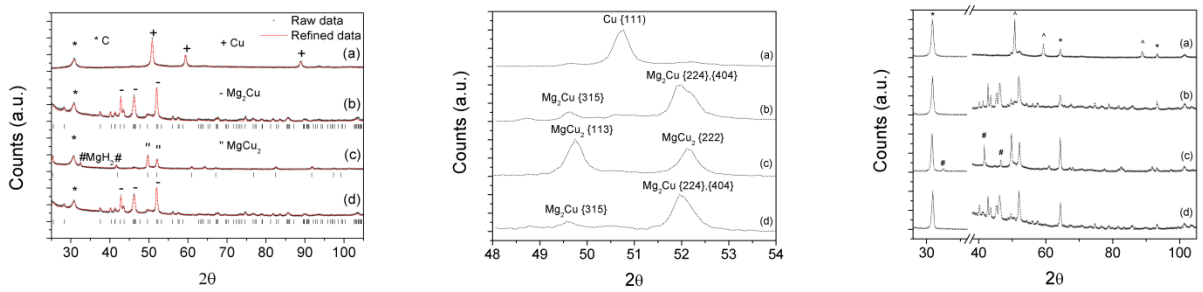

Fig. 3 - 2: XRD patterns obtained after Cu impregnation on porous carbon (a), Mg addition (b), hydrogenation (c) and dehydrogenation (d). A selected region is enlarged for clarity (middle frame). The strongest lines belonging to C(*), Cu(+), MgH_2(#), Mg_2Cu (-) and $MgCu_2$(″) are indicated. (|) Underneath the patterns represents the position of all the reflections for Mg_2Cu (b,d) and $MgCu_2$ (c). Right: XRD patterns of the samples supported on KS-6 after impregnation (a), Mg addition (b), hydrogenation (c) and dehydrogenation (d). The region after 40° is normalized at a different scale for clarity. The following phases are indicated: C (*), Cu (^) and MgH_2(#). The other reflections belong either to Mg_2Cu (b, d) or $MgCu_2$ (c).

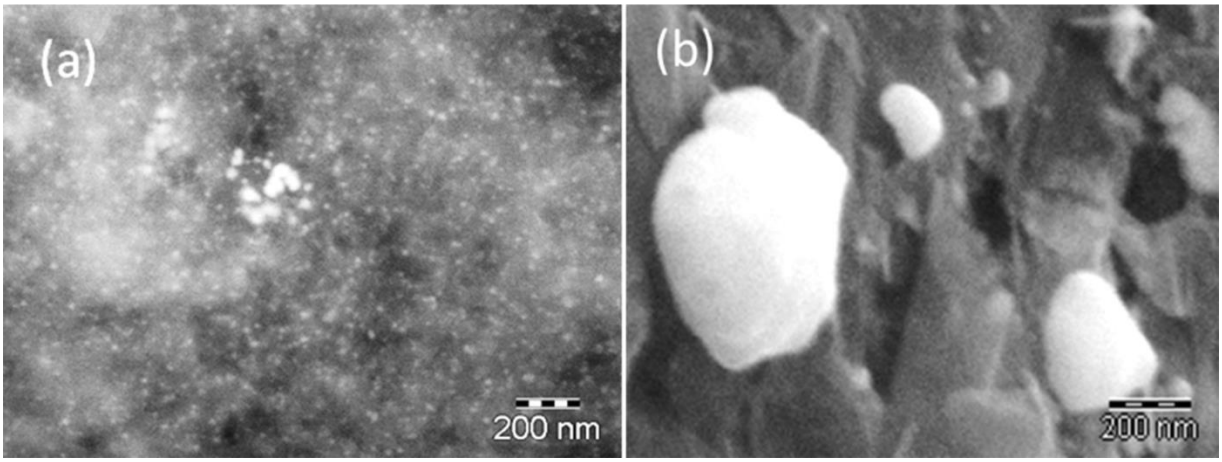

Fig. 3 - 3: SEM-images from back-scattered electrons of: (a) Cu on porous carbon (b) Cu on non-porous carbon.

Fig. 3 - 4 shows the obtained N_2-physisorption isotherms and the derived pore size distribution of the porous carbon support. The shape of the nitrogen sorption isotherm (Fig. 3 - 4(a and b)) did not change after the deposition of Cu, so the structure of the pores did not change; however, a gradual decrease of the porosity was observed. The decrease in pore volume is observed mainly in the 2-20 nm region (Table 3 - 1). This suggests that some Cu particles might occupy these pores. However, the pore volume loss is larger than expected. To verify whether the pore

structure was changed, the metals were leached from the carbon in an acidic solution and the sample was re-measured (Fig. 3 - 4(d)). The total pore volume was recovered after this treatment, so no severe damage to the carbon structure has occurred. The extra loss in pore volume might be caused by blockage of the pores by the Cu particles. Clearly, these observations again stress that porous carbon is better for obtaining small Cu particles compared to non-porous carbon, because porous carbon was able to prevent agglomeration of the Cu particles during the drying and reduction step by providing a larger surface area and partial entrapment of the Cu particles inside its pores.

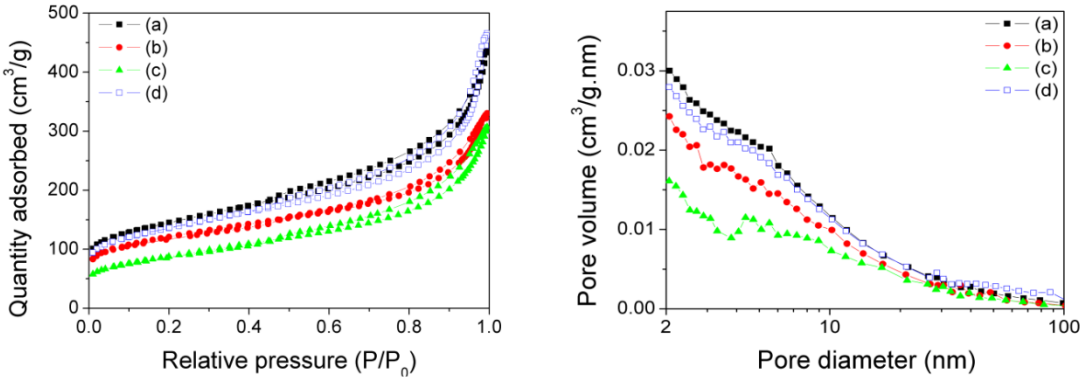

Fig. 3 - 4: Nitrogen isotherms (left) and pore size distribution (right) of: (a) HSAG-500, (b) after Cu impregnation, (c) after addition of Mg and (d) after removal of all metal species.

3.3.2 Structural characterization of the Mg_2Cu-C composites

XRD was performed again after the reaction with Mg to analyze new crystalline phases. The diffraction pattern (Fig. 3 - 2(b): left) fitted well with the structure models of Mg_2Cu (F*ddd*) and graphitic carbon ($P6_3/mmc$) using Rietveld refinement [27]. Calculation from the line width of the 5 strongest diffraction lines of the Mg_2Cu phase yielded average Mg_2Cu crystallites of 20 nm on the porous carbon material, while much larger Mg_2Cu crystallites were present on non-porous carbon graphite. The excess of Mg successfully prevented the formation of $MgCu_2$, but no additional Mg diffraction lines were observed. The absence of these diffraction lines could be due to evaporation of Mg, which has a high vapor pressure, during the melting reaction. Alternatively, very small Mg particles might have formed within the carbon pores, which could not be detected by XRD.

The electron microscope images of different Mg_2Cu composites are shown in Fig. 3 - 5. The TEM image in Fig. 3 - 5(a) visualizes Mg_2Cu on porous carbon. The dark spheres represent the Mg_2Cu alloy and carbon is observed as a plate like structure in grey. The size of the dark spheres varies from 10 nm to 50 nm, but most particles had a size close to 25 nm. Larger Mg_2Cu particles were observed in the SEM-image for the sample prepared on non-porous carbon Fig. 3 - 5(b). The image from back-scattered electrons shows the spherical alloy particles in white. The graphite plates are visible in dark grey. The particles varied in size between 100 nm to 500 nm. The majority of the particles was 300 nm in size. The SEM image of the sieved fraction of bulk Mg_2Cu, which was physically mixed with porous carbon is shown in Fig. 3 - 5(c). Most crystals have a size up to a few micrometers. The histogram of the particle size distribution of Mg_2Cu on porous and non-porous carbon is shown in Fig. 3 - 5(d). In summary, samples with a different size range were obtained.

N_2-physisorption of Mg_2Cu on porous carbon (Fig. 3 - 4(c)) shows a further decrease in pore volume compared to Cu on porous carbon, which was approximately the expected loss due to addition of Mg (Table 3 - 1). BJH analysis of the pore size distribution shows a gradual decrease of the pore volume in the region between 2-20 nm and follows the same trend as the previous measurement on the Cu-C composite (Fig. 3 - 4(b)). Therefore, Mg successfully reacted with the small Cu particles to form nanosized alloy particles. On the contrary, large alloy crystals were formed on non-porous carbon due to agglomeration during the reaction. The crystal growth on porous carbon was surprisingly limited.

Table 3 - 1: Calculated values for the Brunauer-Emmet-Teller (BET) surface area (S_{BET}), meso-pore volume ($V_{2\text{-}50nm}$), single point total pore volume (V_{total}) and expected total pore volume loss (V_{ex}) of HSAG-500 assuming all metals are inside the pores.

Sample	S_{BET} ($m^2 \cdot g^{-1}$)	$V_{2\text{-}20\ nm}$ ($cm^3 \cdot g^{-1}$)	V_{total} ($cm^3 \cdot g^{-1}$)	V_{ex} ($cm^3 \cdot g^{-1}$)
(a) HSAG-500	499	0.24	0.66	-
(b) Cu-C	467	0.19	0.56	0.02
(c) Mg_2Cu-C	291	0.14	0.51	0.05
(d) C leached	470	0.23	0.71	-

The XRD pattern in Fig. 3 - 2(c): left shows the obtained crystalline phases after hydrogenation. New peaks have appeared, which corresponds to crystalline MgH_2 ($P4_2/mnm$)

and $MgCu_2$ (F*d*3*m*) [28]. The peaks around 50° and 52° show the transformation of the Mg_2Cu to the $MgCu_2$ lattice and two new strong diffraction lines around 32° and 42° are from the MgH_2 phase. XRD after dehydrogenation yielded the pattern in Fig. 3 - 2(d): left, which is identical to the pattern obtained after synthesis of the alloy (Fig. 3 - 2(b): left). Similar results were observed for the samples synthesized on non-porous carbon, where the observed diffraction lines were sharper compared to the samples on porous carbon (Fig. 3 - 2(b-d): right). Both systems show full reversibility after hydrogenation and dehydrogenation.

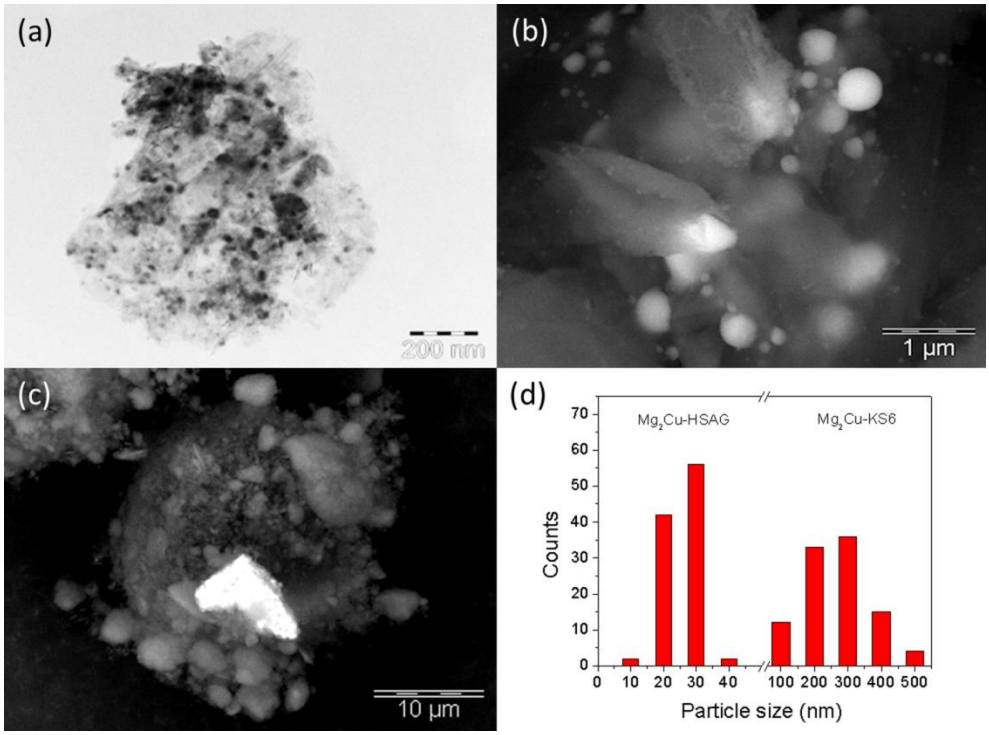

Fig. 3 - 5: Overview of electron microscope images. (a) is a bright field TEM image of Mg_2Cu on porous carbon. (b) is a SEM image of Mg_2Cu on non-porous carbon from BSE. (c) is a SEM image from BSE of a physical mixture of powdered Mg_2Cu particles prepared by induction melting with porous carbon. In frame (d) the particle size distribution of Mg_2Cu on porous and non-porous carbon is shown as determined by the electron microscope images.

3.3.3 Hydrogen release properties

Fig. 3 - 6 shows the hydrogen release profiles of both $Mg_2Cu(H)$ prepared on porous carbon (a) and $Mg_2Cu(H)$ synthesized on non-porous carbon (b). As reference materials the following samples are also included: a sample containing a physical mixture of bulk $Mg_2Cu(H)$ with porous carbon (c) and MgH_2 in porous carbon made by melt infiltration (d) [25]. The last reference was bulk $Mg_2Cu(H)$, which was prepared by induction melting (e).

Bulk $Mg_2Cu(H)$ (e) shows a broad H_2 desorption peak with a maximum around 415 ^oC. The peak temperature of the physical mixture of $Mg_2Cu(H)$ (c) was slightly decreased (410 ^oC) towards lower temperatures. MgH_2 molten on porous carbon showed a peak around 380 ^oC (d). The decrease in temperature for this composite is due to the presence of small MgH_2 particles inside the pores of the carbon support as was described earlier [25]. The peak temperature of the $Mg_2Cu(H)$ composite on non-porous carbon (b) decreased further to approximately 340 ^oC. The most interesting desorption profile is from $Mg_2Cu(H)$ prepared on porous carbon (a), which shows the largest decrease in desorption temperature compared to the other samples. Compared to bulk $Mg_2Cu(H)$ (e), the desorption temperature is approximately 150 ^oC lower.

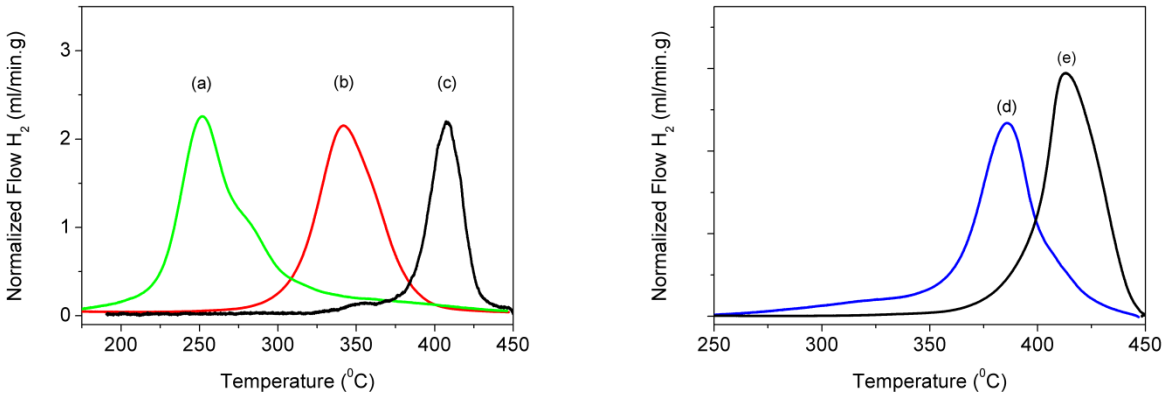

Fig. 3 - 6: TPD profiles (5 $^oC \cdot min^{-1}$) of: (a) $Mg_2Cu(H)$ on porous carbon and (b) $Mg_2Cu(H)$ on non-porous carbon and (c) a physical mixture of $Mg_2Cu(H)$ bulk with porous carbon. The references are (d) MgH_2 on porous carbon and (e) bulk $Mg_2Cu(H)$.

The benefits of using Cu are apparent from a comparison with the MgH_2 reference (Fig. 3 - 6(c)). The supported $Mg_2Cu(H)$-C composites release hydrogen at lower temperatures. The presence of the carbon support only has a minor effect on the temperature for hydrogen release when comparing the physical mixture (c) with pure $Mg_2Cu(H)$ (e). Structural characterization on these samples, as discussed in the previous section, revealed two major differences in the Mg_2Cu-C composites: particle size and distribution of the alloy on the support. By combining these results with the hydrogen release measurements, the trend is that smaller particles desorbed hydrogen at lower temperatures. Also, supported alloy particles on graphite showed lower temperatures for hydrogen release. The presence of a shoulder in sample (a) is most likely caused by the size distribution of the sample, where particles with an average size of 20-30 nm were

dominant as was shown in Fig. 3 - 5. This might also explain the broader peak of sample (b), where a larger difference in size distribution was found varying from 100 nm to 500 nm. The sieved bulk sample (c) turned out to be more uniform in size, leading to a narrower peak. In summary, two effects are causing the shift in desorption temperature. The first is the effect of particle size, which causes the largest shift in the desorption temperature. The other effect is caused by the presence of graphite, which has a minor effect on the desorption reaction.

3.3.4 Cycling and the H_2 sorption equilibrium

Equilibrium desorption isotherms were measured volumetrically on Mg_2Cu-H on porous carbon (Fig. 3 - 7: left) after 2 initial sorption cycles. The isotherms show similar amounts of hydrogen being released at five different temperatures (250 ^{o}C, 275 ^{o}C, 300 ^{o}C, 325 ^{o}C and 350 ^{o}C). Only a single plateau was observed, which means that only one hydride phase is present. The equilibrium pressures were estimated from the center of the plateaus, which were at 0.75 wt% for the isotherms at 250 ^{o}C and 275 ^{o}C; and 1 wt% for the isotherms at 300 ^{o}C 325 ^{o}C and 350 ^{o}C. These plateau pressures were plotted in a van 't Hoff diagram (Fig. 3 - 7: right) and resulted in an enthalpy and entropy of the hydrogen desorption reaction of 66 (±3) kJ·mol^{-1} H_2 and 126 (±10) J·mol^{-1}·K^{-1} respectively. These values are comparable to earlier investigations [12, 21]. The obtained enthalpy for this system is approximately 9 kJ·mol^{-1} lower compared to MgH_2, which is causing the decrease in hydrogen release temperature for the Mg_2Cu(H) system. Therefore, the hydrogen release properties of the Mg_2Cu on porous carbon composite were kinetically and thermodynamically improved with respect to the MgH_2 system.

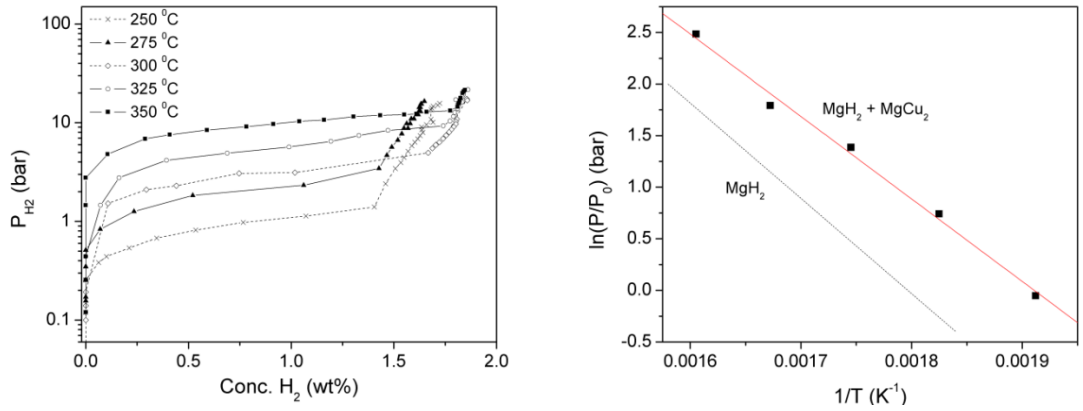

Fig. 3 - 7: Left: H_2 desorption isotherms of Mg_2Cu(H) on porous carbon measured at 250 ^{o}C, 275 ^{o}C, 300 ^{o}C, 325 ^{o}C and 350 ^{o}C. Right: Resulting van 't Hoff plot of Mg_2Cu(H) on porous carbon. The dashed line stands for the reported phase equilibrium between Mg and MgH_2 with ΔH = 75 kJ·mol^{-1} H_2 and ΔS = 136 J·mol^{-1}·K^{-1} [29].

The reversibility of the hydrogen sorption reaction of $Mg_2Cu(H)$ on porous and non-porous carbon was measured gravimetrically (Fig. 3 - 8). Both samples were measured for 7 subsequent cycles and the onset temperature, where the weight loss starts occurring, is close to the thermodynamic equilibrium of ~250 ^{o}C at 1.3 bar H_2. $Mg_2Cu(H)$ on non-porous carbon (Fig. 3 - 8: left) shows an excellent reversibility close to the theoretic storage capacity of 2.6 wt%. For $Mg_2Cu(H)$ on porous carbon (Fig. 3 - 8: right), the first cycle showed almost the full storage capacity and the storage capacity decreased slightly for further cycling and stabilized at 2.0 wt%.

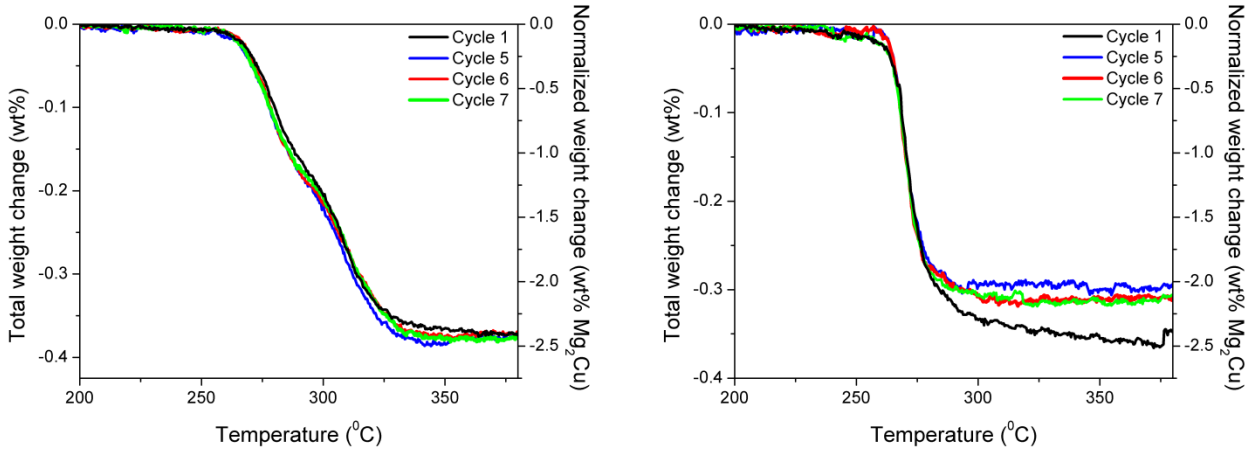

Fig. 3 - 8: H_2 desorption cycles measured gravimetrically of 15 wt% $Mg_2Cu(H)$ on carbon at 1.3 bar H_2 atmosphere with a heating ramp of 1 ^{o}C·min^{-1}. The total and normalized weight change is shown. The quantity of hydrogen released is normalized to the total amount of $Mg_2Cu(H)$, which has a theoretical capacity of 2.6 wt% H_2. Left: $Mg_2Cu(H)$ on non-porous carbon. Right: $Mg_2Cu(H)$ on porous carbon.

Comparing the slopes of the desorption profiles from both $Mg_2Cu(H)$ on porous carbon and non-porous carbon, the slope is steeper for $Mg_2Cu(H)$ on porous carbon. This indicates that the desorption kinetics are faster for this system, while there is no difference in the thermodynamics of both systems, since the onset temperature for desorption is the same. For instance, 80% of the total capacity was released after ~20 min at 280 ^{o}C for $Mg_2Cu(H)$ on porous carbon, while Mg_2Cu on non-porous carbon required ~60 min at a temperature of 320 ^{o}C. This is in line with the TPD results, where faster desorption kinetics were observed for $Mg_2Cu(H)$ on porous carbon due to a smaller average particle size.

It seems that Mg_2Cu on non-porous carbon with large crystallites have a better reversibility than Mg_2Cu on porous carbon containing smaller crystallites. This has also been observed by Jurczyk et al. [10]. The reduction in hydrogen uptake was attributed to excess strain in the

nanoparticles during hydrogen ab- and desorption or induced chemical disorder of the Mg-Cu lattice since Mg diffusion is required for the reaction $MgCu_2 \leftrightarrow Mg_2Cu$. On the other hand, it is also possible that the reduction in uptake could be due to oxidation of the active material due to impurities in the H_2-gasflow used in the experiments. Smaller particles tend to become oxidized faster and more material is lost due to the larger surface area to volume ratio of nanoparticles, assuming that only an oxide shell is formed.

3.3.5 Activation energy for hydrogen desorption of $Mg_2Cu(H)$-C

The lower reaction enthalpy for reaction (Eq. 3 - 1) compared to pure MgH_2, 66 $kJ \cdot mol^{-1}$ H_2 and 75 $kJ \cdot mol^{-1}$ H_2 [30] respectively, results in a lower equilibrium temperature for the $Mg_2Cu(H)$ system. However, TPD results have shown that there is still a large kinetic difference between the different $Mg_2Cu(H)$ phases supported on carbon. To study this difference, a Kissinger analysis was performed to obtain more information on the hydrogen release kinetics [31].

Table 3 - 2: Calculated values for the activation energy (E_A) and pre-exponential factor (A_0). The maximum peak temperatures are given for a heating rate of 5 $^{o}C \cdot min^{-1}$ (Fig. 3 - 6).

Sample	T_{max} (^{o}C)	E_A ($kJ \cdot mol^{-1}$)	A_0 ($1 \cdot s^{-1}$)
(a) $Mg_2Cu(H)$ (~20 nm)	251	97 (± 9)	$1.1 \cdot 10^7$ ($\pm 0.1 \cdot 10^7$)
(b) $Mg_2Cu(H)$ (~300 nm)	341	102 (± 7)	$1.0 \cdot 10^6$ ($\pm 0.1 \cdot 10^6$)
(c) $Mg_2Cu(H)$ (> 1 μm)	407	128 (± 6)	$4.7 \cdot 10^4$ ($\pm 0.2 \cdot 10^4$)
(d) $Mg_2Cu(H)$ (> 1 μm)	406	123 (± 8)	$4.9 \cdot 10^4$ ($\pm 0.2 \cdot 10^4$)

An interesting trend of a decreasing activation energy (E_A) from the bulk (a) to $Mg_2Cu(H)$ on non-porous carbon (b) and $Mg_2Cu(H)$ on porous carbon (c) was observed (Table 3 - 2 and Fig. 3 - 9: left). Bulk $Mg_2Cu(H)$ (d) resulted in similar values for the activation energy and pre-exponential factor as sample (c). Thus, the kinetic properties of $Mg_2Cu(H)$ did not change significantly by only adding carbon. In Fig. 3 - 9: right, the activation energy is plotted against the Mg_2Cu particle sizes. Not only a decrease for the activation energy was found for smaller particles, but also the pre-exponential factor (A_0) is increasing for smaller particles. The value for

the activation energy of the bulk reference is close to what has been found for the hydrogen desorption of pure MgH_2 (126 kJ·mol^{-1}) [32].

The decrease in activation energy for the supported Mg_2Cu particles on porous carbon (a) and non-porous carbon (b) compared to the bulk reference (c) is quite remarkable. Earlier investigations have shown that the activation energy of the hydrogen sorption reaction of pure MgH_2 did not change for different particle- and grain sizes [33]. On the other hand, reaction (1) requires the diffusion of Mg atoms to obtain Mg_2Cu. Lei et al. have proposed a model on how this might occur [11]. This mechanism involves formation of new crystal boundaries of $Mg(H_2)$, $MgCu_2$ and Mg_2Cu during the hydrogen sorption reaction. Smaller particles might have a lower activation energy for reaction (1), because the diffusion distance for Mg atoms to reform Mg_2Cu is shorter. This also might explain the increasing pre-exponential factor. The larger grain boundary between the MgH_2 and $MgCu_2$ phase provide a higher statistical probability for the solid-state reaction of $MgCu_2 \leftrightarrow Mg_2Cu$ to occur, which favors decomposition of MgH_2. The movement of the phase boundary between MgH_2 and $MgCu_2$ is most likely the rate-limiting step, since solid-state diffusion of atoms requires thermal activation.

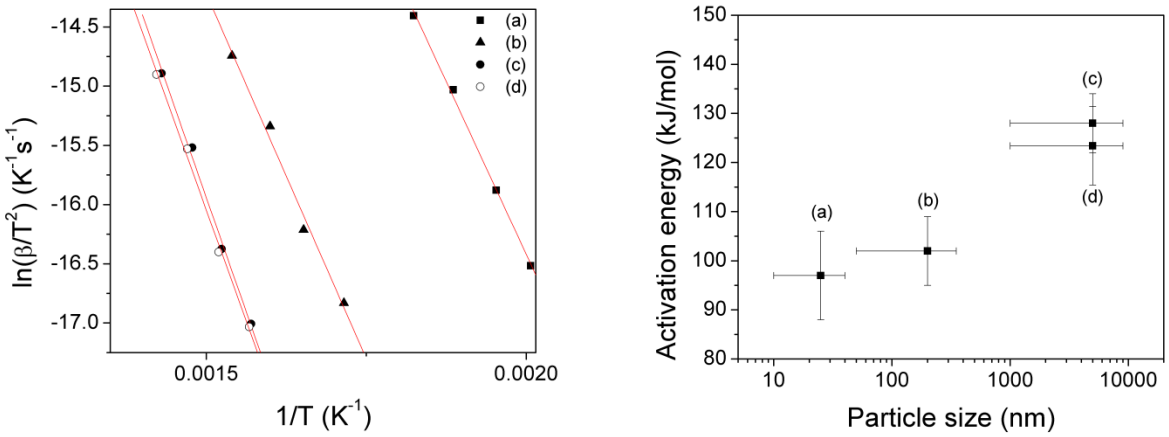

Fig. 3 - 9: Left: Kissinger plot obtained by TPD profiles heated at rates of 1 °C·min^{-1} 2 °C·min^{-1}, 5 °C·min^{-1} and 10 °C·min^{-1}. Sample (a) represents $Mg_2Cu(H)$ on porous carbon. Sample (b) is $Mg_2Cu(H)$ on non-porous carbon. Sample (c) is the $Mg_2Cu(H)$ bulk references obtained by induction melting. Right: Relation between particle size and activation energy for hydrogen desorption of: (a) $Mg_2Cu(H)$ on porous carbon. (b) $Mg_2Cu(H)$ on non-porous carbon. (c) Bulk physical mixture of $Mg_2Cu(H)$ with porous carbon. (d) Bulk Mg_2Cu without carbon.

Another aspect is the effect of the used carbon supports. With this synthesis method, the alloy particles are brought in close contact with the carbon support. This could have an influence on the electronic structure of the alloy leading to a lower activation energy. A similar trend was

observed for MgH_2-C nanocomposites [34]. Smaller and well dispersed alloy particles have relatively more contact with the support material, which enhances the effect. In this case sample (a) has the best dispersion and consists of the smallest crystallites, thus has the lowest activation energy.

3.4 Conclusions

A new method was successfully applied to obtain Mg_2Cu alloy nanoparticles supported on carbon. There are clear synergetic effects of nanosizing and using a carbon support. Different sizes of Mg_2Cu were obtained, where the average size of Mg_2Cu nanoparticles was 20 nm on a porous carbon support. The activation energy for hydrogen desorption of these nanoparticles was lowered from 128 (± 6) $kJ \cdot mol^{-1}$ for a physical mixture of bulk Mg_2Cu with porous carbon to 97 (± 9) $kJ \cdot mol^{-1}$ for supported Mg_2Cu nanoparticles on porous carbon. The kinetics for the solid-state reaction involved in this material was improved. This new synthesis method to obtain nanomaterials with enhanced kinetic properties could be relevant for the development of other Mg-based alloy nanomaterials for application in hydrogen storage or batteries in the future.

Acknowledgements

M. Versluijs-Helder and J. D. Meeldijk are greatly acknowledged for obtaining the SEM and TEM images. A. M. J. van der Eerden is acknowledged for his technical support. Timcal is acknowledged for providing us the carbon samples.

References

(1) Sakintuna, B.; Lamari-Darkrim, F.; Hirscher, M. Metal Hydride Materials for Solid Hydrogen Storage: A Review. *Int J Hydrogen Energy* **2007**, *32*, 1121-1140.

(2) Jain, I. P.; Lal, C.; Jain, A. Hydrogen Storage in Mg: A most Promising Material. *Int J Hydrogen Energy* **2010**, *35*, 5133-5144.

(3) Liang, G.; Huot, J.; Boily, S.; Van Neste, A.; Schulz, R. Catalytic Effect of Transition Metals on Hydrogen Sorption in Nanocrystalline Ball Milled MgH_2-Tm (Tm = Ti, V, Mn, Fe and Ni) Systems. *J. Alloys Compounds* **1999**, *292*, 247-252.

(4) Hanada, N.; Ichikawa, T.; Hino, S.; Fujii, H. Remarkable Improvement of Hydrogen Sorption Kinetics in Magnesium Catalyzed with Nb_2O_5. *J. Alloys Compounds* **2006**, *420*, 46-49.

(5) Murray, J. L. The Al-Mg (Aluminum-Magnesium) System. *Bulletin of Alloy Phase Diagrams* **1982**, *3*, 60-74.

(6) Nayeb-Hashemi, A. A.; Clark, J. B. The Mg-Ni (Magnesium-Nickel) System. *Bulletin of Alloy Phase Diagrams* **1985**, *6*, 238-244.

(7) Moser, D.; Bull, D. J.; Sato, T.; Noréus, D.; Kyoi, D.; Sakai, T.; Kitamura, N.; Yusa, H.; Taniguchi, T.; Kalisvaart, W. P.; Notten, P. Structure and Stability of High Pressure Synthesized Mg-TM Hydrides (TM = Ti, Zr, Hf, V, Nb and Ta) as Possible New Hydrogen Rich Hydrides for Hydrogen Storage. *Journal of Materials Chemistry* **2009**, *19*, 8150-8161.

(8) Milanese, C.; Girella, A.; Bruni, G.; Berbenni, V.; Cofrancesco, P.; Marini, A.; Villa, M.; Matteazzi, P. Hydrogen Storage in Magnesium-Metal Mixtures: Reversibility, Kinetic Aspects and Phase Analysis. *J. Alloys Compounds* **2008**, *465*, 396-405.

(9) Andreasen, A.; Sørensen, M. B.; Burkarl, R.; Møller, B.; Molenbroek, A. M.; Pedersen, A. S.; Vegge, T.; Jensen, T. R. Dehydrogenation Kinetics of Air-Exposed MgH_2/Mg_2Cu and $MgH_2/MgCu_2$ Studied with in Situ X-Ray Powder Diffraction. *Applied Physics A: Materials Science and Processing* **2006**, *82*, 515-521.

(10) Jurczyk, M.; Okonska, I.; Iwasieczko, W.; Jankowska, E.; Drulis, H. Thermodynamic and Electrochemical Properties of Nanocrystalline Mg_2Cu-Type Hydrogen Storage Materials. *J. Alloys Compounds* **2007**, *429*, 316-320.

(11) Lei, J. P.; Huang, H.; Dong, X. L.; Sun, J. P.; Lu, B.; Lei, M. K.; Wang, Q.; Dong, C.; Cao, G. Z. Formation and Hydrogen Storage Properties of in Situ Prepared Mg-Cu Alloy Nanoparticles by Arc Discharge. *Int J Hydrogen Energy* **2009**, *34*, 8127-8134.

(12) Shao, H.; Wang, Y.; Xu, H.; Li, X. Preparation and Hydrogen Storage Properties of Nanostructured Mg_2Cu Alloy. *Journal of Solid State Chemistry* **2005**, *178*, 2211-2217.

(13) Tanaka, M. X.; Takeichi, N.; Takeshita, H. T.; Kiyobayashi, T. Effect of Ball-Milling on the Properties of Mg_2Cu Hydrogen Storage Alloy. *Materials Transactions* **2008**, *49*, 2698-2701.

(14) Cuevas, F.; Korablov, D.; Latroche, M. Synthesis, Structural and Hydrogenation Properties of Mg-Rich MgH_2-TiH_2 Nanocomposites Prepared by Reactive Ball Milling Under Hydrogen Gas. *Physical Chemistry Chemical Physics* **2012**, *14*, 1200-1211.

(15) Cao, P.; Lu, L.; Lai, M. O. Grain Growth and Kinetics for Nanocrystalline Magnesium Alloy Produced by Mechanical Alloying. *Mater. Res. Bull.* **2001**, *36*, 981-988.

(16) Beattie, S. D.; Setthanan, U.; McGrady, G. S. Thermal Desorption of Hydrogen from Magnesium Hydride (MgH_2): An in Situ Microscopy Study by Environmental SEM and TEM. *Int J Hydrogen Energy* **2011**, *36*, 6014-6021.

(17) Nielsen, T. K.; Besenbacher, F.; Jensen, T. R. Nanoconfined Hydrides for Energy Storage. *Nanoscale* **2011**, *3*, 2086-2098.

(18) De Jongh, P. E.; Adelhelm, P. Nanosizing and Nanoconfinement: New Strategies Towards Meeting Hydrogen Storage Goals. *ChemSusChem* **2010**, *3*, 1332-1348.

(19) Zlotea, C.; Cuevas, F.; Andrieux, J.; Matei Ghimbeu, C.; Leroy, E.; Léonel, E.; Sengmany, S.; Vix-Guterl, C.; Gadiou, R.; Martens, T.; Latroche, M. Tunable Synthesis of (Mg-Ni)-Based Hydrides Nanoconfined in Templated Carbon Studied by in Situ Synchrotron Diffraction. *Nano Energy* **2013**, *2*, 12-20.

(20) Bogerd, R.; Adelhelm, P.; Meeldijk, J. H.; De Jong, K. P.; De Jongh, P. E. The Structural Characterization and H_2 Sorption Properties of Carbon-Supported $Mg_{1-x}Ni_x$ Nanocrystallites. *Nanotechnology* **2009**, *20*, 204019.

(21) Reilly, J. J.; Wiswall, R. H. The Reaction of Hydrogen with Alloys of Magnesium and Copper. *Inorg. Chem.* **1967**, *6*, 2220-2223.

(22) Nayeb-Hashemi, A. A.; Clark, J. B. The Cu-Mg (Copper-Magnesium) System. *Bulletin of Alloy Phase Diagrams* **1984**, *5*, 36-43.

(23) Toupance, T.; Kermarec, M.; Louis, C. Metal Particle Size in Silica-Supported Copper Catalysts. Influence of the Conditions of Preparation and of Thermal Pretreatments. *J Phys Chem B* **2000**, *104*, 965-972.

(24) Silva, A. R.; Figueiredo, J. L.; Freire, C.; De Castro, B. Copper(II) Acetylacetonate Anchored Onto an Activated Carbon as a Heterogeneous Catalyst for the Aziridination of Styrene. *Catalysis Today* **2005**, *102-103*, 154-159.

(25) De Jongh, P. E.; Wagemans, R. W. P.; Eggenhuisen, T. M.; Dauvillier, B. S.; Radstake, P. B.; Meeldijk, J. D.; Geus, J. W.; De Jong, K. P. The Preparation of Carbon-Supported Magnesium Nanoparticles using Melt Infiltration. *Chemistry of Materials* **2007**, *19*, 6052-6057.

(26) Hunter, B. A. *IUCR Powder Diffraction* **1997**, *22*, 21.

(27) Gingl, F.; Selvam, P.; Yvon, L. *Acta Cryst. B* **1993**, *49*, 201.

(28) Ohba, T.; Kitano, Y.; Komura, Y. *Acta Cryst.* **1984**, *40*, 1.

(29) Karty, A.; Grunzweig-Genossar, J.; Rudman, P. S. Hydriding and Dehydriding Kinetics of Mg in a Mg/Mg_2Cu Eutectic Alloy: Pressure Sweep Method. *J. Appl. Phys*. **1979**, *50*, 7200-7209.

(30) Larsson, P.; Araújo, C. M.; Larsson, J. A.; Jena, P.; Ahuja, R. Role of Catalysts in Dehydrogenation of MgH_2 Nanoclusters. *Proc. Natl. Acad. Sci. U. S. A.* **2008**, *105*, 8227-8231.

(31) Kissinger, H. E. Reaction Kinetics in Differential Thermal Analysis. *Anal. Chem.* **1957**, *29*, 1702-1706.

(32) Stander, C. M. Kinetics of Decomposition of Magnesium Hydride. *Journal of Inorganic and Nuclear Chemistry* **1977**, *39*, 221-223.

(33) Fátay, D.; Révész, Á; Spassov, T. Particle Size and Catalytic Effect on the Dehydriding of MgH_2. *J. Alloys Compounds* **2005**, *399*, 237-241.

(34) Zhao-Karger, Z.; Hu, J.; Roth, A.; Wang, D.; Kübel, C.; Lohstroh, W.; Fichtner, M. Altered Thermodynamic and Kinetic Properties of MgH_2 Infiltrated in Microporous Scaffold. *Chemical Communications* **2010**, *46*, 8353-8355.

4. Reversible hydrogen storage in $Mg(BH_4)_2$/Carbon nanocomposites

Abstract

$Mg(BH_4)_2$ exhibits a high hydrogen content of 14.9 wt% and the enthalpy of the decomposition reaction (39 $kJ \cdot mol^{-1}$ H_2) corresponds to the desired operation temperature between 25 to 100 ^oC at 1 bar H_2. However, the rate for decomposition is slow, which is caused by high kinetic barriers. In this study, the synthesis of a $Mg(BH_4)_2$/carbon nanocomposite and other magnesium boron hydride compounds were performed by ball milling of MgH_2 nanoparticles supported on carbon aerogel in B_2H_6/H_2 atmosphere. The peak temperature for hydrogen release is decreased from around 300 ^oC for bulk $Mg(BH_4)_2$ to 160 ºC for the newly synthesized magnesium boron hydride compounds. The activation energy for decomposition of the magnesium boron hydride nanocomposite (102 ± 6 $kJ \cdot mol^{-1}$) was lower compared to bulk $Mg(BH_4)_2$ (340 ± 11 $kJ \cdot mol^{-1}$). Furthermore, partial re-formation of $Mg(BH_4)_2$ after dehydrogenation is achieved at 270 ºC and a pressure range of 80 to 150 bar H_2 for the nanocomposite. Nanosizing was able to increase the decomposition rate of the magnesium boron hydride compounds and allowed partial reversibility to form $Mg(BH_4)_2$ and $MgB_{12}H_{12}$.

4.1 Introduction

Hydrogen is regarded as a clean energy carrier for the future [1, 2]. Achieving safe and efficient hydrogen storage is one of the key technological challenges for wide use of hydrogen as fuel. Metal boron hydrides, with high gravimetric and volumetric densities of hydrogen, have been extensively investigated for solid state hydrogen storage [3-5]. Among them, magnesium borohydride, i.e. $Mg(BH_4)_2$, shows a hydrogen capacity of 14.9 wt% and an favorable enthalpy change of 39 $kJ \cdot mol^{-1}$ H_2 in dehydrogenation according to (Eq. 4 - 1) [6-8].

$$Mg(BH_4)_2 \rightarrow MgB_2 + 4\ H_2 \qquad \text{(Eq. 4 - 1)}$$

Although the dehydrogenation enthalpy change allows for hydrogen desorption at temperatures in the range of 25 °C to 100 °C at 1 bar H_2, the dehydrogenation only occurred above 250 °C for bulk $Mg(BH_4)_2$ [9-11]. Rehydrogenation of MgB_2 requires high hydrogen pressures and high temperatures (e.g. 95 MPa H_2, 400 °C) [12]. Numerous studies have revealed that the decomposition reaction (1) occurs in multi steps involving the formation of Mg-B-H ternary intermediates such as $Mg(B_3H_8)_2$, $MgB_{12}H_{12}$ etc. [11, 13-15] The partial decomposition of $Mg(BH_4)_2$ to $Mg(B_3H_8)_2$ is reversible at 250 °C and 120 bar for 2.5 wt% H_2. The migration of atoms such as Mg and B in the formation process of $[B_{12}H_{12}]^{2-}$ from the reconstruction of $[BH_4]^-$ as well as the breaking of B-H covalent bonds in $[BH_4]^-$ are considered to result in the slow kinetics for the dehydrogenation reaction of $Mg(BH_4)_2$ [15].

An effective approach to accelerate the reaction kinetics is to reduce the particle size and form nanomaterials [16-19]. By ball milling of MgB_2 in high pressure hydrogen atmosphere, nanostructured $Mg(BH_4)_2$ was formed with enhanced hydrogen desorption properties [20, 21]. Incorporation in a nanoporous scaffold can be used to avoid sintering in the de-/ab-sorption cycles of nanostructured $Mg(BH_4)_2$ [22, 23]. Deposition of $Mg(BH_4)_2$ in activated carbon via wet impregnation was carried out, resulting in reduced hydrogen release temperature, but residues of solvent and unconfined $Mg(BH_4)_2$ were reported [22]. In a recent research, the temperature of hydrogen desorption was reduced to 155 °C by combining nanoconfinement and a Ni catalyst [23]. However, the regeneration of $Mg(BH_4)_2$ under mild conditions from the dehydrogenated state has not been reported so far.

Previous studies have demonstrated that solvent free metal boron hydrides, such as $LiBH_4$, $Mg(BH_4)_2$, $Ca(BH_4)_2$ and $Y(BH_4)_3$, can be synthesized via a reaction between the corresponding metal hydrides and B_2H_6 [24, 25]. In this study, this method was applied to synthesize nanostructured $Mg(BH_4)_2$. MgH_2 nanoparticles supported on carbon served as precursors and were ball milled in B_2H_6/H_2 atmosphere to form $Mg(BH_4)_2$ according to (Eq. 4 - 2).

$$MgH_2 + B_2H_6 \rightarrow Mg(BH_4)_2 \qquad \text{(Eq. 4 - 2)}$$

To investigate the influence of different carbon additives, carbon aerogel (porous structure) and graphite (nonporous structure) were compared. The formation of nanostructured $Mg(BH_4)_2$ was observed, which released hydrogen at lower temperatures compared to bulk $Mg(BH_4)_2$. Partially re-formation of the nanostructured $Mg(BH_4)_2$ also occurred under milder conditions compared to earlier reports [12].

4.2 Experimental

Carbon aerogel (CA) was synthesized through resorcinol-formaldehyde condensation [26]. Resorcinol (Sigma Aldrich 99%, 8.65 g, 79 mmol), formaldehyde (Fisher chemical, analytical reagent 37-41%, stabilized by 12% methanol, 12.89 g, 158 mmol) and sodium carbonate (Across organics, anhydrous pure, 0.017 g, 0.16 mmol) were dissolved in deionized water. After curing (1 day at room temperature, 1 day at 60 ºC and 3 days at 90 ºC), the obtained gel was cooled, powdered and subsequently washed with acetone. The gel was pyrolized in a tubular oven at 800 ºC for 10 hours in an Ar flow and stored in an Ar purified glovebox (MBraun Labmaster) after cooling to room temperature. Non-porous graphite (KS-6), obtained from Timcal, was pre-treated at 600 ºC overnight in an Ar flow. Unless otherwise stated, all sample handlings were carried out in the glovebox under Ar atmosphere to prevent (hydro-) oxidation.

Deposition of MgH_2 nanoparticles supported on carbon occurred via a heat treatment of a mixture of MgH_2 and the carbon support above the melting temperature of Mg [27]. In a typical experiment, 0.9 g of CA or KS-6 was mixed and ground with 0.1 g of MgH_2 in a mortar to obtain a mixture with 10 wt% MgH_2. The mixture was placed in a graphite cup which was inserted in a stainless steel sample holder. The sample was then heated in a tubular oven with 10 ºC·min^{-1} to 658 ºC and dwelled for 24 min under an Ar flow. Hydrogenation of the samples was performed at 80 bar H_2 and 300 ºC for 10 h in an autoclave (Parr). The MgH_2 supported on carbon aerogel

(CA) and on non-porous graphite (KS-6) are labeled as MH-CA and MH-KS6, respectively. All samples investigated in this study are listed in Table 4 - 1.

Table: 4 - 1 Assignment of the investigated samples. Additionally, a physical mixture of bulk $Mg(BH_4)_2$ reference with CA in a mass ration of 1 to 5 is labeled as MBH-CA-PM.

Carbon supports	MgH_2 supported on carbon	Ball milled in B_2H_6/H_2
carbon aerogel (CA)	MH-CA	MBH-CA
non-porous graphite (KS-6)	MH-KS6	MBH-KS6

$LiZn_2(BH_4)_5$, synthesized by ball milling a mixture of $ZnCl_2$ (Sigma–Aldrich, 99.9%) and $LiBH_4$ (Katchem, 95%), was used as a B_2H_6 source. Release of B_2H_6 and H_2 due to decomposition occurs above 100 ºC according to Ravensbaek et al [28]. The milling vial was filled with 500 mg MH-CA or MH-KS6 and connected to the B_2H_6 source. The whole system was purged with hydrogen and evacuated. Subsequently, the diborane source was heated up to 150 ºC to fill the system with a B_2H_6/H_2 (1 : 1) atmosphere. After the 10 bars of diborane pressure was generated, ball milling was carried out for 3 days and the progress of the subsequent reaction was monitored by the pressure change in the milling vial. The samples of MH-CA and MH-KS6 after B_2H_6 treatment were labeled as MBH-CA and MBH-KS6, respectively. Ideally, 10 wt% of MgH_2 in MH-CA could result in 18 wt% of $Mg(BH_4)_2$ (according to Eq. 4 - 2) in MBH-CA. In order to compare the effect of carbon addition, a physical mixture of $Mg(BH_4)_2$ with CA, labeled as MBH-CA-PM, was prepared by ball milling of bulk $Mg(BH_4)_2$ reference (Sigma-Aldrich, 95%) and CA in a mass ratio of 1 to 5 under 10 bar H_2 for 3 days. Also, pure CA was ball milled in B_2H_6/H_2 and H_2 atmosphere, respectively, to investigate the possible reactions between CA with B_2H_6 and H_2.

N_2-physisorption (Micromeritics TriStar 3000) was performed at -196 ^oC for porosity analysis. The total pore volume was obtained at p/p_0 = 0.997. The samples were prepared in a capped quartz sample tube in the glovebox and were directly measured. The mesopore size distribution was analyzed with the Barrett-Joyner-Halenda (BJH) method from the adsorption branch of the isotherm with a carbon black thickness equation as reference.

X-ray diffraction (XRD) measurements were performed using a Bruker D8 diffractometer equipped with a Goebel mirror selecting $Cu_{K\alpha}$ radiation (λ = 1.5418 Å) and a linear detector

system (Vantec). Samples for XRD measurements were filled and sealed in inert atmosphere into glass capillaries (diameter, 0.7 mm; wall thickness, 0.01 mm). Each scan was performed from 10^o-70^o 2θ with a step size of 0.015^o and an acquisition time of 7 s per step.

For transmission electron microscopy (TEM) observation, a small amount of sample was placed on a 200 mesh Cu grid coated with a carbon polymer film in the glovebox. The sample was exposed for 5 s to air during the insertion of the sample holder into the microscope. Images were recorded with an FEI Tecnai 20F (equipped with a Field Emission Gun) and operated at 200 kV in bright field mode. Elemental analysis was performed with Energy-dispersive X-ray spectroscopy (EDX) and electron energy loss spectroscopy (EELS), which are connected to the microscope.

Solid state ^{11}B magic angle spinning nuclear magnetic resonance (MAS NMR) experiments were performed on a Bruker Avance-400 NMR spectrometer using a 4 mm CP-MAS probe. The ^{11}B NMR spectra were recorded at 128.38 MHz at 12 kHz sample rotation applying a Hahn echo pulse sequence to suppress the broad background resonance of boron nitride of the probe. Pulse lengths of 1.5 μs (π/12 pulse) and 3.0 μs were applied for the excitation and echo pulses, respectively. ^{11}B NMR chemical shifts are reported in parts per million (ppm) externally referenced to a 1M $B(OH)_3$ aqueous solution at 19.6 ppm as an external standard sample. Reference sample $K_2B_{12}H_{12}$ was purchased from Katchem. The dehydrogenated samples were measured after heating to 90 ^{o}C, 250 ^{o}C and 360 ^{o}C respectively with 5 ºC·min^{-1} in an Ar-flow. Heating was stopped after the desired temperature was reached and measured after cooling to room temperature.

Thermogravimetric (TG) measurements were carried out by using a magnetic suspension balance (Rubotherm), with a heating rate of 5 ºC·min^{-1} and an Ar flow of 200 ml·min^{-1}. Temperature programmed desorption combined with mass-spectrometry (TPD-MS) (Micromeritics AutoChem II 2920 and Pfeiffer Vacuum OmniStar^{TM}) measurements were performed to analyze the decomposition reaction of the samples. Approximately 50 mg of sample was taken for each measurement. The experiments were carried out in an Ar flow of 25 ml·min^{-1} with a temperature ramp of 5 ºC·min^{-1} up to 500 ºC. The masses of B_2H_6 and H_2 were recorded simultaneously over time.

The activation energy (E_a) of hydrogen desorption reaction was determined by using the Kissinger method involving the application of (Eq. 4 - 3) [29].

$$\ln(\beta/T^2_{max}) = - E_a/RT_{max} + C \qquad \text{(Eq. 4 - 3)}$$

Where β is the heating rate, T_{max} is the peak temperature, R is the gas constant and C is a constant. TPD measurements with different heating rates of 2, 5, 10 and 15 ºC·min^{-1} were accordingly carried out.

4.3 Results and discussion

4.3.1 Characterization

CA exhibits a porous structure with a surface area (S_{BET}) of 605 m^2·g^{-1}, a total pore volume of 0.52 cm^3 g^{-1} and an average pore size of 10 nm. After infiltration with Mg, the pore volume of CA is slightly decreased, as shown in Fig. 4 - 1. The pore volume is reduced to zero in MBH-CA, indicating that the porous structure of CA was destroyed during the ball milling process.

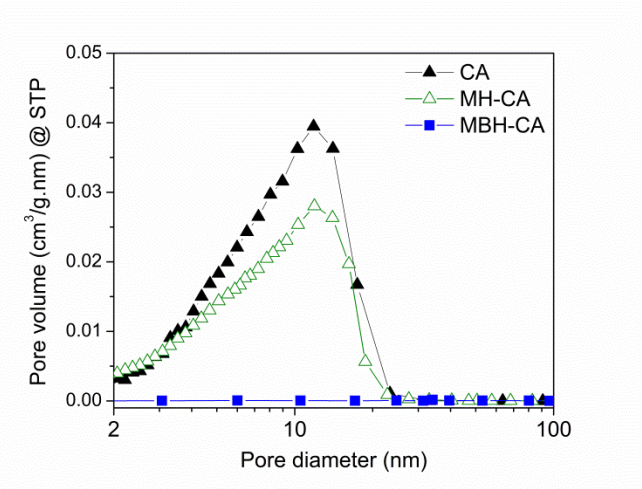

Fig. 4 - 1: Pore size distribution of CA, MH-CA and MBH-CA.

The XRD patterns of MH-CA and MH-KS6 before and after ball milling in B_2H_6 are shown in Fig. 4 - 2: left. Diffraction lines of MgH_2 and Mg are observed in samples MH-CA and MH-KS6, indicating the presence of crystalline MgH_2 and Mg. After ball milling in B_2H_6/H_2, the reflections of Mg and MgH_2 disappeared in MBH-CA, while the peak intensities of graphite, MgH_2 and Mg were strongly reduced in MBH-KS6. No observation of new reflections implies that the newly formed compounds by ball milling in B_2H_6/H_2 atmosphere are amorphous or nanocrystalline. Thereby, NMR spectroscopy is a suitable choice for further phase identification.

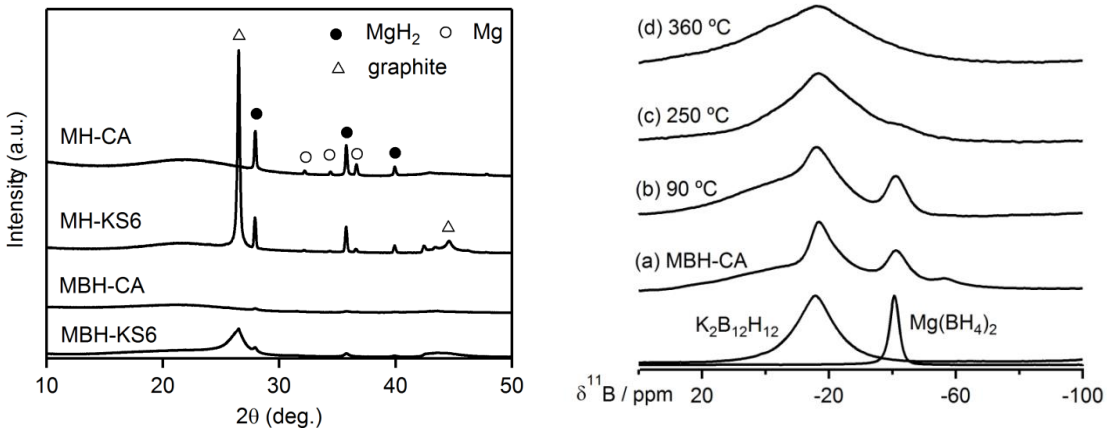

Fig. 4 - 2: Left: XRD patterns of carbon supported MgH_2 samples: MH-CA and MH-KS6, and samples after ball milling in B_2H_6/H_2: MBH-CA and MBH-KS6. Right: ^{11}B MAS NMR spectra of (a) as-synthesized MBH-CA, and MBH-CA heated at (b) 90 °C, (c) 250 °C and (d) 360 °C, respectively, compared to the reference samples $K_2B_{12}H_{12}$ and $Mg(BH_4)_2$

The ^{11}B MAS NMR spectrum of MBH-CA in Fig. 4 - 2: right (a) shows two major resonances at -41 and -16 ppm. The resonance at -41 ppm shows the same chemical shift as the reference sample $Mg(BH_4)_2$, indicating the formation of $Mg(BH_4)_2$ in MBH-CA. The signal at -16 ppm belongs to the $[B_{12}H_{12}]^{2-}$ species, which may be formed by a reaction between the newly formed $Mg(BH_4)_2$ compound and B_2H_6. The presence of boron in MBH-CA is also confirmed by EELS

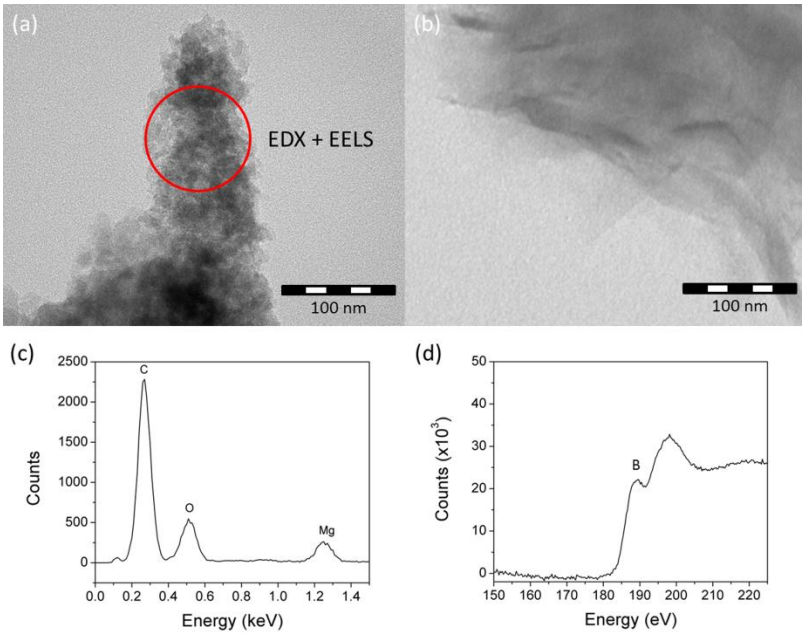

Fig. 4 - 3: Bright field TEM image of (a) MBH-CA, (b) MBH-KS6 (c) EDX and (d) EELS spectra of (a). The red circle in (a) shows the area for EDX and EELS measurements of MBH- CA.

as shown in Fig. 4 - 3(d). By integrating the individual peak area in Fig. 4 - 2: right (a), the mass ratio of $Mg(BH_4)_2$ to $MgB_{12}H_{12}$ is estimated to be 1 to 4.5. Regarding the initial amount of Mg is 10 wt% in MH-CA, the amount of $Mg(BH_4)_2$ and $MgB_{12}H_{12}$ in MBH-CA are estimated to be 6 and 27 wt%, respectively, with the remaining 67 wt% being carbon. ^{11}B MAS NMR measurements on MBH-KS6 were not successful**,** due to the presence of unpaired electrons in graphite leading to a loss of the NMR signal [30, 31].

4.3.2 Hydrogen desorption properties

The hydrogen desorption behaviors of MBH-CA, MBH-KS6 and two reference samples were examined by TPD and MS. In Fig. 4 - 4 (a), the desorption of the bulk $Mg(BH_4)_2$ reference starts from 250 ºC. The three desorption peaks within a temperature range of 270 to 400 ºC correspond to three decomposition steps [9]. Only traces of B_2H_6 release was detected by MS, as shown in Fig. 4 - 4(b). MBH-CA-PM shows a broad desorption peak within the same temperature region as bulk $Mg(BH_4)_2$.

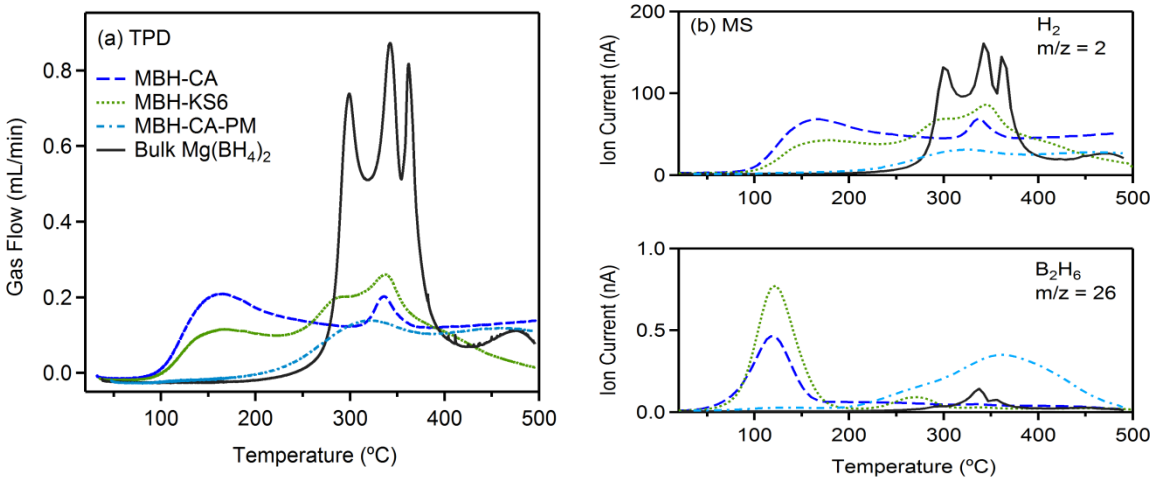

Fig. 4 - 4: (a) TPD profiles for H_2 release and (b) MS profiles for H_2 and B_2H_6 release of MBH-CA, MBH-KS6, MBH-CA-PM and bulk $Mg(BH_4)_2$.

The hydrogen desorption behaviors of MBH-CA and MBH-KS6 (Fig. 4 - 4 (a)) are quite different from the reference samples. The desorption of MBH-CA starts around 100 ºC, approximately 150 ºC lower than that of bulk $Mg(BH_4)_2$, which is in good agreement with TG results in Fig. 4 - 5: left. The first desorption step of MBH-CA occurs at 160 ºC and the second step at 335 ºC. The simultaneous MS measurement in Fig. 4 - 4(b) reveals that the gas release in

the TPD measurement is mainly due to the release of H_2 and only a slight amount of B_2H_6 release is detected. The first desorption peak of MBH-KS6 is also found at 160 ºC (Fig. 4 - 4(a)). In addition, two other desorption peaks are observed at 285 and 336 ºC, within a similar temperature range as the decomposition of bulk $Mg(BH_4)_2$. In summary, the synthesized magnesium boron hydrides supported on different carbon matrixes showed different desorption behaviors compared to bulk $Mg(BH_4)_2$.

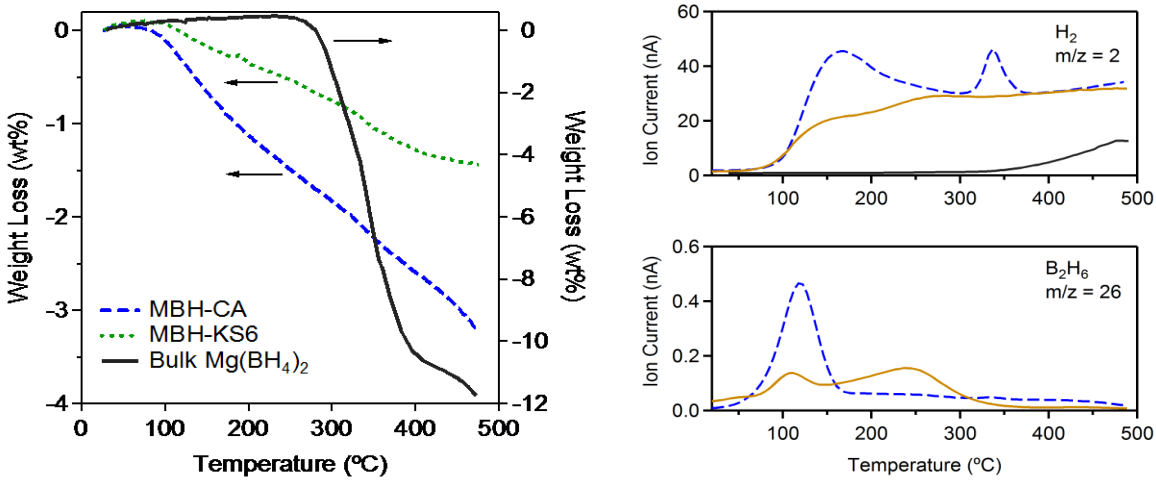

Fig. 4 - 5: Left: TG curves of MBH-CA, MBH-KS6 and bulk $Mg(BH_4)_2$ reference, respectively. Measured with 200 $ml \cdot min^{-1}$ Ar flow and a heating rate of 5 $ºC \cdot min^{-1}$. Right: MS profiles for H_2 and B_2H_6 release of MBH-CA (blue, dashed line), and CA ball milled in a B_2H_6/H_2 (grey line) and CA ball milled in H_2 atmosphere (black line) for 3 days.

Note that the release of B_2H_6 occurs at a lower temperature (below 100 ºC) than that of H_2 for both MBH-CA and MBH-KS6 (shown in Fig. 4 - 4(b)). The released B_2H_6 might possibly originate from physisorption or trapping of B_2H_6 on carbon during the ball milling process. To verify this hypothesis, pure CA was ball milled under B_2H_6/H_2 and pure H_2 atmosphere, respectively, and examined by MS. In Fig. 4 - 5: right, MS data of MBH-CA and milled CA are compared. It is clearly observed that H_2 is also desorbed from the ball milled CA in B_2H_6/H_2 but without distinct peaks, and the H_2 release profile of CA appears to follow the baseline of that of MBH-CA. Defects could be created in the carbon structure during the ball milling process, possibly leading to the formation of B-C, C-H or B-H-C chemical bonds. Ball milling of CA in pure H_2 atmosphere only results in traces of hydrogen release above 350 ºC, possibly due to the formation of stable C-H bonds. Therefore, the hydrogen desorption peaks of MBH-CA at 160 and 335 ºC (Fig. 4 - 5: right) can be ascribed to the decomposition of the synthesized magnesium

boron hydrides present in the compositions. The ball milled CA under B_2H_6/H_2 also shows a different B_2H_6 release behavior compared to MBH-CA, i.e. two B_2H_6 peaks at 120 and 250 ºC respectively, and the B_2H_6 release at 120 ºC is very limited. This indicates that the B_2H_6 release around 120 ^oC mainly originates from decomposition of the magnesium boron hydrides and supports the fact that decomposition occurs at low temperature.

To clarify the evolution of the boron species in MBH-CA during the decomposition process, MBH-CA was decomposed at different temperatures and examined by ^{11}B MAS NMR. As shown in Fig. 4 - 3: right, the resonance assigned to $[BH_4]^-$ is present at 90 ºC and disappears at 250 ºC.

4.3.3 Reversibility

According to the results in Fig. 4 - 4 and 4 - 5, the hydrogen desorption from $Mg(BH_4)_2$ in MBH-CA shows apparently two steps and is completed below 360 ºC. To examine the reversibility of $Mg(BH_4)_2$ supported on CA, the sample of MBH-CA was decomposed at 360 ºC and rehydrogenated under 150 bar H_2 at 200 or 270 ºC and under 80 bar at 200 ºC, respectively. The ^{11}B MAS NMR spectra of the rehydrogenated samples are shown in Fig. 4 - 6. The partial re-formation of $Mg(BH_4)_2$ is observed at both 200 and 270 ºC under 150 bar. Carrying out rehydrogenation at a lower H_2 pressure of 80 bar at 200 ºC, traces of $Mg(BH_4)_2$ were formed as well. In contrast, the rehydrogenation of bulk $Mg(BH_4)_2$ requires higher pressures (e.g. 900 to 950 bar of H_2) and higher temperatures (e.g. 390 to 400 ºC) [12, 30].

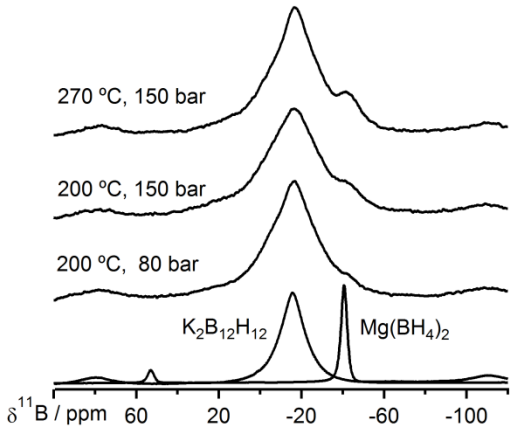

Fig. 4 - 6: ^{11}B MAS NMR spectra of MBH-CA rehydrogenated at 200 ºC and 270 ºC, respectively.

Fig. 4 - 7 shows the hydrogen desorption of the sample rehydrogenated at 270 ºC. In the 2nd cycle, less hydrogen is released and the hydrogen desorption temperature is increased to 200 ºC, indicating the deterioration of the H_2 desorption properties. In addition, desorption of B_2H_6 was also observed at 120 ºC, similar to that of the as-synthesized sample (Fig. 4 - 4).

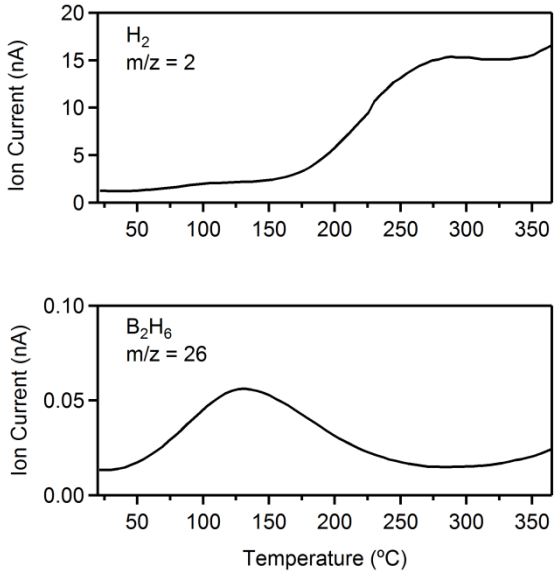

Fig. 4 - 7: MS profiles of MBH-CA rehydrogenated at 270 ºC and 150 bar for 20h.

4.4 Discussion

A nanocomposite of magnesium boron hydride supported on carbon, mainly consisting of $MgB_{12}H_{12}$ and $Mg(BH_4)_2$, was successfully synthesized by ball milling of supported MgH_2 nanoparticles on carbon aerogel in B_2H_6/H_2 atmosphere at room temperature, exhibiting a lower desorption temperature and partial reversibility under milder conditions compared to bulk $Mg(BH_4)_2$. The hydrogen release occurring at temperatures of the MBH-CA composite is mainly attributed to the decomposition of nanostructured $Mg(BH_4)_2$. Reducing the particle sizes of hydrides improves the H_2 sorption kinetics and decreased the decomposition temperature [31-35]. The improvement in kinetics by nanosizing arises from the lowered activation barrier and the shortened diffusion distance for atoms. The activation energies (E_a) of the first hydrogen desorption step of MBH-CA and bulk $Mg(BH_4)_2$ are compared in Fig. 4 - 8. In sample MBH-CA, the nanostructured $Mg(BH_4)_2$ shows a lowered E_a of 102 ± 6 kJ·mol^{-1}, compared to 340 ± 11 kJ·mol^{-1} for bulk $Mg(BH_4)_2$.

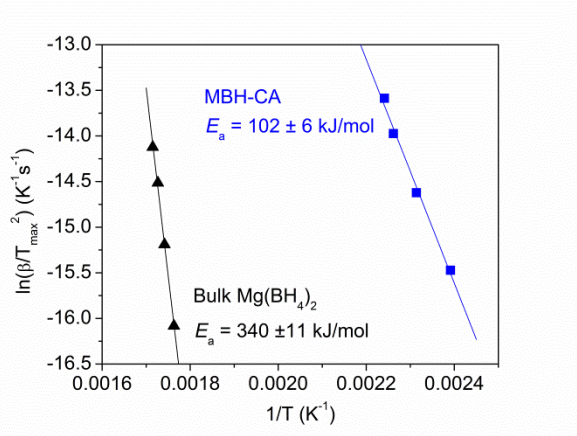

Fig. 4 - 8: Kissinger plot of the first hydrogen desorption step for MBH-CA and bulk $Mg(BH_4)_2$

The hydrogen desorption process of $Mg(BH_4)_2$ is altered from an apparently 3-step reaction for the bulk $Mg(BH_4)_2$ to a 2-step reaction for MBH-CA or one of these steps occurs so much faster or over a broader temperature range that merging of peaks in the hydrogen release profile occurred. The presence of carbon did not have a catalytic effect improving the decomposition of the MBH-CA sample. When carbon aerogel was introduced into bulk $Mg(BH_4)_2$ in a mass ratio of 5 to 1 by ball milling, the hydrogen desorption temperature was only slightly reduced, as observed in sample MBH-CA-PM (shown in Fig. 4 - 4).

Since the porous structure of carbon aerogel in MBH-CA was destroyed during the milling process, a possible effect due to nanoconfinement cannot be determined. The newly formed $Mg(BH_4)_2$ is very likely dispersed homogeneously on the non-porous carbon matrix with this synthesis method (Fig. 4 - 3(a)). In this sense, ball milling of MgH_2 supported on non-porous graphite in B_2H_6/H_2 could also lead to the formation of nanostructured $Mg(BH_4)_2$, which is responsible for the hydrogen desorption reaction to occur at 160 ºC. The hydrogen desorption reactions at 285 and 336 ºC took place within the temperature range similar to the desorption of bulk $Mg(BH_4)_2$ (Fig. 4 - 4(b)), implying the existence of bulk $Mg(BH_4)_2$ in MBH-KS6. This could be related to the observation of some crystalline MgH_2 in the XRD pattern of MBH-KS6 (Fig. 4 - 2: left).

Fig. 4 - 9 summarizes schematically the images of bulk $Mg(BH_4)_2$, MBH-CA-PM, MBH-KS6 and MBH-CA, and their temperature ranges for hydrogen desorption are compared. Apparently, the smaller the particle size, the lower the desorption temperature; this tendency implies a relation between particles size and hydrogen sorption performance of $Mg(BH_4)_2$, similar to the

observations in other hydrides such as $LiBH_4$ and MgH_2 [32, 36, 37]. The same argument may also apply to the improved rehydrogenation performance of MBH-CA.

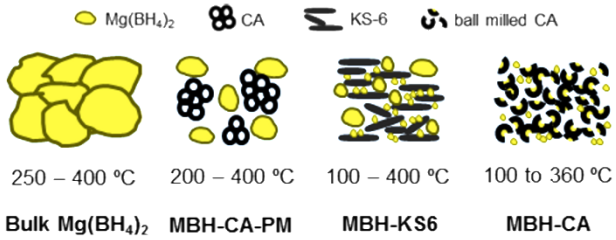

Fig. 4 - 9: Schematic images of bulk $Mg(BH_4)_2$, MBH-CA-PM, MBH-KS6 and MBH-CA, with corresponding temperature ranges for hydrogen desorption.

However, due to the destruction of the pore structure of the carbon matrix in MBH-CA by ball milling, particle growth during the desorption and absorption process could take place. As a consequence, the hydrogen desorption temperature was increased and the amount of hydrogen desorbed was decreased during the second desorption cycle. About 30% of hydrogen can be re-absorbed in the second cycle, as shown in Fig. 4 - 10. Despite that, the B_2H_6 desorption in the 2nd cycle (Fig. 4 - 7) remains at the same temperature compared to the as-synthesized MBH-CA (Fig. 4 - 4(b)), indicating the partial formation of $Mg(BH_4)_2$ after rehydrogenation as was also observed in NMR (Fig. 4 - 6).

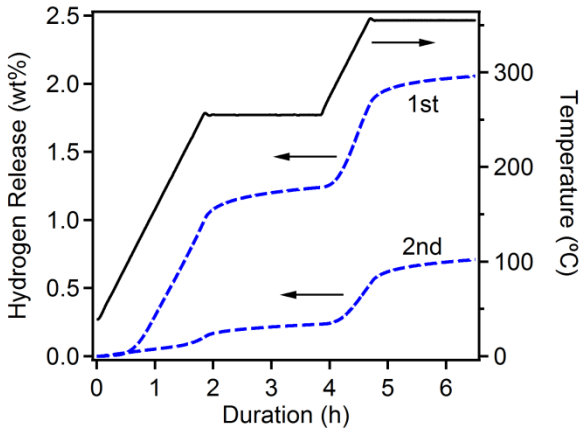

Fig. 4 - 10: The hydrogen desorption of MBH-CA in the two cycles. Rehydrogenation reaction was carried out at 270 ºC and 150 bar H_2 for 20 h. Approximately 30 % of hydrogen is reversibly stored in the 2nd cycle. Conditions: 200 ml·min^{-1} Ar flow and a heating rate of 5 ºC·min^{-1}.

4.5 Conclusions

Ball milling of MgH_2 supported on carbon matrix in B_2H_6/H_2 atmosphere has led to formation of mainly $MgB_{12}H_{12}$ and $Mg(BH_4)_2$. ^{11}B MAS NMR measurement confirmed the formation of $MgB_{12}H_{12}$ and $Mg(BH_4)_2$. MBH-CA exhibits a markedly reduced activation energy of 102 ± 6 $kJ \cdot mol^{-1}$ for decomposition compared to 340 ± 11 $kJ \cdot mol^{-1}$ for bulk $Mg(BH_4)_2$. A low hydrogen release temperature (160 ºC) was found. When non-porous graphite was used as the carbon support, the formed nanocomposite (MBH-KS6) also shows a hydrogen desorption peak at 160 ºC. In addition, the desorption reactions occurring at 285 and 336 ºC within a similar temperature range as the decomposition of bulk $Mg(BH_4)_2$ implying the presence of bulk $Mg(BH_4)_2$ in MBH-KS6 as well.

Partial re-formation of $Mg(BH_4)_2$ from dehydrogenated MBH-CA was achieved at 200 ºC and 80 to 150 bar H_2. The deterioration in hydrogen desorption performance during the 2^{nd} sorption cycle is possibly caused by particle growth due to destruction of the porosity of the carbon support during ball-milling. Therefore, maintenance of the nanostructures is considered to be important for the reversible hydrogen sorption performance of $Mg(BH_4)_2$ under mild conditions.

Acknowledgements

J.D. Meeldijk is acknowledged for acquiring the TEM images and J. Geus is thanked for his advice on the EELS measurements. Timcal is acknowledged for providing the carbon support materials.

References

(1) Schlapbach, L.; Züttel, A. Hydrogen-Storage Materials for Mobile Applications. *Nature* **2001**, *414*, 353-358.

(2) Züttel, A.; Remhof, A.; Borgschulte, A.; Friedrichs, O. Hydrogen: The Future Energy Carrier. *Philosophical Transactions of the Royal Society A: Mathematical, Physical and Engineering Sciences* **2010**, *368*, 3329-3342.

(3) Graetz, J. New Approaches to Hydrogen Storage. *Chem. Soc. Rev.* **2009**, *38*, 73-82.

(4) Yang, J.; Sudik, A.; Wolverton, C.; Siegel, D. J. High Capacity Hydrogen Storage Materials: Attributes for Automotive Applications and Techniques for Materials Discovery. *Chem. Soc. Rev.* **2010**, *39*, 656-675.

(5) Li, H. ; Yan, Y.; Orimo, S. ; Züttel, A.; Jensen, C. M. Recent Progress in Metal Borohydrides for Hydrogen Storage. *Energies* **2011**, *4*, 185-214.

(6) Van Setten, M. J.; De Wijs, G. A.; Fichtner, M.; Brocks, G. A Density Functional Study of a-$Mg(BH_4)_2$. *Chemistry of Materials* **2008**, *20*, 4952-4956.

(7) Ozolins, V.; Majzoub, E. H.; Wolverton, C. First-Principles Prediction of Thermodynamically Reversible Hydrogen Storage Reactions in the Li-Mg-Ca-B-H System. *J. Am. Chem. Soc.* **2009**, *131*, 230-237.

(8) Yan, Y.; Li, H.; Nakamori, Y.; Miwa, N. O. K.; Towata, S.; Orimo, S. Differential Scanning Calorimetry Measurements of Magnesium Borohydride $Mg(BH_4)_2$. *Materials Transactions* **2008**, *49*, 2751-2752.

(9) Li, H..; Kikuchi, K.; Nakamori, Y.; Ohba, N.; Miwa, K.; Towata, S.; Orimo, S. Dehydriding and Rehydriding Processes of Well-Crystallized $Mg(BH_4)_2$ Accompanying with Formation of Intermediate Compounds. *Acta Materialia* **2008**, *56*, 1342-1347.

(10) Hanada, N.; Chlopek, K.; Frommen, C.; Lohstroh, W.; Fichtner, M. Thermal Decomposition of $Mg(BH_4)_2$ Under He Flow and H_2 Pressure. *Journal of Materials Chemistry* **2008**, *18*, 2611-2614.

(11) Soloveichik, G. L.; Gao, Y.; Rijssenbeek, J.; Andrus, M.; Kniajanski, S.; Bowman Jr., R. C.; Hwang, S. J.; Zhao, J. C. Magnesium Borohydride as a Hydrogen Storage Material: Properties and Dehydrogenation Pathway of Unsolvated $Mg(BH_4)_2$. *Int J Hydrogen Energy* **2009**, *34*, 916-928.

(12) Severa, G.; Rönnebro, E.; Jensen, C. M. Direct Hydrogenation of Magnesium Boride to Magnesium Borohydride: Demonstration of >11 Weight Percent Reversible Hydrogen Storage. *Chemical Communications* **2010**, *46*, 421-423.

(13) Chong, M.; Karkamkar, A.; Autrey, T.; Orimo, S.; Jalisatgi, S.; Jensen, C. M. Reversible Dehydrogenation of Magnesium Borohydride to Magnesium Triborane in the Solid State Under Moderate Conditions. *Chemical Communications* **2011**, *47*, 1330-1332.

(14) Hwang, S. J.; Bowman Jr., R. C.; Reiter, J. W.; Rijssenbeek, J.; Soloveichik, G. L.; Zhao, J. C.; Kabbour, H.; Ahn, C. C. NMR Confirmation for Formation of $[B12H12]^{2-}$ Complexes during Hydrogen Desorption from Metal Borohydrides. *Journal of Physical Chemistry C* **2008**, *112*, 3164-3169.

(15) Li, H. W.; Miwa, K.; Ohba, N.; Fujita, T.; Sato, T.; Yan, Y.; Towata, S.; Chen, M. W.; Orimo, S. Formation of an Intermediate Compound with a $B_{12}H_{12}$ Cluster: Experimental and Theoretical Studies on Magnesium Borohydride $Mg(BH_4)_2$. *Nanotechnology* **2009**, *20*, 204013.

(16) Chen, X.; Li, C.; Grätzel, M.; Kostecki, R.; Mao, S. S. Nanomaterials for Renewable Energy Production and Storage. *Chem. Soc. Rev.* **2012**, *41*, 7909-7937.

(17) Fichtner, M. Nanotechnological Aspects in Materials for Hydrogen Storage. *Advanced Engineering Materials* **2005**, *7*, 443-455.

(18) Vajo, J. J. Influence of Nano-Confinement on the Thermodynamics and Dehydrogenation Kinetics of Metal Hydrides. *Current Opinion in Solid State and Materials Science* **2011**, *15*, 52-61.

(19) Adelhelm, P.; De Jongh, P. E. The Impact of Carbon Materials on the Hydrogen Storage Properties of Light Metal Hydrides. *Journal of Materials Chemistry* **2011**, *21*, 2417-2427.

(20) Gupta, S.; Hlova, I. Z.; Kobayashi, T.; Denys, R. V.; Chen, F.; Zavaliy, I. Y.; Pruski, M.; Pecharsky, V. K. Facile Synthesis and Regeneration of $Mg(BH_4)_2$ by High Energy Reactive Ball Milling of MgB_2. *Chemical Communications* **2013**, *49*, 828-830.

(21) Pistidda, C.; Garroni, S.; Dolci, F.; Bardají, E. G.; Khandelwal, A.; Nolis, P.; Dornheim, M.; Gosalawit, R.; Jensen, T.; Cerenius, Y.; Suriñach, S.; Baró, M. D.; Lohstroh, W.; Fichtner, M. Synthesis of Amorphous $Mg(BH_4)_2$ from MgB_2 and H_2 at Room Temperature. *J. Alloys Compounds* **2010**, *508*, 212-215.

(22) Fichtner, M.; Zhao-Karger, Z.; Hu, J.; Roth, A.; Weidler, P. The Kinetic Properties of $Mg(BH_4)_2$ Infiltrated in Activated Carbon. *Nanotechnology* **2009**, *20*, 204029.

(23) Wahab, M. A.; Jia, Y.; Yang, D.; Zhao, H.; Yao, X. Enhanced Hydrogen Desorption from $Mg(BH_4)_2$ by Combining Nanoconfinement and a Ni Catalyst. *Journal of Materials Chemistry A* **2013**, *1*, 3471-3478.

(24) Remhof, A.; Borgschulte, A.; Friedrichs, O.; Mauron, P.; Yan, Y.; Züttel, A. Solvent-Free Synthesis and Decomposition of $Y(BH_4)_3$. *Scr. Mater.* **2012**, *66*, 280-283.

(25) Friedrichs, O.; Remhof, A.; Borgschulte, A.; Buchter, F.; Orimo, S. I.; Züttel, A. Breaking the Passivation - the Road to a Solvent Free Borohydride Synthesis. *Physical Chemistry Chemical Physics* **2010**, *12*, 10919-10922.

(26) Pekala, R. W. Organic Aerogels from the Polycondensation of Resorcinol with Formaldehyde. *J. Mater. Sci.* **1989**, *24*, 3221-3227.

(27) De Jongh, P. E.; Wagemans, R. W. P.; Eggenhuisen, T. M.; Dauvillier, B. S.; Radstake, P. B.; Meeldijk, J. D.; Geus, J. W.; De Jong, K. P. The Preparation of Carbon-Supported Magnesium Nanoparticles using Melt Infiltration. *Chemistry of Materials* **2007**, *19*, 6052-6057.

(28) Ravnsbaek, D.; Filinchuk, Y.; Cerenius, Y.; Jakobsen, H. J.; Besenbacher, F.; Skibsted, J.; Jensen, T. R. A Series of Mixed-Metal Borohydrides. *Angewandte Chemie - International Edition* **2009**, *48*, 6659-6663.

(29) Kissinger, H. E. Reaction Kinetics in Differential Thermal Analysis. *Anal. Chem.* **1957**, *29*, 1702-1706.

(30) Newhouse, R. J.; Stavila, V.; Hwang, S.; Klebanoff, L. E.; Zhang, J. Z. Reversibility and Improved Hydrogen Release of Magnesium Borohydride. *Journal of Physical Chemistry C* **2010**, *114*, 5224-5232.

(31) Gutowska, A.; Li, L.; Shin, Y.; Wang, C. M.; Li, X. S.; Linehan, J. C.; Smith, R. S.; Kay, B. D.; Schmid, B.; Shaw, W.; Gutowski, M.; Autrey, T. Nanoscaffold Mediates Hydrogen Release and the Reactivity of Ammonia Borane. *Angewandte Chemie - International Edition* **2005**, *44*, 3578-3582.

(32) Gross, A. F.; Vajo, J. J.; Van Atta, S. L.; Olson, G. L. Enhanced Hydrogen Storage Kinetics of $LiBH_4$ in Nanoporous Carbon Scaffolds. *Journal of Physical Chemistry C* **2008**, *112*, 5651-5657.

(33) Liu, Y.; Zhon, K.; Luo, K.; Gao, M.; Pan, H.; Wang, Q. Size-Dependent Kinetic Enhancement in Hydrogen Absorption and Desorption of the Li-Mg-N-H System. *J. Am. Chem. Soc.* **2009**, *131*, 1862-1870.

(34) Ngene, P.; Van Zwienen, R.; De Jongh, P. E. Reversibility of the Hydrogen Desorption from $LiBH_4$: A Synergetic Effect of Nanoconfinement and Ni Addition. *Chemical Communications* **2010**, *46*, 8201-8203.

(35) Mueller, T.; Ceder, G. Effect of Particle Size on Hydrogen Release from Sodium Alanate Nanoparticles. *ACS Nano* **2010**, *4*, 5647-5656.

(36) Liu, X.; Peaslee, D.; Jost, C. Z.; Baumann, T. F.; Majzoub, E. H. Systematic Pore-Size Effects of Nanoconfinement of $LiBH_4$: Elimination of Diborane Release and Tunable Behavior for Hydrogen Storage Applications. *Chemistry of Materials* **2011**, *23*, 1331-1336.

(37) Paskevicius, M.; Sheppard, D. A.; Buckley, C. E. Thermodynamic Changes in Mechanochemically Synthesized Magnesium Hydride Nanoparticles. *J. Am. Chem. Soc.* **2010**, *132*, 5077-5083.

5. Pore confined synthesis of magnesium boron hydride nanoparticles

Abstract

Nanostructured materials based on light elements such as Li, Mg and Na are essential for energy storage and conversion applications, but often difficult to prepare with control over size and structure. A new strategy which is illustrated by the formation of magnesium boron hydrides that is relevant for reversible solid state hydrogen storage is discussed. The reaction was carried out with small (5-10 nm) MgH_2 nanoparticles inside the ~10 nm pores of a carbon scaffold, and larger MgH_2 crystallites on the exterior surface of the scaffold. The large difference in reactivity between the two types of MgH_2 is used to selective react the small MgH_2 particles inside the pores with B_2H_6 to form magnesium boron hydrides under mild conditions. In this way pore-confined magnesium boron hydrides are formed with $MgB_{12}H_{12}$ as the major phase. Hydrogen release from the confined magnesium boron hydrides starts just above the synthesis temperature of 120 ^oC. The addition of Ni brings about the reaction to proceed readily at temperatures as low as 30 ^oC. Furthermore by Ni addition and tuning the synthesis temperature, the product distribution can be steered towards $Mg(BH_4)_2$ and other magnesium boron hydrides. This shows the suitability of this method to selectively form pore-confined complex metal hydrides, such as $MgB_{12}H_{12}$ for which no synthesis strategy had been reported until now. This strategy might also be relevant for other novel energy storage and conversion materials which are difficult to nanostructure in a controlled manner by conventional methods.

1. Introduction

The design and synthesis of novel nanomaterials is crucial to facilitate energy conversion and storage [1]. Nanomaterials can be applied in the field of photocatalytic hydrogen generation, solar cells, batteries and hydrogen storage [2-5]. Due to the small size the surface to volume ratio is large, leading to increased reactivity, lower melting point, change in phase transition temperatures, higher solubility and different electronic band structures changing the electric and optical properties compared to bulk materials [6]. However, in most processes the material has to be operated or cycled under dynamic conditions. During prolonged operation the structure of the nanomaterial is likely to change since particle growth is favorable as it lowers the surface energy [7]. Hence, a support or scaffold material is often employed to prevent particle growth.

Supported nanomaterials are important because of their unique functionality, but assembling them is often not straightforward. Two approaches can be used: deposition of preformed particles obtained for example via colloidal routes, which allows unique control over size and shape; or in-situ growth of the active phase in a host material leading to formation of nanoparticles [8]. Solution impregnation is often used: a precursor solution is added to a porous host, followed by drying and decomposition to obtain well-dispersed supported nanoparticles, usually metal oxides [9]. Metallic species are obtained by reduction of the metal oxides species at elevated temperatures. However, this method cannot always be applied. Not all compounds are sufficiently soluble in suitable solvents. As typically high temperatures are needed to remove the solvent and/or decompose precursors, potential issues include undesired reactions, the formation of stable adducts, and particle growth. Furthermore, the method cannot be applied for metallic species that are difficult to form by reduction from the oxides, such as alkaline or alkaline-earth metals. On the other hand since weight is often an important criterion, energy storage materials are often based on light elements such as Li, Mg, Al and Na [10, 11].

An alternative is deposition via a molten or gas phase. For instance, guest species are brought into close contact with the host material and heated above the melting temperature [12]. The liquid guest species are sucked into the pores, if wetting occurs. However, the method is not applicable whenever a compound or their precursor decomposes before the melting point is reached. Also, the wetting between the host and guest material must be favorable, meaning that the contact angle between the liquid and solid interface must be lower than 90^{o}. An alternative preparation

strategy is proposed, taking nanostructured magnesium borohydride as showcase, since this compound is difficult to prepare via any of the existing routes mentioned above.

Recently $Mg(BH_4)_2$ (14.9 wt% H_2) attracted much attention as a possible reversible hydrogen storage material [13]. The enthalpy change is -39 $kJ \cdot mol^{-1}$ H_2 for hydrogen release following (Eq. 5 - 1): [14]

$$Mg(BH_4)_2 \leftrightarrow MgB_2 + 4\ H_2 \qquad \text{(Eq. 5 - 1)}$$

However, dehydrogenation only starts above 250 ˚C due to kinetic barriers [15]. Several intermediates phases were observed during the decomposition of $Mg(BH_4)_2$ such as $Mg(B_3H_8)_2$ and $MgB_{12}H_{12}$ [16, 17]. Also, the reverse reaction to form $Mg(BH_4)_2$ is slow and requires high hydrogen pressures and high temperatures (e.g. 95 MPa H_2, 400 ^oC) [18].

Nanoconfinement has shown to have great benefits in hydrogen storage for other complex metal hydrides, such as enhancing the kinetics and reversibility of hydrogen sorption. Although $NaAlH_4$ and $LiBH_4$ can be prepared by melt infiltration [19-21], it is not possible for $Mg(BH_4)_2$, because decomposition occurs before melting. Nanoconfined $Mg(BH_4)_2$ prepared via solution impregnation with addition of Ni addition has been reported [22]. The peak temperature for hydrogen desorption was reduced to 155 ^oC, however, the difficulty of removing residual traces of solvent after impregnation remains and multiple impregnation steps are needed due to the low solubility of $Mg(BH_4)_2$ in diethyl ether [23].

This study discloses a novel synthesis route for nanoconfined complex hydrides. The strategy is to start with nanoconfined metal or metal hydride species that is more easily deposited and to take advantage of the high reactivity of the nanoparticles to convert them exclusively into nanoparticles of the desired complex metal hydride compounds via a solid-gas reaction. The method is demonstrated for synthesis of magnesium boron hydrides. After synthesis of nanoconfined MgH_2, the sample was treated in a B_2H_6/H_2 gas mixture at mild temperatures to add boron. This method also allows the addition of other metals as catalyst as is illustrated with the addition of Ni. Depending on the synthesis conditions, nanoconfined $Mg(BH_4)_2$, $MgB_{12}H_{12}$ and other magnesium boron hydride compounds with favorable hydrogen release properties was successfully obtained.

2. Experimental

2.1 Synthesis

Porous carbon was synthesized via resorcinol-formaldehyde condensation [24]. Resorcinol (Sigma Aldrich 99%, 8,65 g, 79 mmol), formaldehyde (Fisher chemical, analytical reagent 37-41%, stabilized by 12% methanol, 12.89 g, 158 mmol) and sodium carbonate (Across organics 99.5%, 0.017 g, 0.16 mmol) were dissolved in deionized water and the mixture was stirred until a homogeneous solution was obtained. The next step was to age the sample for 1 day at room temperature, 1 day at 60 ^{o}C and 3 days at 90 ^{o}C, followed by cooling, powdering and washing with acetone. After drying at room temperature, pyrolization was performed in a tubular oven at 800 ^{o}C for 10 hours in an Ar-flow resulting in the carbon support with an average pore diameter of ~9 nm with a pore volume of ~0.5 $cm^3 \cdot g^{-1}$.

Deposition of 10 wt% MgH_2 on carbon occurred via heat treatment of a mixture of the porous support and MgH_2 (Alfa Aesar 98%) above the melting temperature [25]. The sample was ground in a mortar to obtain a homogenous mixture and placed in a carbon crucible, which was sealed hermetically in a stainless steel vessel and brought into the tubular oven under Ar atmosphere. The sample was heated up to 658 ^{o}C with 10 $^{o}C \cdot min^{-1}$ and kept at this temperature for 24 min before cooling to room temperature. Rehydrogenation of the sample was performed in an autoclave (Parr) at 300 ^{o}C with 100 bar of H_2 pressure for 12 h. The hydrogenated sample was stored in an Ar-glovebox (MBraun Labmaster) and all further preparation steps and measurements were performed in inert atmosphere.

The Mg-Ni-H-C composition was prepared by first depositing Ni nanoparticles via incipient wetness impregnation with a nickel citrate solution as precursor. The nickel citrate solution (0.88 M) was created by dissolving nickel nitrate hexahydrate (Acros 99%, 5.3 mmol) and citric acid (Acros 99.5%, 3.5 mmol) in 10 ml of demineralized water. After injecting 0.5 ml of the solution dropwise to the carbon support (1.0 g) under Ar atmosphere, the sample was dried in vacuum for 6 hours at room temperature. The sample was decomposed and reduced in a tubular oven at 400 ^{o}C with a heating ramp of 5 $^{o}C \cdot min^{-1}$ and kept at 400 ^{o}C for 3 hours, while flowing a 20% H_2/Ar mixture flowing at 150 $ml \cdot min^{-1}$. Addition of Mg occurred via the same method as described previously. The composition containing 10 wt% Mg and 2 wt% Ni on carbon (Mg_{10}-Ni_2-H) was obtained after hydrogenation at 200 ^{o}C with 100 bar H_2 pressure for 12 h in an autoclave (Parr).

The diborane source was prepared from a ball milled mixture of $NaBH_4$ (Katchem, 95%) and $ZnCl_2$ (Sigma–Aldrich, 99.9%) as proposed by Ravnsbaek et al. that releases a B_2H_6/H_2 mixture with a 1 : 1 molar ratio at elevated temperatures [26].

MgH_2 and Mg_{10}-Ni_2-H supported on carbon were treated separately under ~10 bar static pressure of the generated B_2H_6/H_2 gas mixture at 30 °C, 60 °C and 120 °C for 3 days, which resulted in MgB_xH_x and MgB_xH_x-Ni composites supported on carbon. A batch of $Mg(BH_4)_2$ (Sigma Aldrich 95%) was dried at 150 °C for 3 h and was used as reference material. The obtained samples are and treatment conditions are summarized in Table 5 - 1.

Table 5 - 1: List of samples and treatment conditions.

Sample list	Treatment temperature	Comments
MgH_2/C	-	MgH_2 nanoparticles supported on carbon
MgH_2/C	120 °C	10 wt% MgH_2 on carbon treated in 10 bars of B_2H_6/H_2 at 120 °C for 3 days
Mg_{10}-Ni_2-H/C	-	10 wt% MgH_2 and 2 wt% Ni nanoparticles supported on carbon
Mg_{10}-Ni_2-H/C	30 °C	10 wt% MgH_2 and 2 wt% Ni on carbon treated in 10 bars of B_2H_6/H_2 at 30 °C for 3 days
Mg_{10}-Ni_2-H/C	60 °C	10 wt% MgH_2 and 2 wt% Ni on carbon treated in 10 bars of B_2H_6/H_2 at 60 °C for 3 days
Mg_{10}-Ni_2-H/C	120 °C	10 wt% MgH_2 and 2 wt% Ni on carbon treated in 10 bars of B_2H_6/H_2 at 120 °C for 3 days

2.2 Characterization

X-ray diffraction (XRD) was carried out using a Bruker D8 Advance diffractometer equipped with the VANTEC-1 detector and using $Cu_K\alpha_{1,2}$ radiation. All samples were prepared in the glovebox and measured in sealed glass capillaries (diameter, 0.7 mm; wall thickness, 0.01 mm). Each scan was performed from 20°-70° 2θ with a step size of 0.015° and an acquisition time of 7 s per step.

Pore volume analysis was performed with N_2-physisorption (Micromeritics TriStar 3000). The samples were loaded in a capped quartz tube in the glovebox and directly measured. The

mesopore size distribution was analyzed with the Barrett-Joyner-Halenda (BJH) method from the adsorption branch by using a carbon black equation as reference. The total pore volume was obtained at $p/p_0 = 0.997$.

Solid state ^{11}B magic angle spinning nuclear magnetic resonance (MAS NMR) was performed with a Bruker Avance-400 NMR spectrometer using a 4 mm CP-MAS probe. The ^{11}B NMR spectra were recorded at 128.38 MHz at 12 kHz sample rotation. A Hahn echo pulse sequence was used to suppress the broad background resonance of boron nitride from the probe. For the excitation, pulse lengths of 1.5 μs (π/12 pulse) were used and 3.0 μs echo pulses were applied. The ^{11}B chemical shifts are reported in parts per million (ppm) with respect to a 1M $B(OH)_3$ aqueous solution at 19.6 ppm as an external standard sample. Also, $Mg(BH_4)_2$ (Sigma Aldrich 95%) and $K_2B_{12}H_{12}$ (Katchem) were used as references for the identification of the $[BH_4]^-$ and $[B_{12}H_{12}]^{2-}$ signals.

Transmission electron microscopy (TEM) images were acquired with an FEI Tecnai 20F (equipped with a Field Emission Gun) and operated at 200 kV. A small amount of sample was placed on a 200 mesh Cu grid coated with a carbon polymer film in the glovebox and transferred into the microscope, where the sample was exposed to air for no more than 5 s. Simultaneously, energy-dispersive X-ray spectroscopy (EDX) was used for elemental analysis and electron energy loss spectroscopy **(**EELS) was used to detect the presence of B species.

Hydrogen desorption measurements were carried out with combined temperature programmed desorption (Micromeritics AutoChem II 2920 equipped with a TCD detector) and mass spectroscopy experiments (Pfeiffer Vacuum OmniStar^{TM}) (TPD-MS). Approximately 50 mg of each sample was put into quartz tubes in the glovebox and measured in an Ar-flow of 25 ml·min^{-1} with a heating ramp of 5 $^{o}C \cdot min^{-1}$ up to 600 ^{o}C as standard measurements. At the same time, the mass spectrometer recorded the masses of H_2 (m/z = 2) and B_2H_6 (m/z = 26) during the measurements.

3. Results and discussion

3.1 Structural properties of pore confined magnesium boron hydrides

The carbon support had an average pore diameter of 9 nm and a mesopore volume of 0.52 $cm^3 \cdot g^{-1}$. MgH_2 deposition onto the carbon support and subsequent reaction with B_2H_6/H_2 at 120 ^{o}C, resulted in a pore volume decrease to 0.40 $cm^3 \cdot g^{-1}$ (Fig. 5 - 1: left). For the Ni impregnated

sample, the pore volume had decreased to 0.32 $cm^3 \cdot g^{-1}$ after reacting with B_2H_6/H_2 (Fig. 5 - 1: right). The decrease in pore volume is in line with material partly filling the mesopores of the carbon support and reacting in each step to form different species (Table 5 - 2).

Bright field transmission electron microscopy (TEM) on the MgH_2/C sample treated at 120 °C under B_2H_6/H_2 pressure indeed showed particles as dark spots with an average size of 7 nm on the more diffuse greyish carbon support (Fig. 5 - 3(a)). The local presence of C, O and Mg was proven by EDX, and EELS measurements comprised a B signal at 188 eV (Fig. 5 - 3(b) and (c)). The O signal is most likely from oxides formed during the short exposure of the sample to air or from oxygen groups on the carbon support.

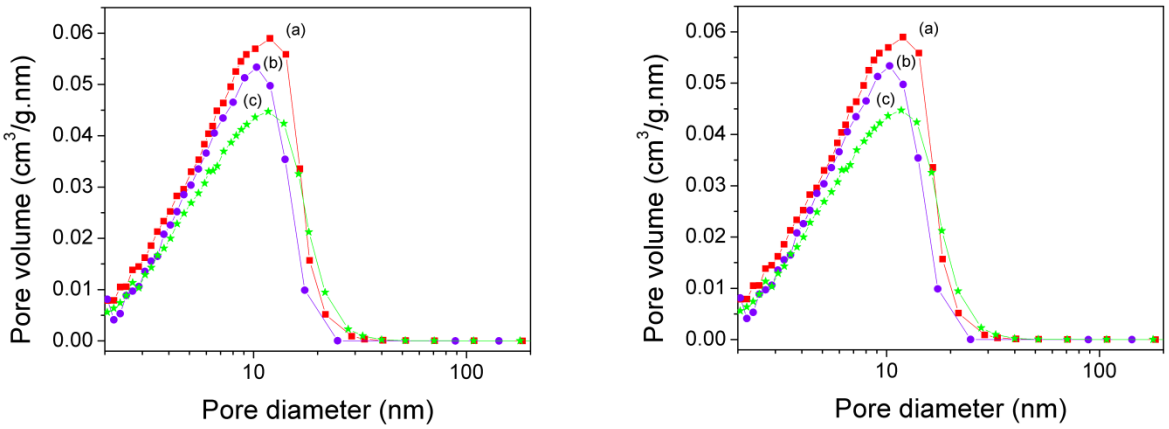

Fig. 5 - 1: Left: Pore size distribution of (a) the carbon support, (b) MgH_2 on carbon and (c) MgH_2 treated in B_2H_6/H_2 at 120 °C on carbon. Right: Pore size distribution of (a) the carbon support, (b) Ni on carbon, (c) Mg_{10}-Ni_2-H on carbon and (d) Mg_{10}-Ni_2-H treated in B_2H_6/H_2 at 120 °C on carbon.

Table 5 - 2: Calculated mesopore volumes from the pore size distributions of the samples as reported in Fig. 5 - 1.

Sample	Mesopore volume ($cm^3 \cdot g^{-1}$)
Carbon as synthesized	0.52
10 wt% MgH_2/C	0.48
10 wt% MgH_2/C 120 °C in B_2H_6/H_2	0.40
2 wt% Ni/C	0.46
Mg_{10}-Ni_2-H/C	0.38
Mg_{10}-Ni_2-H/C 120 °C in B_2H_6/H_2	0.32

When starting with Ni, nanoparticles with an average particle size of 6 nm were observed on the carbon support after impregnation and reduction (Fig. 5 - 2(a)). Mg-Ni containing species with an average size of 9 nm were formed after heat treating the Ni on carbon sample with Mg

and hydrogenation (Fig. 5 - 2(b)). After subsequent treatment of the sample at 60 °C under B_2H_6/H_2 pressure, small particles were observed as black dots in the TEM image (Fig. 5 - 3(d)) with an average size of 3 nm. When measuring EDX, the elements C, O, Mg and Ni were found (Fig. 5 - 3(e)). EELS revealed the presence of B (Fig. 5 - 3(f)). These results show that the elements Mg, Ni and B were successfully incorporated in the pores of the carbon scaffold as particles smaller than 10 nm.

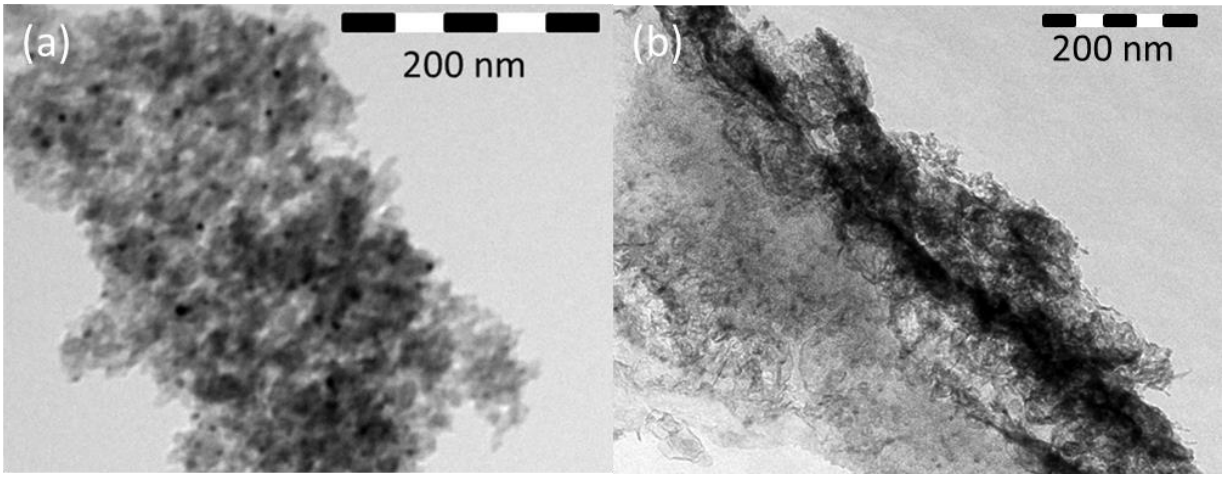

Fig. 5 - 2: Bright field TEM image of (a) 2 wt% Ni on carbon and (b) 10 wt% MgH_2 and 2 wt% Ni on carbon.

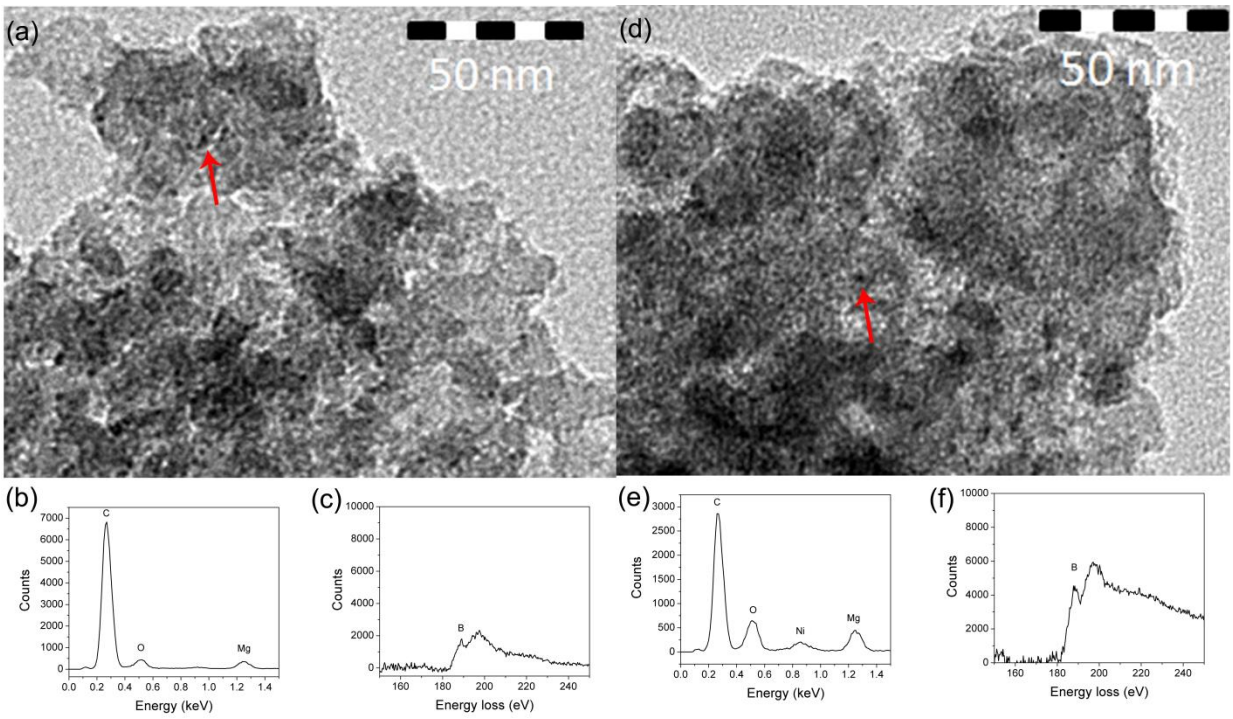

Fig. 5 - 3: Bright field TEM of (a) MgH_2/C treated in B_2H_6/H_2 at 120 °C with EDX (b) and EELS (c) measured on (a); and (d) TEM of Mg_{10}-Ni_2-H/C treated in B_2H_6/H_2 at 60 °C. EDX (e) and EELS (f) measured on (d).

3.2 Phase evolution upon treating nanoconfined MgH_2 with B_2H_6/H_2

Fig. 5 - 4(a) shows the X-ray pattern of MgH_2 deposited on carbon. The diffraction lines belong to Mg and MgH_2 crystallites. The observation of crystalline MgH_2 is in line with earlier findings: this preparation method typically results in approximately 30% of the added MgH_2 as nanoparticles in the pores of the scaffold, and the remainder crystallites are situated outside the pores of the carbon support [27]. After treatment with B_2H_6/H_2 at 120 °C, the diffraction pattern still shows diffraction lines belonging to crystalline Mg and MgH_2 (Fig. 5 - 4(b)). When compared to the diffraction pattern of the as-prepared state, the intensity of the MgH_2 diffraction lines had decreased slightly, which indicates that some reaction had taken place between B_2H_6 and MgH_2. However, new diffraction lines indicating the presence of a crystalline magnesium boron hydride compound did not appear. Apparently, if new phases have formed, they were non-crystalline and hence cannot be probed by X-ray diffraction. Therefore, solid-state nuclear magnetic resonance (NMR) was used to probe the presence of magnesium boron hydride species.

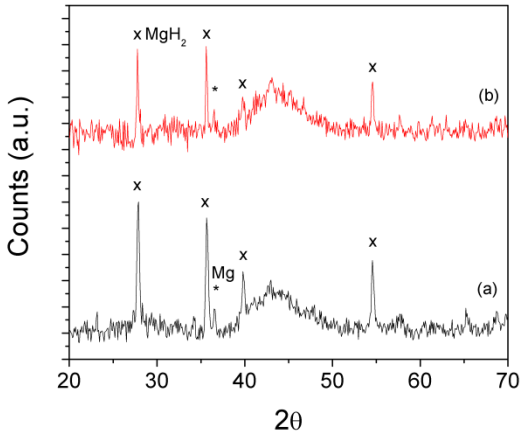

Fig. 5 - 4: XRD pattern of (a) MgH_2 on carbon and (b) MgH_2/C treated in B_2H_6/H_2 at 120 °C.

The ^{11}B NMR spectrum of the MgH_2/C sample treated at 120 °C in B_2H_6/H_2, shows a resonance around -16.0 ppm, which matches the chemical shift of $[B_{12}H_{12}]^{2-}$ (Fig. 5 - 5(a)). The peak has a shoulder, which indicates the possible presence of other closely related magnesium closoborane species such as $MgB_{11}H_{11}$ or MgB_9H_9. Also, a minor peak is observed at -40.8 ppm, which is at the same chemical shift as the $Mg(BH_4)_2$ reference. Hence, MgH_2 had reacted with B_2H_6/H_2 to form mainly $MgB_{12}H_{12}$ and a small amount of $Mg(BH_4)_2$.

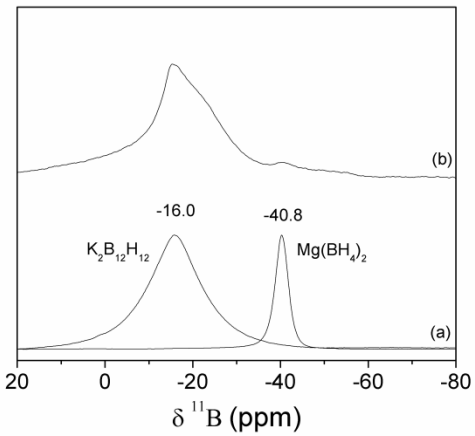

Fig. 5 - 5: ^{11}B MAS NMR spectra of (a) reference compounds $K_2B_{12}H_{12}$ (-16.0 ppm) and $Mg(BH_4)_2$ (-40.8 ppm). (b) MgH_2/C treated in B_2H_6/H_2 at 120 °C.

The hydrogen desorption profiles of the nanoconfined magnesium boron hydrides together with several MgH_2 reference compounds are shown in Fig. 5 - 6. The hydrogen desorption profile of the 37 μm MgH_2 powder (Fig. 5 - 6(a)) comprised a single desorption peak with a maximum temperature at 425 °C. MgH_2 deposited on the porous carbon support resulted in the desorption profile as shown in Fig. 5 - 6(b). Two peaks were found around 275 °C and 380 °C due to the presence of small confined nanoparticles and larger MgH_2 nanoparticles respectively, as was shown before [27, 28]. The hydrogen release kinetics of MgH_2 strongly depended on particle size and the amount of hydrogen release indicated that the sample consisted of approximately 20% nano-MgH_2 and 80% of larger crystalline MgH_2 particles.

For MgH_2/C heated at 120 °C with B_2H_6/H_2, hydrogen release started around 120 °C (Fig. 5 - 6(c)). The broad hydrogen release peaking around 210 °C is ascribed to the major phase present, mainly $MgB_{12}H_{12}$ with a possible contribution of other closely related closoboranes and the minor fraction of $Mg(BH_4)_2$. The amount of hydrogen released contributing from the broad peak with a peak around 210 °C (Fig. 5 - 6(c)) was increased after reacting with B_2H_6 compared to the first peak around 275 °C from the untreated MgH_2/C sample (Fig. 5 - 6(b)) and is due to the higher stoichiometric hydrogen content in MgB_xH_y. The sharp peak around 380 °C is assigned to residual MgH_2, which had not reacted with B_2H_6 as noted before based on XRD and NMR. Remarkable is the absence of the peak around 275 °C, which indicates that all the nanoconfined MgH_2 particles have reacted with B_2H_6. Also remarkable is that hydrogen is released at such low

temperatures from the nanoconfined magnesium boron hydride species. Non-confined $MgB_{12}H_{12}$ is known to decompose at significant higher temperatures [29-31].

To investigate whether or not the porous carbon support contributed to the gas release, the bare support was treated in B_2H_6/H_2 pressure at 120 °C. Afterwards, no signal indicating H_2 release was found in TPD and no significant amount of B_2H_6 release was found in MS (Fig. 5 - 6(d)). These results demonstrate that the reactivity of pore-confined MgH_2 particles allowed a selective reaction with gasses under mild conditions to form pore-confined complex metal hydride nanoparticles, while larger crystallites present on the exterior surface of the scaffold did not react under these conditions.

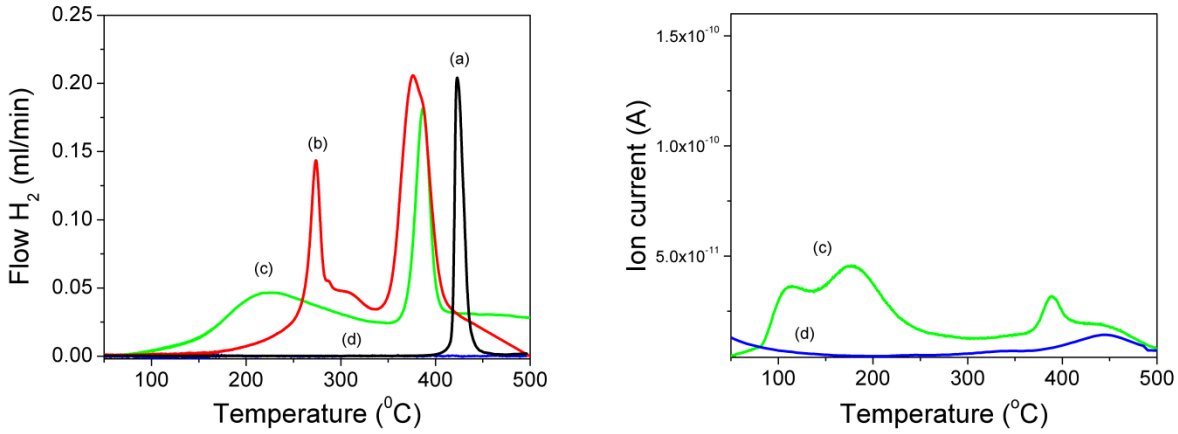

Fig. 5 - 6: Left: H_2 release of (a) MgH_2 powder (37 µm), (b) MgH_2 supported on carbon, (c) MgH_2/C treated in B_2H_6/H_2 at 120 °C and (d) the carbon support treated in B_2H_6/H_2 at 120 °C. Right: MS (m/z = 26) for B_2H_6 release measured simultaneously for (c) and (d). The heating rate was 5 °C·min^{-1}.

3.3 Phase evolution of nanoconfined MgH_2(Ni) upon treatment in B_2H_6/H_2

The hydrogenated Mg_{10}-Ni_2-H/C sample was characterized with XRD (Fig. 5 - 7(a)). Diffraction lines belonging to three different crystalline phases were found: MgH_2, Mg_2NiH_4 and traces of Mg. Upon treatment in 10 bars of B_2H_6/H_2 pressure at 30 °C (Fig. 5 - 7(b)), no significant change in the diffraction pattern occurred. Increasing the temperature to 60 °C resulted in a significant decrease in intensity of the MgH_2 and Mg_2NiH_4 diffraction lines, while the intensity of the Mg lines only decreased slightly (Fig. 5 - 7(c)). Interestingly, the diffraction lines of Mg_2NiH_4 had completely disappeared after treatment at 120 °C (Fig. 5 - 7(d)), while diffraction lines from crystalline Mg and MgH_2 were still present. No diffraction lines of a new crystalline phase were observed. Clearly, the addition of Ni made the sample more reactive towards B_2H_6 and the Mg-B-Ni-H phases formed were non-crystalline.

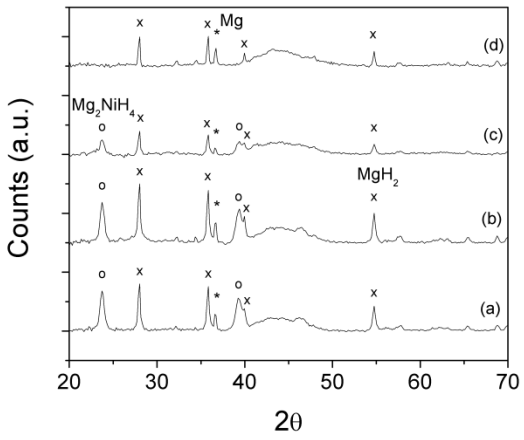

Fig. 5 - 7: XRD patterns (a) Mg_{10}-Ni_2-H on carbon, (b) Mg_{10}-Ni_2-H/C treated in B_2H_6/H_2 at 30 °C, (c) 60 °C and (d) 120 °C.

The ^{11}B NMR spectra of the Mg_{10}-Ni_2-H/C sample treated under B_2H_6/H_2 pressure at different temperatures are shown in Fig. 5 - 8. Please note that the presence of Ni in the sample can shield a part of the B-signal causing loss in sensitivity for the NMR measurements. The sample treated at 30 °C showed resonances with a clear peak at -17.8 ppm and a broad shoulder centered around -20.5 ppm, as well as a small peak near -57.0 ppm (Fig. 5 - 8(a)). Treating the sample at 60 °C slightly increased the intensity of the peaks at - 57.0 ppm and -16.0 ppm. This combination of peaks can probably be ascribed to magnesium boron hydride species in which the anion is not a closed cage (like $[B_{12}H_{12}]^{2-}$) but to a compound formed with a nidoborane that has more hydrogen anions, such as $Mg(B_5H_8)_2$, in which one of the boron atoms occupies a distinctly different position that the other four [32]. Remarkably, also a new resonance is observed at -40.8 ppm matching the $Mg(BH_4)_2$ reference. When the sample is treated at 120 °C, the main resonance is at – 16.0 ppm, matching the chemical shift $K_2B_{12}H_{12}$ and the signal at -57 ppm almost disappeared. Furthermore the peak at -40.8 ppm became even stronger (Fig. 5 - 8(c)). It is remarkable that the addition of nickel steered the reaction towards $Mg(BH_4)_2$ with increasing reaction temperature, while $MgB_{12}H_{12}$ was formed without the presence of nickel.

The hydrogen release was measured to further elucidate the phase evolution. A comparison was made between the hydrogen release before and after B_2H_6/H_2 treatment at different temperatures (Fig. 5 - 9). The $Mg(BH_4)_2$ powder reference showed 3 desorption peaks with maxima around 300 °C, 340 °C and 360 °C (Fig. 5 - 9(a)). This shows that multiple intermediate reaction steps were required for decomposition of $Mg(BH_4)_2$ in line with earlier reports [15, 18, 33,

[34]. The decomposition of all magnesium boron hydride species was accompanied by simultaneous release of B_2H_6 as observed with MS, but the amount is small compared to the release of H_2 (Fig. 5 - 9(a): right).

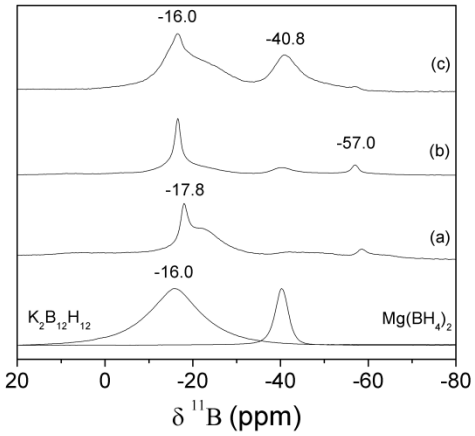

Fig. 5 - 8: ^{11}B MAS NMR spectra of Mg_{10}-Ni_2-H/C treated in B_2H_6/H_2 at (a) 30 °C, (b) 60 °C and (c) 120 °C. $K_2B_{12}H_{12}$ (-16.0 ppm) and $Mg(BH_4)_2$ (-40.8 ppm) are shown as reference compounds.

The hydrogen release profile of the hydrogenated Mg_{10}-Ni_2-H/C sample is shown in Fig. 5 - 9(b). Four peaks were observed with peak maxima at 190 ^oC, 210 ^oC, 280 ^oC and 380 ^oC, ascribed to Mg_2NiH_4 nanoparticles, crystalline Mg_2NiH_4; and nano-MgH_2 and crystalline MgH_2 particles respectively [28, 35, 36]. The different hydrogen release events are in line with the determination of multiple hydride phases with XRD (Fig. 5 - 7(a)) and the presence of different particle sizes found in TEM (Fig. 5 - 2(b)).

Fig. 5 - 9(c-e) shows the desorption profiles of Mg_{10}-Ni_2-H/C treated in B_2H_6/H_2 at different temperatures. After treatment at room temperature, the desorption profile started with a broad peak with a maximum at 170 ^oC, followed by 3 peaks in the temperature range of 250 ^oC to 350 ^oC with a last peak was found around 380 ^oC (Fig. 5 - 9(c)). The new peak with a maximum at 170 ^oC is most likely from a new magnesium boron hydride compound. The other peaks belong to residual crystalline MgH_2 and Mg_2NiH_4 as detected with XRD.

Heat treatment at 60 ^oC resulted in a more intense peak at 170 ^oC, indicating that more magnesium boron hydrides were formed (Fig. 5 - 9(d)). Also, the H_2 release peaks in the region between 250 ^oC to 350 ^oC had broadened. This is in line with the decrease in intensity of the diffraction lines in the X-ray pattern (Fig. 5 - 7(c)), which suggests that the amount of the crystalline Mg_2NiH_4 and MgH_2 phases was reduced. It shows that these phases are gradually

converted into a magnesium boron hydride phase as confirmed by the NMR measurement (Fig. 5 - 8(b)). Noteworthy is the low onset temperature of 75 °C for hydrogen release, as was also found for the compounds formed at 30 °C.

For the sample treated at 120 °C, the first peak is now at 230 °C instead of 170 °C. Also, the onset temperature has shifted to 120 °C (Fig. 5 - 9(e)), which is expected since other magnesium boron hydride species decomposing below the reaction temperature of 120 °C cannot exist. Furthermore, the features between 300-400 °C resemble those for decomposition of $Mg(BH_4)_2$ powder for both H_2 and B_2H_6 release as shown in the MS profile (Fig. 5 - 9(e)). The peak appearing at 440 °C is probably from decomposition of MgH_2. Noteworthy is that this sample combines complete disappearance of the Mg_2NiH_4 diffraction lines with the highest amount of $Mg(BH_4)_2$ formed as was determined by NMR Fig. 5 - 8(c)).

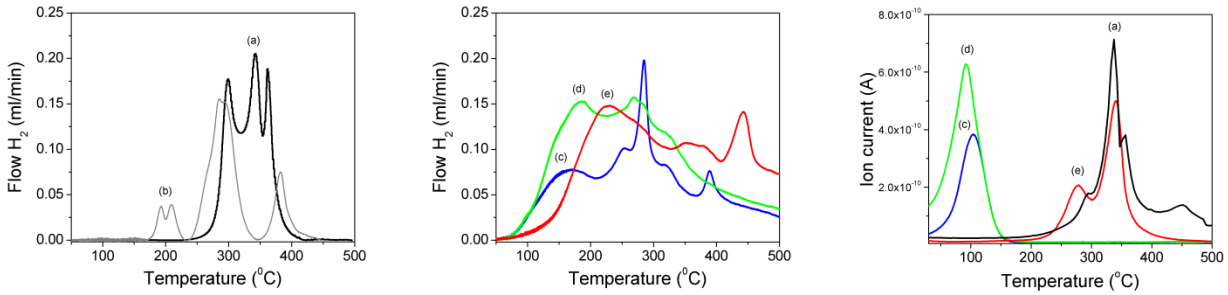

Fig. 5 - 9: H_2 release of (a) the $Mg(BH_4)_2$ reference, (b) Mg_{10}-Ni_2-H on carbon, (c) Mg_{10}-Ni_2-H/C treated in B_2H_6/H_2 at 30 °C, (d) 60 °C and (e) 120 °C. The right frame shows the MS spectra (m/z = 26) for B_2H_6 release simultaneously measured for (a, c-e). The heating rate was 5 °C·min^{-1}.

3.4 Tuning the reaction pathway

Fig. 5 - 10 summarizes the possibilities for the pore-confined reactions taking place between Mg(Ni) and B_2H_6 forming magnesium boron hydrides. As illustrated in the upper route, nanoconfined MgH_2 particles in a carbon scaffold fully react with B_2H_6 at 120 °C to form nanoconfined magnesium boron hydrides, with $MgB_{12}H_{12}$ identified as the major phase. Measuring the hydrogen release profile is in this case an important characterization method, and did not show any trace of the original pore-confined MgH_2 nanoparticles. At the same time MgH_2 crystallites present on the outside of the porous carbon particles hardly react, in line with earlier reports on a large difference in reactivity for pore-confined non-crystalline MgH_2 and larger MgH_2 crystallites [27].

It is generally very difficult to produce nanostructured light metal hydrides with controlled particle size and uniformity. For instance for nanostructuring by ball-milling a large heterogeneity in these parameters is found, while for pore confined materials it has proven difficult to selectively only obtain the active phase inside nanopores [30]. Furthermore synthesis often involves the use of solvents, which are difficult to remove without treatment at elevated temperatures, which could lead to undesired reactions. Hence a first important point is that, even though starting from MgH_2 on carbon that is rather heterogeneous, and contains both small MgH_2 particles inside the nanopores as well as larger crystallites on the outside of the support particles, after reaction with the gaseous B_2H_6 resulting magnesium boron hydrides are selectively formed inside the nanopores.

A second important point to note is that this is a new method for solvent free synthesis of $MgB_{12}H_{12}$, a compound that has been reported before but rather as an intermediate in the decomposition of other boron hydrides [17, 29]. This offers the possibility to produce this compound and study the structural, thermodynamic and hydrogen sorption properties in more detail.

With the addition of a second metal, Ni, it becomes clear that it is possible to some extent to steer the rate and the products of this pore-confined reaction. The reaction with B_2H_6 now even occurs at 30 ^oC. At low temperatures different magnesium boron hydrides can be formed, while at 120 ^oC the reaction product is mainly $MgB_{12}H_{12}$, but also comprises a significant amount of $Mg(BH_4)_2$. It is not trivial to explain the exact role of the Ni in this case, as it can influence the reaction in several ways. First of all metallic Ni surfaces are known to be excellent catalysts, for instance for hydrogenation reactions. The addition of Ni has been reported to lead to a large increase in reversibility for the hydrogen cycling of complex metal hydrides like $LiBH_4$ [20]. The ability of Ni to form a variety of Ni_xB compounds might also play an important role, as it can act as a site to "store B reversibly" facilitating the reaction [37]. On the other hand, the presence of Mg_2NiH_4 might facilitate the formation of $Mg(BH_4)_2$. The present study does not suffice to distinguish between the different possible roles. However, the fact that the presence of Ni (and hence probably also other metals like Co and Fe) steers the selectivity of the reaction from $MgB_{12}H_{12}$ in the direction of $Mg(BH_4)_2$ is highly interesting. It raises the expectation that further exploration of the reaction conditions and metal additives might yield solvent-free strategies to selectively produce different boron hydride phases.

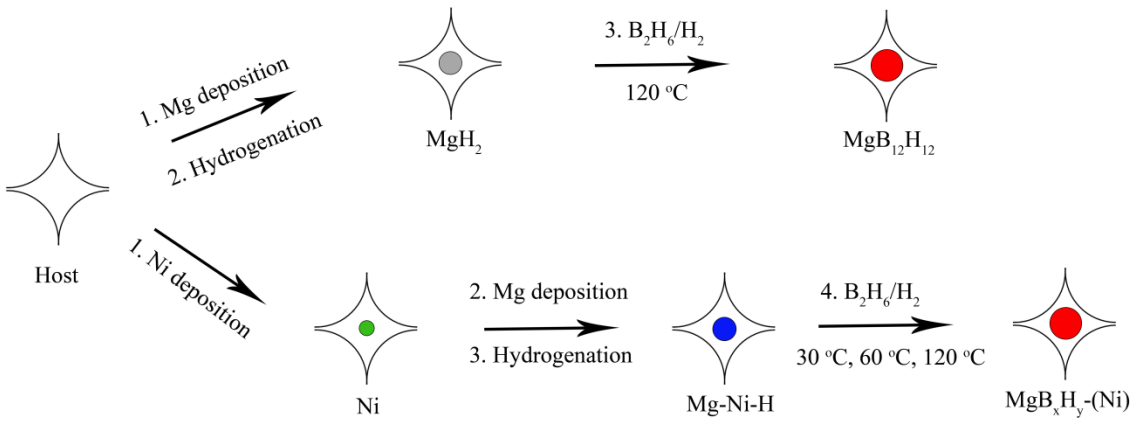

Fig. 5 - 10: Schematic overview of the synthesis strategy of the magnesium boron hydride compounds inside a porous host. In the upper route MgH_2 is treated under B_2H_6/H_2 pressure to form mainly $MgB_{12}H_{12}$. The lower route illustrates that with the addition of Ni mixtures of magnesium boron hydrides can be obtained, also comprising $Mg(BH_4)_2$.

4. Conclusions

Starting from supported MgH_2 nanoparticles, reaction with B_2H_6 leads to the formation of $MgB_{12}H_{12}$ selectively inside the pores of a carbon scaffold. Hydrogen release started at the preparation temperature of the sample (120 ^{o}C). The kinetics of the reaction were influenced by the addition of Ni, which led to fast reaction even at 30 ^{o}C. A shift in the product composition from other magnesium boron hydrides at low temperatures to $Mg(BH_4)_2$ at 120 ^{o}C was obtained. Pore-confined magnesium boron hydrides are relevant compounds, for instance for reversible hydrogen storage. But more importantly, it is possible to use the high reactivity of nanoparticles to selectively perform solid-gas reactions inside nanopores and produce a range of pore-confined magnesium boron hydrides via a solvent-free reaction. Energy storage and conversion often relies on light materials, which should be nanosized to obtain fast conversions but on the other hand stable under dynamic conditions, for instance by anchoring them on a support. This strategy might hence also be relevant to produce other novel energy storage and conversion materials based on light elements which are difficult to nanostructure in a controlled manner by conventional methods.

Acknowledgements

R. van den Berg and J. D. Meeldijk are acknowledged for the TEM measurements. D. Rentsch is acknowledged for performing the NMR measurements.

References

(1) Chen, X.; Li, C.; Grätzel, M.; Kostecki, R.; Mao, S. S. Nanomaterials for Renewable Energy Production and Storage. *Chem. Soc. Rev.* **2012**, *41*, 7909-7937.

(2) Chen, X.; Shen, S.; Guo, L.; Mao, S. S. Semiconductor-Based Photocatalytic Hydrogen Generation. *Chem. Rev.* **2010**, *110*, 6503-6570.

(3) Kamat, P. V. Meeting the Clean Energy Demand: Nanostructure Architectures for Solar Energy Conversion. *Journal of Physical Chemistry C* **2007**, *111*, 2834-2860.

(4) Aricò, A. S.; Bruce, P.; Scrosati, B.; Tarascon, J. M.; Van Schalkwijk, W. Nanostructured Materials for Advanced Energy Conversion and Storage Devices. *Nature Materials* **2005**, *4*, 366-377.

(5) Nielsen, T. K.; Besenbacher, F.; Jensen, T. R. Nanoconfined Hydrides for Energy Storage. *Nanoscale* **2011**, *3*, 2086-2098.

(6) Alivisatos, A. P. Perspectives on the Physical Chemistry of Semiconductor Nanocrystals. *The Journal of Physical Chemistry* **1996**, *100*, 13226-13239.

(7) Challa, S. R.; Delariva, A. T.; Hansen, T. W.; Helveg, S.; Sehested, J.; Hansen, P. L.; Garzon, F.; Datye, A. K. Relating Rates of Catalyst Sintering to the Disappearance of Individual Nanoparticles during Ostwald Ripening. *J. Am. Chem. Soc.* **2011**, *133*, 20672-20675.

(8) Jeon, K. J.; Moon, H. R.; Ruminski, A. M.; Jiang, B.; Kisielowski, C.; Bardhan, R.; Urban, J. J. Air-Stable Magnesium Nanocomposites Provide Rapid and High-Capacity Hydrogen Storage without using Heavy-Metal Catalysts. *Nature Materials* **2011**, *10*, 286-290.

(9) Eggenhuisen, T. M.; Friedrich, H.; Nudelman, F.; Zecevic, J.; Sommerdijk, N. A. J. M.; De Jongh, P. E.; De Jong, K. P. Controlling the Distribution of Supported Nanoparticles by Aqueous Synthesis. *Chemistry of Materials* **2013**, *25*, 890-896.

(10) Felderhoff, M.; Bogdanovic, B. High Temperature Metal Hydrides as Heat Storage Materials for Solar and Related Applications. *International Journal of Molecular Sciences* **2009**, *10*, 335-344.

(11) Schüth, F.; Bogdanovic, B.; Felderhoff, M. Light Metal Hydrides and Complex Hydrides for Hydrogen Storage. *Chemical Communications* **2004**, , 2249-2258.

(12) Gross, A. F.; Vajo, J. J.; Van Atta, S. L.; Olson, G. L. Enhanced Hydrogen Storage Kinetics of LiBH4 in Nanoporous Carbon Scaffolds. *Journal of Physical Chemistry C* **2008**, *112*, 5651-5657.

(13) Matsunaga, T.; Buchter, F.; Miwa, K.; Towata, S.; Orimo, S.; Züttel, A. Magnesium Borohydride: A New Hydrogen Storage Material. *Renewable Energy* **2008**, *33*, 193-196.

(14) Chlopek, K.; Frommen, C.; Léon, A.; Zabara, O.; Fichtner, M. Synthesis and Properties of Magnesium Tetrahydroborate, $Mg(BH_4)_2$. *Journal of Materials Chemistry* **2007**, *17*, 3496-3503.

(15) Hanada, N.; Chlopek, K.; Frommen, C.; Lohstroh, W.; Fichtner, M. Thermal Decomposition of $Mg(BH_4)_2$ Under He Flow and H_2 Pressure. *Journal of Materials Chemistry* **2008**, *18*, 2611-2614.

(16) Chong, M.; Karkamkar, A.; Autrey, T.; Orimo, S.; Jalisatgi, S.; Jensen, C. M. Reversible Dehydrogenation of Magnesium Borohydride to Magnesium Triborane in the Solid State Under Moderate Conditions. *Chemical Communications* **2011**, *47*, 1330-1332.

(17) Hwang, S. J.; Bowman Jr., R. C.; Reiter, J. W.; Rijssenbeek, J.; Soloveichik, G. L.; Zhao, J. C.; Kabbour, H.; Ahn, C. C. NMR Confirmation for Formation of $[B_{12}H_{12}]^{2-}$ Complexes during Hydrogen Desorption from Metal Borohydrides. *Journal of Physical Chemistry C* **2008**, *112*, 3164-3169.

(18) Severa, G.; Rönnebro, E.; Jensen, C. M. Direct Hydrogenation of Magnesium Boride to Magnesium Borohydride: Demonstration of >11 Weight Percent Reversible Hydrogen Storage. *Chemical Communications* **2010**, *46*, 421-423.

(19) Gao, J.; Adelhelm, P.; Verkuijlen, M. H. W.; Rongeat, C.; Herrich, M.; Van Bentum, P. J. M.; Gutfleisch, O.; Kentgens, A. P. M.; De Jong, K. P.; De Jongh, P. E. Confinement of $NaAlH_4$ in Nanoporous Carbon: Impact on H_2 Release, Reversibility, and Thermodynamics. *Journal of Physical Chemistry C* **2010**, *114*, 4675-4682.

(20) Ngene, P.; Van Zwienen, R.; De Jongh, P. E. Reversibility of the Hydrogen Desorption from $LiBH_4$: A Synergetic Effect of Nanoconfinement and Ni Addition. *Chemical Communications* **2010**, *46*, 8201-8203.

(21) Ngene, P.; Van Den Berg, R.; Verkuijlen, M. H. W.; De Jong, K. P.; De Jongh, P. E. Reversibility of the Hydrogen Desorption from $NaBH_4$ by Confinement in Nanoporous Carbon. *Energy and Environmental Science* **2011**, *4*, 4108-4115.

(22) Wahab, M. A.; Jia, Y.; Yang, D.; Zhao, H.; Yao, X. Enhanced Hydrogen Desorption from $Mg(BH_4)_2$ by Combining Nanoconfinement and a Ni Catalyst. *Journal of Materials Chemistry A* **2013**, *1*, 3471-3478.

(23) Fichtner, M.; Zhao-Karger, Z.; Hu, J.; Roth, A.; Weidler, P. The Kinetic Properties of $Mg(BH_4)_2$ Infiltrated in Activated Carbon. *Nanotechnology* **2009**, *20*, 204029.

(24) Pekala, R. W. Organic Aerogels from the Polycondensation of Resorcinol with Formaldehyde. *J. Mater. Sci.* **1989**, *24*, 3221-3227.

(25) De Jongh, P. E.; Wagemans, R. W. P.; Eggenhuisen, T. M.; Dauvillier, B. S.; Radstake, P. B.; Meeldijk, J. D.; Geus, J. W.; De Jong, K. P. The Preparation of Carbon-Supported Magnesium Nanoparticles using Melt Infiltration. *Chemistry of Materials* **2007**, *19*, 6052-6057.

(26) Ravnsbaek, D.; Filinchuk, Y.; Cerenius, Y.; Jakobsen, H. J.; Besenbacher, F.; Skibsted, J.; Jensen, T. R. A Series of Mixed-Metal Borohydrides. *Angewandte Chemie - International Edition* **2009**, *48*, 6659-6663.

(27) Au, Y. S.; Klein Obbink, M.; Srinivasan, S.; Magusin, P. C. M. M.; De Jong, K. P.; De Jongh, P. E. *Advanced Functional Materials* **2014**, *accepted*.

(28) Zlotea, C.; Chevalier-César, C.; Léonel, E.; Leroy, E.; Cuevas, F.; Dibandjo, P.; Vix-Guterl, C.; Martens, T.; Latroche, M. Synthesis of Small Metallic Mg-Based Nanoparticles Confined in Porous Carbon Materials for Hydrogen Sorption. *Faraday Discuss.* **2011**, *151*, 117-131.

(29) Chong, M.; Karkamkar, A.; Autrey, T.; Orimo, S.; Jalisatgi, S.; Jensen, C. M. Reversible Dehydrogenation of Magnesium Borohydride to Magnesium Triborane in the Solid State Under Moderate Conditions. *Chemical Communications* **2011**, *47*, 1330-1332.

(30) Yan, Y.; Au, Y. S.; Rentsch, D.; Remhof, A.; de Jongh, P. E.; Zuttel, A. Reversible Hydrogen Storage in $Mg(BH_4)_2$/carbon Nanocomposites. *J. Mater. Chem. A* **2013**, *37*, 11177.

(31) Zhang, Y.; Majzoub, E.; Ozolinš, V.; Wolverton, C. Theoretical Prediction of Metastable Intermediates in the Decomposition of $Mg(BH_4)_2$. *Journal of Physical Chemistry C* **2012**, *116*, 10522-10528.

(32) Hermánek, S. 11B NMR Spectra of Boranes, Main-Group Heteroboranes, and Substituted Derivatives. Factors Influencing Chemical Shifts of Skeletal Atoms. *Chem. Rev.* **1992**, *92*, 325-362.

(33) David, W. I. F.; Callear, S. K.; Jones, M. O.; Aeberhard, P. C.; Culligan, S. D.; Pohl, A. H.; Johnson, S. R.; Ryan, K. R.; Parker, J. E.; Edwards, P. P.; Nuttall, C. J.; Amieiro-Fonseca, A. The Structure, Thermal Properties and Phase Transformations of the Cubic Polymorph of Magnesium Tetrahydroborate. *Physical Chemistry Chemical Physics* **2012**, *14*, 11800-11807.

(34) Soloveichik, G. L.; Gao, Y.; Rijssenbeek, J.; Andrus, M.; Kniajanski, S.; Bowman Jr., R. C.; Hwang, S. -.; Zhao, J. -. Magnesium Borohydride as a Hydrogen Storage Material: Properties and Dehydrogenation Pathway of Unsolvated $Mg(BH_4)_2$. *Int J Hydrogen Energy* **2009**, *34*, 916-928.

(35) Bogerd, R.; Adelhelm, P.; Meeldijk, J. H.; De Jong, K. P.; De Jongh, P. E. The Structural Characterization and H_2 Sorption Properties of Carbon-Supported $Mg_{1-x}Ni_x$ Nanocrystallites. *Nanotechnology* **2009**, *20*, 204019.

(36) Zlotea, C.; Cuevas, F.; Andrieux, J.; Matei Ghimbeu, C.; Leroy, E.; Léonel, E.; Sengmany, S.; Vix-Guterl, C.; Gadiou, R.; Martens, T.; Latroche, M. Tunable Synthesis of (Mg-Ni)-Based Hydrides Nanoconfined in Templated Carbon Studied by in Situ Synchrotron Diffraction. *Nano Energy* **2013**, *2*, 12-20.

(37) Ngene, P.; Verkuijlen, M. H. W.; Zheng, Q.; Kragten, J.; Van Bentum, P. J. M.; Bitter, J. H.; De Jongh, P. E. The Role of Ni in Increasing the Reversibility of the Hydrogen Release from Nanoconfined $LiBH_4$. *Faraday Discuss.* **2011**, *151*, 47-58.

6. Summary, concluding remarks and outlook

6.1 Summary

The increasing CO_2 content in the atmosphere due to combustion of fossil fuels is the main cause of enhanced "global warming". Switching to renewable energy sources, such as solar or wind energy is promising for a sustainable future, but the produced electricity cannot be used easily for off-grid applications. Fuels are still required for mobile applications and can be produced for instance by electrolysis using the electricity from renewable energy sources. Hydrogen is promising in this context to be used as fuel in the future. A possible scenario is to store the hydrogen and regain the energy either by combustion or by using fuel cells. However, a suitable storage method has not yet been realized. Storage of hydrogen as atoms or ions in solid materials is interesting, because the volume is greatly reduced and it is generally safer than storage as compressed gas.

Unfortunately, several drawbacks have to be overcome before solid-state hydrogen storage can be implemented. Although storage in solid materials is more compact than storage as a gas, the gravimetric density is quite low. This is less critical if the hydrogen is used for stationary applications. Compared to Li-batteries being applied in for instance vehicles, solid hydrogen storage materials are competitive in terms of gravimetric energy density. The operation conditions for solid-state hydrogen storage materials are determined by the equilibrium and kinetic characteristics of hydrogen sorption. Due to the strong bond between the hydrogen and the storage material, high operation pressures and temperatures are often required for the charging and discharging processes. Also cycling stability is an important material property.

This thesis discusses several methods to improve the hydrogen storage properties of Mg-based materials. Magnesium based materials are interesting due to the abundance and low costs of magnesium (~ 3 €/kg in 2013). However, the equilibrium temperature for hydrogen sorption in $Mg(H_2)$ is 300 ^oC at 1 bar H_2 and both hydrogen absorption and desorption are slow at room temperature. In order to change the thermodynamic and kinetic properties, other elements were added to Mg either as catalyst or to form different Mg-compounds. One of the main challenges

was to find new synthesis strategies to produce materials with particle sizes in the nanometer range. Small particle sizes are crucial to improve the kinetic properties and reversibility. A main synthesis technique to obtain nanoparticles involved using porous carbon supports in order to control the particle size. The use of a support also prevented particle growth. An important aim of the study was to relate structural properties of the carbon supported Mg-based nanomaterials to the hydrogen storage performance in order to understand the impact of particle size, composition and interaction with the carbon support.

In **Chapter 2**, the use of carbon aerogel supports with different pore sizes to obtain different $Mg(H_2)$ particle sizes is discussed, as well as the influence of particle size on the kinetics of hydrogen release and uptake. Deposition of Mg was performed via heat treatment of a mixture of the porous carbon support and MgH_2 above the melting temperature of Mg (650 ^oC). This resulted in Mg in the pores of the carbon support with average nanoparticle sizes of 6.3 nm, 7.9 nm, 9.8 nm and 14 nm on carbon supports with average pore diameters of 6 nm, 9 nm 12 nm and 20 nm respectively. Hydrogen desorption measurements for carbon supported MgH_2 clearly showed two distinct hydrogen release events, which are ascribed to nano-MgH_2 in the pores and MgH_2 particles on the exterior surface of the carbon support. For nano-MgH_2, a gradual increase in the peak temperatures for hydrogen release was observed with increasing particle sizes. The difference in kinetic behavior of the hydrogen desorption reaction for crystalline and nanosized MgH_2 was further investigated with ^1H NMR, which showed a higher intrinsic mobility for the H-atoms in nano-MgH_2 compared to crystalline MgH_2. Moreover, hydrogen was reabsorbed up to 80% of the storage capacity of the nanoparticles within 15 min at 300 ^oC and 18 bar H_2; and the hydrogen sorption of the $Mg(H_2)$ nanoparticles remained reversible for several cycles without significant deterioration of the kinetic performance. Hence, the use of porous carbon aerogel supports successfully prevented particle growth and was able to control the particle size of $Mg(H_2)$ leading to faster hydrogen sorption kinetics.

Chapter 3 explains a new method to synthesize Mg-Cu alloys nanoparticles supported on carbon. The nanocomposites were able to store hydrogen reversibly and with a lower decomposition enthalpy (66 $kJ \cdot mol^{-1}$ H_2) than for the MgH_2 system (75 $kJ \cdot mol^{-1}$ H_2), resulting in a lower equilibrium temperature for hydrogen release. Synthesis occurred via impregnation of porous and non-porous graphite supports with a $Cu(NO_3)_2.3H_2O$ solution. Metallic Cu nanoparticles were obtained after decomposition of the precursor and direct reduction in a H_2

flow. Addition of Mg was performed by mixing the carbon supported Cu nanoparticles with MgH_2 powder and heating above the melting temperature of Mg (650 ^oC). The smallest Mg-Cu alloy particles with an average size of 20 nm were obtained on porous graphite. Mg-Cu nanoparticles smaller than 300 nm were not observed on non-porous graphite due to the large initial size of the Cu particles. This demonstrates that the use of a porous scaffold with a high surface area is crucial to synthesize nanostructured materials by allowing better distribution of the particles and possibly trap the nanoparticles in the porous structure. Hydrogen release for the 20 nm particles occurred around 250 ^oC compared to 400 ^oC for micrometer sized Mg-Cu powder. An intermediate hydrogen release temperature of 350 ^oC was found for 300 nm particles. This is also reflected in the activation energies for hydrogen release ranging from 128 (± 6) $kJ \cdot mol^{-1}$ for micrometer particles to 102 (± 7) $kJ \cdot mol^{-1}$ for 300 nm and 97 (± 9) $kJ \cdot mol^{-1}$ for 20 nm particles. When the particle size is decreased, not only the diffusion path length is shorter, but most likely increased the atomic diffusion coefficient as well for transformation of the Mg_2Cu alloy into $MgCu_2$ and vice versa, which is essential during the hydrogen sorption reaction. The system was reversible over several cycles with only minor capacity loss after the first cycle.

$Mg(BH_4)_2$ is a promising Mg-based hydrogen storage material due to its high gravimetric capacity of 14.9 wt% H_2 and an even lower decomposition enthalpy than the previous materials, namely 39 $kJ \cdot mol^{-1}$ H_2. However, hydrogen desorption occurs in multiple steps and dehydrogenation requires harsh conditions. Nanosizing $Mg(BH_4)_2$ might lead to a change in the decomposition and rehydrogenation pathways and kinetics. Moreover an improvement in the kinetics is expected. **Chapter 4** deals with a novel method for synthesis of nanostructured magnesium boron hydrides. The synthesis started from supported MgH_2 nanoparticles on different carbon supports followed by ball milling under B_2H_6/H_2 pressure at room temperature. This resulted in the formation of amorphous $Mg(BH_4)_2$ and $MgB_{12}H_{12}$ as determined by solid-state ^{11}B NMR. Hydrogen release started at 100 ^oC for the newly synthesized magnesium boron hydride compounds compared to 250 ^oC for bulk $Mg(BH_4)_2$. The nanocomposite was partially rehydrogenated to $Mg(BH_4)_2$ under relative mild conditions (270 ^oC, 150 bar H_2 compared to 400 ^oC, 950 bar H_2 for bulk), but $MgB_{12}H_{12}$ was mainly formed.

Unfortunately, the ball milling process destroyed the structure of the carbon scaffold. Therefore, another method was explored to synthesize pore-confined magnesium boron hydride

keeping the carbon scaffold intact, which is described in **chapter 5**. The idea is to take advantage of the high reactivity of (supported) MgH_2 nanoparticles. Supported MgH_2 nanoparticles on porous carbon with and without Ni were treated at different temperatures under B_2H_6/H_2 pressure. The reaction resulted in the formation of different magnesium boron hydrides. Treatment of the MgH_2 nanoparticles at 120 ^oC mainly resulted in $MgB_{12}H_{12}$ and traces of $Mg(BH_4)_2$ as well as other magnesium boron hydrides as determined by solid-state ^{11}B NMR. XRD and hydrogen release measurements showed that all MgH_2 nanoparticles reacted, while bulk MgH_2 remained present in the sample. Addition of Ni changed the reactivity of the samples, resulting in reaction at room temperature and different magnesium boron hydride compounds. Increasing the temperature to 60 ^oC and 120 ^oC led to formation of a significant amount of $Mg(BH_4)_2$, but also $MgB_{12}H_{12}$ was formed. When Ni was present, the conversion of both crystalline Mg_2NiH_4 and MgH_2 was observed. Treatment of Ni catalyzed MgH_2 at 60 ^oC resulted in the highest amount of hydrogen released from magnesium boron hydrides that occurred at 170 ^oC instead of 300 ^oC for bulk $Mg(BH_4)_2$.

6.2 Concluding remarks and outlook

The synthesis of nanoparticles is a main topic in this thesis, because nanosizing is an effective tool to improve the kinetics for hydrogen absorption and desorption in metal hydride systems. It is known that the specific surface area is enhanced and the diffusion distances for atoms are shortened for nanoparticles. This was for instance demonstrated for the Mg-Cu system discussed in chapter 3. Also, it has been shown that the nucleation and growth processes in nanomaterials are faster due to the higher accessibility of nucleation sites and reduced distances for growth of the metal(hydride) phase. However, the impact of nanosizing on the kinetics are still far from understood. ^1H solid-state NMR on MgH_2 as described chapter 2 showed for the first time orders of magnitude faster dynamics of H-atoms in nano-MgH_2 than for H-atoms in crystalline MgH_2. This was determined from MgH_2 nanoparticles with different size ranges, prepared by deposition of Mg in a carbon scaffold with defined pore diameters. Further characterization on this type of samples with other advanced techniques can lead to new insights on the properties of nanomaterials.

Using a carbon support is essential to facilitate and stabilize small hydride nanoparticles for practical applications, but a drawback is the extra weight introduced by addition of the inert

support. Therefore, achieving high loadings of nanosized MgH_2 is an important challenge. Heat treatment of the support with Mg above the melting temperature to synthesize carbon supported $Mg(H_2)$ nanoparticles is a scalable technique. While postulated earlier that this process occurs via melt infiltration of liquid Mg, it has been speculated that the formation of supported nano-Mg particles also can occur via gas phase deposition. A closer investigation on the deposition mechanism will be helpful to understand whether and how the loading of nanoparticles can be increased.

The choice for the preferred Mg-based material to be used in practical applications depends on the desired operation conditions. In large scale industrial processes performing mainly exothermic reactions, an excess of heat might be available to release the stored hydrogen from the material. The preferred material could be $Mg(H_2)$, which has a large decomposition enthalpy but a high cycling stability. However catalysts are most likely required to increase the reaction rates. For processes where less excess heat is available and weight is less critical, the $Mg_2Cu(H)$ system can be considered, which has a lower hydrogen sorption enthalpy.

$Mg(BH_4)_2$ is an interesting hydrogen storage compound due to its high gravimetric capacity and low decomposition enthalpy. However, reversibility remains an issue even after nanosizing. It could be interesting to investigate the cyclability of partially decomposed $Mg(BH_4)_2$, involving intermediate compounds rather than the final product MgB_2. Since $MgB_{12}H_{12}$ was determined as one of the reaction intermediates, it will be worthwhile to perform more experimental studies on the stability of this compound in nanoconfinement, but also other intermediate compounds might be interesting. The method to synthesize $MgB_{12}H_{12}$ and other magnesium boron hydrides at nanoscale described this thesis could assist in this investigation. The addition of other elements, as was demonstrated with Ni, has the potential to steer the reaction to form certain magnesium boron hydride compounds. Yet, one has to keep in mind that partial decomposition will lower the storage capacity.

In summary, this thesis discussed novel methods to synthesize nanosized Mg-based compounds on carbon supports. Moreover, the high reactivity that the nanoparticles possess can be utilized in subsequent reactions to synthesize more complex compounds. An improved understanding on the influence of the carbon support in combination with nanosizing on the stability of various ternary and complex metal hydrides was attained. Addition of a carbon support and nanoparticles larger than 5 nm does not influence the reaction equilibrium of MgH_2.

However, nanosizing improves the hydrogen sorption kinetics of the metal(hydrides), while the carbon support is a tool to disperse the nanoparticles and prevent these from growing during operation at elevated temperatures. These new insights and tools can assist in the discovery of new functional materials and investigation on their physical and chemical properties. The application of supported alloy or hydride nanoparticles is not limited to hydrogen storage, but can also be relevant in other research fields with dynamic operation conditions like in catalysis or rechargeable batteries.

7. Samenvatting en vooruitblik

7.1 Samenvatting

Het grootschalige gebruik van fossiele brandstoffen, zoals benzine en aardgas, leidt tot een flinke toename van de CO_2 concentratie in de atmosfeer en een versterkt broeikaseffect. Door gebruik te maken van duurzame energiebronnen, zoals zonne- en windenergie, kan de uitstoot van CO_2 worden teruggedrongen. Toch is het gebruik van een brandstof gewenst. Zonnepanelen en windmolens wekken meestal elektriciteit op voor het lichtnet. Hierdoor is het meestal noodzakelijk om aan het lichtnet verbonden te zijn om van de opgewekte elektriciteit gebruikt te kunnen maken. Als alternatief kan elektriciteit uit zonne- of windenergie gebruikt worden om duurzame brandstoffen te produceren voor mobiele toepassingen (Fig. 7 - 1).

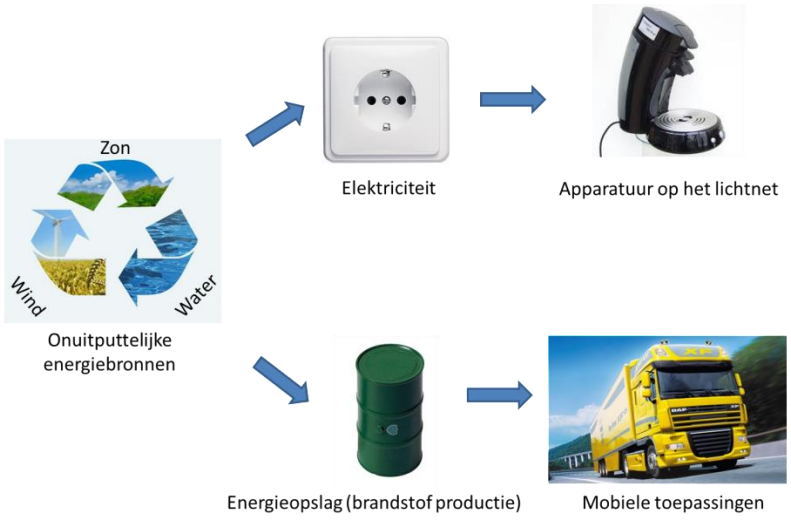

Fig. 7 - 1: Duurzame energiebronnen kunnen meestal alleen in elektriciteit omgezet worden. Voor mobiele toepassingen is een brandstof handiger. Een brandstof kan met de opgewekte energie geproduceerd worden.

Een duurzame brandstof kan bijvoorbeeld biodiesel, biogas, methanol of waterstof zijn. Waterstof is een interessante keuze omdat het kan worden geproduceerd zonder uitstoot van CO_2. Waterstof kan gemaakt worden door elektrolyse van water, waarbij de elektriciteit afkomstig is van duurzame energiebronnen. Om weer energie uit waterstof terug te winnen kan deze worden verbrand of elektrochemisch worden omgezet in elektriciteit met een brandstofcel, waarbij water wordt terug gevormd volgens de reactie: $2\ H_2 + O_2 \rightarrow 2\ H_2O$. Waterstof kan echter

alleen in de samenleving geïmplementeerd worden als er een compacte en veilige opslagmethode beschikbaar is. Waterstof is een gas en bestaat uit moleculen. Bij kamertemperatuur en atmosferische druk heeft waterstofgas een lage dichtheid, waardoor het veel ruimte inneemt. Ook is waterstof zeer licht ontvlambaar en explosief als het ongecontroleerd in contact wordt gebracht met lucht. Het opslaan van waterstof als waterstofatomen in chemische verbindingen, zoals het metaalhydride MgH_2, is interessant omdat het een stuk veiliger is dan opslag in gasvorm onder hoge druk. Waterstof kan niet ongecontroleerd vrijkomen omdat de waterstofatomen sterk gebonden zijn in de chemische verbinding. De dichtheid voor waterstof in chemische verbindingen kan 10 keer hoger zijn dan voor waterstofgas opgeslagen onder hoge druk en dit is schematisch weergegeven in Fig. 7 - 2.

Fig. 7 - 2: Schematische weergave van het volume van 10 kg waterstof opgeslagen in verschillende vormen. Het gewicht van de opslagtank is buiten beschouwing gelaten.

De opslag van waterstof doormiddel van vaste verbindingen heeft echter enkele nadelen. De opslagcapaciteit is beperkt tot het aantal waterstofatomen dat gebonden kan worden in de verbindingen. MgH_2 kan bijvoorbeeld per magnesium atoom slechts 2 waterstofatomen binden. Omdat relatief veel magnesium (M_{Mg} 24 g·mol^{-1}) gebruikt moet worden om 1 waterstofmolecuul op te slaan (M_{H2} 2 g·mol^{-1}), neemt het totaalgewicht toe. Toch is waterstofopslag qua gewicht competitief met Li-ion batterijen die worden toegepast in voertuigen.

Een ander nadeel is dat de chemische binding in een metaalhydride vaak sterk is, waardoor veel warmte toegevoerd moet worden om waterstof eruit te halen en dus hoge temperaturen nodig zijn. Ook waterstof binden aan het materiaal is niet altijd eenvoudig, omdat de sterke binding tussen de watsrstofatomen in een waterstofmolecuul (H_2) verbroken moet worden en de waterstofatomen door het materiaal moeten diffunderen (schematisch weergegeven in Fig. 7 - 3). Beide processen gebeuren met een bepaalde snelheid die niet altijd hoog genoeg is voor

praktische toepassingen. De reversibiliteit is een belangrijk aspect die de levensduur bepaald van het materiaal. Meestal streeft men naar 1000 laad en ontlaad cycli met een minimaal verlies aan opslagcapaciteit.

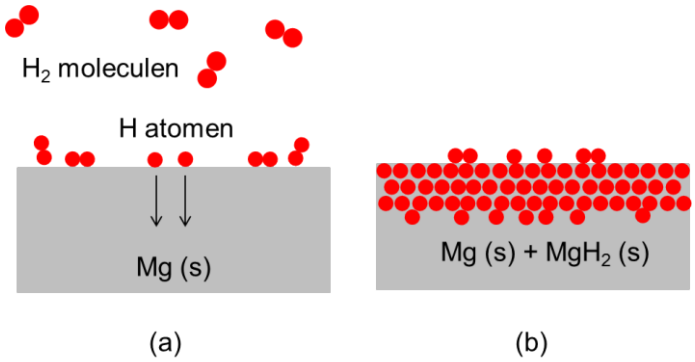

Fig. 7 - 3: (a) De waterstofmoleculen (H_2) worden gesplitst in waterstofatomen (H) en binden aan het metaal om een metaalhydride te vormen (b). In dit voorbeeld is magnesium (Mg) het metaal dat waterstofatomen bindt en magnesiumhydride (MgH_2) het metaalhydride dat wordt gevormd.

In dit proefschrift worden verschillende methoden uiteengezet om de waterstofopslag eigenschappen van chemische verbindingen te verbeteren. Magnesium gebaseerde verbindingen zijn interessant vanwege de ruime beschikbaarheid en lage prijs (3 €/kg 2013). Omdat magnesium een licht element is, is het totaal gewicht van het opslagsysteem relatief laag. Het nadeel van magnesium(hydride) is dat een hoge temperatuur nodig is om het materiaal te laten werken. Het evenwicht van de reactie: $MgH_2 \leftrightarrow Mg + H_2$ ligt bij 300 ^oC en 1 bar waterstof met als gevolg dat waterstof alleen vrijkomt bij temperaturen hoger dan 300 ^oC. Ook is de snelheid van de waterstofopname en afgifte laag.

Verschillende methoden kunnen worden toegepast om het evenwicht te veranderen en de reactiesnelheid te verbeteren. Het toevoegen van andere elementen als katalysatoren of om een magnesiumlegering te vormen, is een optie. Een van de uitdagingen is om het materiaal in de vorm van nanodeeltjes te maken. Nanodeeltjes maken dat het opslagmateriaal fysisch en chemisch andere eigenschappen heeft, maar nog steeds is opgebouwd uit dezelfde atomen. Bij nanodeeltjes kan waterstof sneller afgegeven en opgenomen worden doordat de diffusieafstand voor de waterstofatomen door het materiaal klein is. Ook is de verhouding oppervlakte : volume groot, waardoor waterstof het materiaal beter kan bereiken en verlaten. Een manier om nanomaterialen te maken is door nanodeeltjes af te zetten op een poreuze drager. De grootte van de nanodeeltjes kan worden beïnvloed door de grootte van de poriën van het drager materiaal.

Ook blijven de nanodeeltjes door de drager van elkaar gescheiden, zodat zij niet kunnen samensmelten tot grote deeltjes tijdens gebruik bij hoge temperaturen.

In **hoofdstuk 2** staat beschreven hoe koolstofdragers met verschillende poriegrootte zijn gebruikt om verschillende deeltjesgrootte van magnesium te maken. Ook is de invloed van de deeltjesgrootte op de reactiesnelheid voor waterstofopname en afgifte onderzocht. Magnesium werd boven zijn smeltpunt verhit samen met het drager materiaal, waardoor Mg nanodeeltjes konden worden gevormd op de drager. De verschillende dragers hadden een poriegrootte van 6 nm, 9 nm, 12 nm en 20 nm, waarop $Mg(H_2)$ nanodeeltjes werden gevormd met een gemiddelde grootte van 6.3 nm, 7.9 nm, 9.8 nm en 14 nm respectievelijk. Metingen hebben aangetoond dat de waterstofafgifte van MgH_2 nanodeeltjes sneller was dan MgH_2-deeltjes met een grootte van enkele micrometers. Ook de kleine nanodeeltjes onderling vertoonden een verschil in reactiesnelheid, waarbij kleinere deeltjes een hogere reactiesnelheid hadden. Het verschil in dynamiek van de waterstof atomen in MgH_2 tussen nanodeeltjes en grote deeltjes is ook aangetoond met ^1H NMR metingen. De Mg nanodeeltjes waren na 15 min voor 80% opgeladen met waterstof en dit proces was reversibel voor enkele cycli, zonder afname van de opslagcapaciteit en reactiesnelheid. Het is dus mogelijk om een poreuze koolstof drager te gebruiken om de deeltjesgrootte van $Mg(H_2)$ te controleren en samensmelten van de nanodeeltjes tegen te gaan.

Hoofdstuk 3 beschrijft een nieuwe methode om nanodeeltjes te maken van een Mg-Cu legering. De koolstof gedragen Mg-Cu legering kan bij lagere temperaturen waterstof opnemen en afgeven (66 $kJ \cdot mol^{-1}H_2$) dan MgH_2. De eerste stap om de nanodeeltjes te maken, was door Cu nanodeeltjes af te zetten, zowel op een koolstofdrager met een poreuze structuur als op een koolstofdrager zonder poriën, door impregnatie met een waterige oplossing van $Cu(NO_3)_2$. Daarna werd de legering gevormd door Mg samen met de koolstof gedragen Cu nanodeeltjes te verhitten boven de smelttemperatuur van Mg. De kleinste legering deeltjes werden op de poreuze drager gevormd met een gemiddelde grootte van 20 nm. Op de drager zonder poriën waren legering deeltjes met een gemiddelde grootte van 300 nm ontstaan. Het gebruik van een poreuze drager is dus een belangrijke factor om kleinere deeltjes te kunnen maken. Het specifieke oppervlak van de poreuze koolstofdrager is groter dan de koolstofdrager zonder poriën. Dit leidde tot een betere verdeling van de nanodeeltjes over de drager. Het verschil in deeltjesgrootte had ook invloed op de waterstofafgifte. De 20 nm deeltjes gaven waterstof af bij 250 ^oC, terwijl

micrometer grote deeltjes pas bij 400 ^{o}C ontleedden. Waterstofafgifte voor de 300 nm deeltjes vond plaats rond 350 ^{o}C. De activeringsenergie voor waterstofafgifte volgde dezelfde trend: 128 (± 6) kJ·mol^{-1}, 102 (± 7) kJ·mol^{-1} en 97 (± 9) kJ·mol^{-1} werd gevonden voor deeltjes van 1 micrometer, 300 nm en 20 nm respectievelijk. De hogere reactiesnelheden hangen samen met de korte diffusie afstanden voor de Mg en Cu atomen om de legering van Mg_2Cu naar $MgCu_2$ te transformeren en omgekeerd. De legering kon in waterstof gecycleerd worden en vertoonde alleen na de eerste cyclus een klein verlies aan opslagcapaciteit.

$Mg(BH_4)_2$ zou theoretisch bij temperaturen beneden 100 ^{o}C kunnen ontleden (39 kJ·mol$^{-1}H_2$) en heeft een hoge opslagcapaciteit (14.9 wt% H_2). Ontleding van $Mg(BH_4)_2$ verloopt echter traag omdat het via meerdere tussenstappen gebeurt. Ook waterstofabsorptie om $Mg(BH_4)_2$ terug te vormen is moeilijk, omdat de ontledingsproducten (waaronder MgB_2) erg stabiel zijn. Door nanodeeltjes te maken van $Mg(BH_4)_2$, zou de ontledingsreactie sneller kunnen verlopen en de waterstofopname kunnen verbeterd kunnen worden. In **hoofdstuk 4** wordt een nieuwe methode behandeld om $Mg(BH_4)_2$ nanodeeltjes te maken. $Mg(BH_4)_2$ werd gemaakt door MgH_2 nanodeeltjes op een koolstofdrager te laten reageren met diboraangas (B_2H_6) onder kogelmalen bij kamertemperatuur. ^{11}B vaste stof NMR metingen toonden de aanwezigheid van $Mg(BH_4)_2$ en $MgB_{12}H_{12}$, terwijl in röntgendiffractie geen lijnen werden gevonden die duidden op de aanwezigheid van kristallijne magnesiumboorhydride verbindingen. Het amorfe $Mg(BH_4)_2$ ontleedde al bij 100 ^{o}C en dat is een stuk lager dan de 250 ^{o}C voor kristallijne $Mg(BH_4)_2$ deeltjes. Uit de ontleedde nanoverbindingen kon gedeeltelijk $Mg(BH_4)_2$ terug gevormd worden.

Het kogelmalen vernielde echter de poriestructuur van de koolstofdrager, waardoor het gebruik van verschillende koolstofdragers geen significant effect had op de reactie. Om de invloed van nanodeeltjes in de poriën van een koolstofdrager te kunnen bestuderen, is een andere methode gebruikt om magnesiumboorhydriden te maken en deze is beschreven in **hoofdstuk 5**. Het plan was om gebruik te maken van de hoge reactiviteit van MgH_2 nanodeeltjes om een reactie met B_2H_6 aan te gaan en magnesiumboorhydride te vormen zonder de poriestructuur van koolstof te veranderen. De koolstof gedragen MgH_2 nanodeeltjes werden met en zonder toevoeging van Ni-deeltjes, behandeld bij verschillende temperaturen onder B_2H_6/H_2 druk. Nadat de koolstof gedragen MgH_2-nanodeeltjes waren behandeld bij 120 ^{o}C was voornamelijk $MgB_{12}H_{12}$ aanwezig zoals aangetoond in ^{11}B vaste stof NMR. Röntgendiffractie en waterstofafgifte metingen lieten zien dat vrijwel alle MgH_2 nanodeeltjes hadden gereageerd met B_2H_6, terwijl grote MgH_2

deeltjes niet reageerden. Door toevoeging van Ni veranderde de reactiviteit van de nanoverbinding en $MgB_{12}H_{12}$ werd al bij 30 ^{o}C gevormd. Zowel kristallijn Mg_2NiH_4 als MgH_2 reageerden met B_2H_6. Na behandeling bij 60 ^{o}C en 120 ^{o}C werden andere magnesiumboorhydriden gevormd, waaronder $Mg(BH_4)_2$. De ontledingstemperaturen voor de nieuwe magnesiumboorhydride verbindingen waren verlaagd van 300 ^{o}C naar 170 ^{o}C vergeleken met kristallijn $Mg(BH_4)_2$.

7.2 Vooruitblik

Het verkleinen van een materiaal tot nanodeeltjes leidt tot een grotere verhouding “oppervlakte : volume”, waardoor atomen met een kortere afstand door het materiaal kunnen diffunderen. Hierdoor werd bij het Mg-Cu systeem de reactiekinetiek verbeterd. Het is echter nog niet duidelijk welke andere eigenschappen van nanodeeltjes de kinetiek kunnen beïnvloeden. Met ^{1}H vaste stof NMR op MgH_2 is aangetoond in hoofdstuk 2 dat de mobiliteit van waterstofatomen in nano-MgH_2 deeltjes hoger is dan voor deeltjes in de orde van micrometers. Dit is een nieuw aspect voor nanodeeltjes dat nog niet eerder is aangetoond. Ook is in hoofdstuk 2 beschreven hoe MgH_2 nanodeeltjes gemaakt kunnen worden met een specifieke grootte. Deze preparaten zouden geschikt kunnen zijn voor andere geavanceerde metingen om nieuwe specifieke eigenschappen van nanodeeltjes te ontdekken.

Een nadeel van het toevoegen van een koolstofdrager is dat het de waterstof opslagcapaciteit verlaagd. De opslagcapaciteit voor koolstof gedragen Mg gebaseerde materialen kan geoptimaliseerd worden door de belading met de actieve magnesiumcomponent te verhogen. Verder onderzoek naar nieuwe methoden om deze hogere beladingen te bereiken zou een volgende stap kunnen zijn om het materiaal verder te verbeteren. De onderzoeken die zijn behandeld in dit proefschrift maakten voornamelijk gebruik van de methode door Mg boven de smelttemperatuur te verhitten om Mg nanodeeltjes op een koolstofdrager af te zetten, wat op een grotere schaal toegepast zou kunnen worden. Eerder onderzoek beweert dat het afzetten van nanodeeltjes gebeurt via smeltinfiltratie, maar dit kan alleen als er een goede interactie (bevochtiging) tussen Mg en de koolstofdrager is. Een andere mogelijkheid zou kunnen zijn dat de Mg nanodeeltjes worden afgezet vanuit de gasfase, omdat Mg een hoge dampdruk heeft. Een onderzoek naar dit mechanisme zou kunnen leiden tot hogere beladingen van Mg nanodeeltjes op koolstof.

De keuze voor het meest geschikte opslagmateriaal is afhankelijk van de toepassing. In grootschalig industriële processen zou de vrijgekomen warmte uit een ander proces gebruikt kunnen worden voor het waterstofopslag. In dit geval lijkt $Mg(H_2)$ geschikt als opslagmateriaal. Magnesium heeft weliswaar een hoge werkingstemperatuur nodig, maar vertoont een goede reversibiliteit en zal naar verwachting een lange levensduur hebben. Voor andere processen waar minder warmte vrijkomt en gewicht geen belangrijke rol speelt, zou een legering als Mg_2Cu geschikt kunnen zijn.

$Mg(BH_4)_2$ zou in aanmerking kunnen komen voor mobiele toepassingen vanwege de hoge opslagcapaciteit en lage ontledingstemperatuur. De slechte reversibiliteit van $Mg(BH_4)_2$ moet echter opgelost worden. Onderzoek naar gedeeltelijke ontleding van $Mg(BH_4)_2$ tot één van de tussenproducten die minder stabiel is dan MgB_2 zou uitkomst kunnen bieden. In hoofdstuk 5 is een methode beschreven om koolstof gedragen nano-$MgH_{12}H_{12}$ deeltjes te maken, die hierbij zou kunnen helpen. $MgB_{12}H_{12}$ werd eerder als tussenproduct gevonden tijdens de ontleding van $Mg(BH_4)_2$, dus het zou interessant kunnen zijn om de stabiliteit van $MgB_{12}H_{12}$, maar ook van andere magnesiumboorhydriden verder te onderzoeken.

Samengevat zijn in dit proefschrift nieuwe methodes uiteengezet om metalen, legeringen en metaalhydriden als nanodeeltjes te maken gedragen op koolstof. De hoge reactiviteit van de nanodeeltjes kan worden gebuikt als uitgangspunt om meer complexe verbindingen te maken. Hoewel een verandering in de evenwichtsligging voor nanodeeltjes groter dan 5 nm niet is waargenomen, is meer inzicht verkregen in de stabiliteit en reactiekinetiek van nanodeeltjes van metaalhydriden gedragen op koolstof. De reactie verloopt sneller voor nanodeeltjes en de koolstofdrager beperkt de groei van de nanodeeltjes. De beschreven methoden in deze dissertatie kunnen worden gebruikt bij vervolgonderzoeken voor het bepalen van de chemische en fysische eigenschappen van nieuwe materialen, die ook gebruikt zouden kunnen worden voor andere toepassingen, zoals katalysatoren of batterijen.

List of Publications and Presentations

This thesis is based on the following publications:

"The size dependence of hydrogen mobility and sorption kinetics for carbon-supported MgH_2 particles"
Yuen S. Au, Margo Klein Obbink, Subramanian Srinivasan, Pieter C.M.M. Magusin, Krijn P. de Jong, Petra E. de Jongh
Advanced Functional Materials, DOI: 10.1002/adfm.201304060, 2014
(Chapter 2)

"Synthesis of Mg_2Cu nanoparticles on carbon supports with enhanced hydrogen sorption kinetics"
Yuen S. Au, Marine Ponthieu, Rien van Zwienen, Claudia Zlotea, Fermin Cuevas, Krijn P. de Jong and Petra E. de Jongh
Journal of Materials Chemistry A, 2013, 1, 9983
(Chapter 3)

"$Mg(BH_4)_2$ / carbon nanocomposite with improved hydrogen sorption performance"
Yigang Yan,* Yuen S. Au,* Daniel Rentsch, Andreas Züttel, Petra E.de Jongh and Arndt Remhof
Journal of Materials Chemistry A, 2013, 1, 11177
(Chapter 4)

"Pore confined synthesis of magnesium boron hydride nanoparticles"
Yuen S. Au,* Yigang Yan,* Krijn P. de Jong, Arndt Remhof and Petra E.de Jongh
Submitted
(Chapter 5)

Other publications:

"Design and synthesis of highly efficient CuCo/MoOx catalysts for the selective production of higher alcohols from synthesis gas"
Gonzalo Prieto, Steven Beijer, Miranda Smith, Ming He, Yuen S. Au, Zi Wang, David Bruce, Krijn P.de Jong, James Spivey and Petra E. de Jongh
Submitted

"In-situ x-ray Raman spectroscopy of nanoconfined alkali metal borohydrides"
Piter S. Miedema, Peter Ngene, Ad M.J. van der Eerden, Dimosthenis Sokaras, Tsu-Chien Weng, Dennis Nordlund, Yuen S. Au, Petra E. de Jongh and Frank M.F. de Groot
Submitted

"Crystal structures and chemistry of double perovskites $Ba_2M(II)M'(VI)O_6$ (M=Ca, Sr, M'=Te, W, U)" W.T. Fu, Y.S. Au, S. Akerboom, D.J.W. IJdo
Journal of Solid State Chemistry, 2008, 181, 2523

"Crystal structure of $Ca_2Ln_3Sb_3O_{14}$ (Ln=La, Pr, Nd and Y): A novel variant of weberite"
Y.S. Au, W.T. Fu, D.J.W. IJdo
Journal of Solid State Chemistry, 2007, 180, 3166

* indicates shared first authorship of the publication

Oral Presentations

"Synthesis of Mg_2Cu nanoparticles in a carbon matrix for hydrogen storage"
Yuen S. Au, Petra E. de Jongh
Advances in Dutch Hydrogen and Fuel Cell Research, Eindhoven (March 2011)

"Improved hydrogen sorption kinetics in supported Mg_2Cu nanoparticles"
Yuen S. Au, Krijn P. de Jong, Petra E. de Jongh
The 13th Netherlands Catalysis and Chemistry Conference, Noordwijkerhout (March 2012)

"The synthesis and hydrogen sorption properties of supported Mg_2Cu nanoparticles on carbon"
Yuen S. Au, Marine Ponthieu, Rien van Zwienen, Claudia Zlotea, Fermin Cuevas, Krijn P. de Jong, Petra E. de Jongh
International Symposium on Metal-Hydrogen Systems, Kyoto, Japan (October 2012)

"The influence of carbon scaffolds with different pore sizes on the hydrogen desorption properties of MgH_2"
Yuen S. Au, Margo Klein Obbink, Krijn P. de Jong, Petra E. de Jongh
2nd International Conference on Materials for Energy, Karlsruhe, Germany (May 2013)

Poster Presentations

"Improved hydrogen sorption kinetics in supported Mg_2Cu nanoparticles"
Yuen S. Au, Krijn P. de Jong, Petra E. de Jongh
6th Int. Symposium Hydrogen & Energy ,Stoos, Switzerland (January 2012)

"Melt infiltration of MgH_2 into carbon aerogels and H_2 sorption properties"
Margo Klein Obbink, Yuen S. Au, Petra E. de Jongh
The 13th Netherlands Catalysis and Chemistry Conference, Noordwijkerhout (March 2012)

"Carbon-confined $LiBH_4$ for hydrogen storage"
Angeloclaudio Nale, Peter Ngene, Yuen. S. Au, Petra E. de Jongh
International Symposium on Metal-Hydrogen Systems, Kyoto, Japan (October 2012)

"The influence of different pore sizes of a carbon scaffold on the hydrogen release properties of melt infiltrated Mg"
Yuen S. Au, Margo Klein Obbink, Krijn P. de Jong, Petra E. de Jongh
The 14th Netherlands Catalysis and Chemistry Conference, Noordwijkerhout (March 2013)

Dankwoord

De resultaten van alle onderzoeken beschreven in dit proefschrift zijn mogelijk gemaakt door inspanning en inzet van verschillende personen, die ik graag in dit stuk zou willen bedanken. Als eerste wil ik graag mijn promotoren Krijn en Petra bedanken voor de kans en het vertrouwen die zij mij hebben gegeven om mijn onderzoek te mogen doen in de vakgroep Anorganische Chemie en Katalyse aan de Universiteit Utrecht. Ik herinnerde me dat het even zoeken was om een geschikt onderwerp voor mij te vinden, maar uiteindelijk is de keuze erg goed bevallen. Ik heb de afgelopen 4 jaar veel kunnen leren en dat heeft een positieve uitwerking gehad op mijn persoonlijke ontwikkeling. De ervaringen die we samen hebben gedeeld zullen mij zeker bijblijven.

Next I would like to acknowledge all the people, who collaborated with me to realize the results described in this thesis. Arndt, Claudia, Fermin, Marine and Yigang, it was really fun to work with you and your contributions were essential for chapters 3-5. Our fruitful exchange programs and our trip to Japan will always be part of my memory. Margo, jij was een geweldig persoon om samen mee te werken. Ons werk samen met Pieter heeft een prachtig resultaat opgeleverd. Hoofdstuk 2 was er zonder jullie hulp niet geweest. Hans en Rien, jullie namen moeten natuurlijk niet vergeten worden. Erg veel resultaten waren niet alleen door jullie gemeten, maar ook de discussies over de interpretatie hebben een significante bijdrage gehad op het eindresultaat.

De overige leden van de (technische) staf wil ik ook graag bedanken. Ten eerste onze Ads. Ad M., jij was altijd bereid en snel mij te helpen als ik iets nodig had. Ad E. de beamtrips verliepen altijd voorspoediger als jij erbij was. Fouad en Marjan, ook bedankt voor de bestellingen en SEM metingen. Dymph en Monique, bedankt voor jullie hulp bij al mijn ‘huishoudelijke’ vraagstukken en natuurlijk niet te vergeten, de EHBO.

Now I want to thank my (former) H-team members. I would like to credit my seniors first. Sankara, thanks for your initial help to get me into the research field. Your knowledge is still there in the group. Peter N., you showed me how to get through tough times. Thanks a lot for the discussions and mental support. Jinbao, you were always helpful during labwork and for

discussions. Angelo and Suwarno, both of you were always in for a nice chat or scientific discussions. I had a lot of fun with you guys. Peter B., I wish you all the best during your ‘quest’ for completing your thesis.

I also would like to mention my close colleagues, who I had fun with during lunch and/or the NIOK course. Carlo, Roy, Hendrik, Jelle, Dimitrije, Thomas, Tomas, Sam, Rafael, Wenhao, Peter M., Arjan, Jeroen, Zoran, Jesper, Daniel, Joe, Gang, JX and Ilona. Good luck with completing your theses. I really enjoyed the time being with you guys.

In de slotparagraaf wil ik graag mijn beste vrienden bedanken voor hun steun. Bas, Erik, Kobus, Rolf en Victor. Het was erg fijn om af en toe andere dingen samen met jullie te doen of even mijn hart te luchten als dat nodig was. Tot slot wil ik graag de belangrijkste personen in mijn leven, mijn aanstaande, zus en moeder bedanken. Dit boekje is voor jullie geschreven.

About the author

Yuen Sheng Au was born in Leiden on 6th of February 1986. In March 2010, he started a PhD curriculum in the group Inorganic Chemistry & Catalysis, supervised by dr. P.E. de Jongh and prof. dr. ir. K.P. de Jong at Utrecht University. The research was focused on hydrogen storage materials in Mg-based systems. The work was carried out in collaboration with several universities and research institutes which were: Technische Universiteit Eindhoven, Institut de Chimie et des materiaux in Paris and the Swiss Federal Laboratories for Materials Science and Technology. The collaboration with Swiss Laboratories was made possible by a financial support, which he received from "the European Cooperation in Science and Technology" for the research proposal "Nanostructured $Mg(BH_4)_2$ catalyzed with Ni, Co, Cu for reversible hydrogen storage" in 2013.

He also carried out teaching tasks in the educational program of the chemistry course at Utrecht University, which included the supervision of the first year organic chemistry practical course "Synthesis of esters" and the supervision of two master students. He was also partly responsible for the publicity of the chemistry course provided by Utrecht University to high school students and supervised five groups of students in research projects related to hydrogen and renewable energy. The PhD curriculum was completed with the thesis entitled "Magnesium-based materials supported on carbon for hydrogen storage" including six publications in scientific journals in four years and the results were presented at six (inter)national conferences.